An investigation of the wind noise reduction mechanism of porous microphone windscreens

A thesis submitted in fulfilment of the requirements for the degree of Doctor of Philosophy

Sipei Zhao

M.S., Nanjing University, China

B.S., Nanjing University, China

School of Engineering

College of Science, Engineering and Health

RMIT University

March, 2018

Declaration

I certify that except where due acknowledgement has been made, the work is that of the author alone; the work has not been submitted previously, in whole or in part, to qualify for any other academic award; the content of this thesis is the result of work which has been carried out since the official commencement date of an approved research program; and any editorial work, paid or unpaid, carried out by third party is duly acknowledged.

Sipei Zhao

Date: 13-02-2018

Acknowledgements

I would like to express my appreciation to my supervisor Prof. Xiaojun Qiu for the guidance, encouragement and support during the process of my PhD. I am grateful to Prof. Mike Austin, Dr. Eva Cheng, Prof. Ian Burnett, Dr. Katrina Neville for being my supervisors. I would like to thank my team mates at RMIT University, Mr. Matthew Dabin, Ms. Xiaoying Wang, Mr. Ross Nye, and Mr. Jiuyang Zhu for their accompany. I would like to thank the administrative staff Associate Prof. Elena Pirogova, Ms. Bethany McKinnon, Ms. Laurie Clinton et al. for their help during my PhD candidature. The financial support from the Australian Research Council through the Linkage Project (LP140100740) is acknowledged.

I sincerely thank my parents, my parents in law, my grandfather, my uncle, my aunt, my brothers and sister, my brother and sister in law, for their continuing support in this hardest period in my life. Last but not least, I would like to express my deepest gratitude to my wife Jihua Kong and our son Shixun Zhao for their optimism spirit, tireless support and selfless love that keep me fuelled all the time.

Abstract

Wind energy is a green way to produce electricity without carbon emissions. However, the infrasound and low frequency audible sound radiated by wind turbines may adversely affect the nearby communities. To investigate the impact of wind farm noise and to understand its noise generation mechanism and propagation, the sound level of wind farm noise must be measured under windy conditions. However, it is often a challenge to measure wind turbine noise under windy conditions in quiet rural residential areas due to wind noise, especially for infrasound and low frequency audible sound. Wind noise is the pseudo sound pressure generated on microphones due to turbulent pressure fluctuations and is indistinguishable from the acoustic signals to be measured. Various microphone windscreens have been utilized to reduce wind noise. However, the physical mechanism of wind noise reduction by windscreens has been unclear to date.

The aim of this PhD research is to investigate the mechanisms of wind noise generation and the wind noise reduction mechanism of porous microphone windscreens, and then develop a new compact acoustic measurement system that is insensitive to wind noise. To achieve this objective, a critical literature review is first presented to summarise the state-of-the-art research results in the field of wind noise and its reduction. Then, the research is focused on three aspects: the mechanisms of wind noise generation, the wind noise reduction mechanism of porous microphone windscreens, and wind noise reduction with a compact spherical microphone array.

In the first aspect of this thesis, the generation mechanism of wind noise is explored and two theoretical models are proposed to predict wind noise spectra. One model is for outdoor atmospheric turbulence where the Reynolds number based on the Taylor microscale varies from 4250 to 19500, and the other is for indoor fan generated turbulent flows where the Reynolds number based on the Taylor microscale is estimated to be around 432. The

proposed theoretical models are validated with existing simulations and experimental results from the literature, as well as measurement results conducted as part of this thesis in a car park for outdoor wind noise and in a laboratory for wind noise from an axial fan.

In the second aspect of this thesis, the mechanism of wind noise reduction by porous microphone windscreens is investigated. It is shown that the wind noise reduction of porous microphone windscreens is caused by viscous and inertial forces introduced by the porous structure. Simulation results indicate that the design of porous microphone windscreens should take into account both turbulence suppression inside and wake generation behind the windscreens to achieve optimal performance. Besides, porous windscreens are found to be the most effective in attenuating wind noise in a certain frequency range, where the windscreen diameter is approximately 2 to 4 times the turbulence wavelengths. It is also found that the wind noise reduction is related to the spatial decorrelation of the wind noise signals provided by porous microphone windscreens. The simulation findings are validated with measurement results from an axial fan in a laboratory.

In the last aspect of this thesis, a method for wind noise reduction with the spherical microphone array is proposed, and the effect of wind noise on the beamforming performance of a spherical microphone array is investigated. The characteristics of the wind noise is explored and compared with the sound signals in the spherical harmonics domain, based on which a spherical harmonics domain low pass filter method is proposed to reduce wind noise without degrading the desired sound signal. Experimental results demonstrate the feasibility of the proposed method. On the other hand, the effects of wind noise on the beamforming performance of the spherical Plane Wave Decomposition (PWD), Delay and Sum (DAS) and Maximum Variance Distortionless Response (MVDR) beamformers are studied. The experimental results demonstrate that the MVDR beamformer is insensitive to wind noise and able to localise the sound source direction under windy conditions.

In summary, two theoretical models are proposed in this PhD research to predict the wind noise spectra in outdoor, large Reynolds number, atmospheric turbulence and indoor, small Reynolds number, turbulent flows, respectively; the physical mechanism of wind noise reduction by porous microphone windscreens is found to be related to the spatial decorrelation effect on the wind noise signal due to the porous structure, and it is demonstrated that the design of porous windscreens should take into account both turbulence suppression inside and wake generation behind the windscreen to achieve optimal performance; the effect of wind noise on the beamforming performance of a spherical microphone array is investigated and a spherical harmonic domain low pass filtering method is proposed to attenuate wind noise without degrading the desired sound signal.

Key words: wind noise, wind noise reduction, microphone windscreen, low frequency noise

Contents

List of Figures

List of Tables

1 Introduction

Wind energy is a green way to produce electricity without carbon emissions and wind generated electric power has expanded rapidly since the beginning of the 21st century [1]. However, the infrasound and low frequency audible sound radiated by wind turbines may adversely affect the nearby communities, potentially leading to sleep disturbance and psychological distress [2–4]. To investigate the impact of wind farm noise and to understand its noise generation mechanism and propagation, the sound pressure level of wind farm noise under windy conditions must be measured. However, it is often challenging to measure wind turbine noise under windy conditions due to the interference of wind noise, especially for infrasound and low frequency audible sound. Wind noise is the pseudo sound pressure generated on microphones due to turbulent pressure fluctuations, which is indistinguishable from the noise from far field wind turbines.

1.1 Motivation and objectives

Low frequency sound measurement under windy conditions is an important problem in acoustics with many applications, and considerable effort has been put into the research. Raspet et al. [5,6] proposed that the wind noise detected by a microphone outdoors is composed of the stagnation pressure, the turbulence-turbulence interactions and the turbulence-shear interactions, and studied the wind noise spectra measured by microphones with and without windscreens. However, these wind noise spectra are restricted to the inertial range for intermediate size turbulent eddies, but are not valid for the energy-containing range and the dissipation range for larger and smaller size turbulent eddies.

Various methods have been utilized to reduce wind noise without degrading the sound signal. These methods can be categorized as physical structures and signal processing

techniques. The porous microphone windscreen shown in Figure 1.1(a) is the most widely used physical structure for wind noise reduction due to its small size and portability. However, the exact wind noise reduction mechanism of porous microphone windscreens remains unclear yet.

In addition, wind noise reduction of small porous windscreens is unsatisfactory in strong wind conditions, especially in the infrasonic and audible low frequency range. Therefore, the international standard IEC61400-11 recommends a secondary windscreen of at least 450 mm diameter to be used on a flat hard circular board, as shown in Figure 1.1(b) [7]. To reduce wind noise effect in the infrasound measurements, other physical structures such as large wind fence enclosures [8] and spatial filters [9] are also used, as shown in Figure 1.1(c) and (d), respectively. However, these structures are usually meters or tens of meters in size, which makes them inconvenient and cumbersome for ordinary outdoor noise measurements.

Microphone arrays have also been used for outdoor noise measurements, especially for noise source localisation. Oerlemans et al. [10] used a planar microphone array of 270 m^2 to measure a full scale wind turbine noise. Ramachandran et al. [11] utilized a compact planar microphone array of 1.5 m^2 to investigate the wind turbine noise measurement with advanced deconvolution algorithms based on a linear programming method. However, the effect of wind noise on the array performance is not studied, and a simple diagonal removal of the cross spectrum matrix was used to eliminate the wind noise on microphones with the assumption that wind noise is incoherent between microphones. Unfortunately, this assumption is not true, because Wilson et al. [12] showed that wind noise is substantially correlated for microphone separations smaller than the size of turbulent eddies.

Therefore, accurate low frequency acoustic measurement in the presence of turbulence is still a challenge, although it is critical in outdoor environmental noise measurements and other applications such as noise measurements in ventilation systems. This motivated the

research of this PhD thesis to investigate the generation mechanism of wind noise and the wind noise reduction mechanism of porous microphone windscreens, based on which a new compact low frequency acoustic measurement system was developed.

(a)

(b)

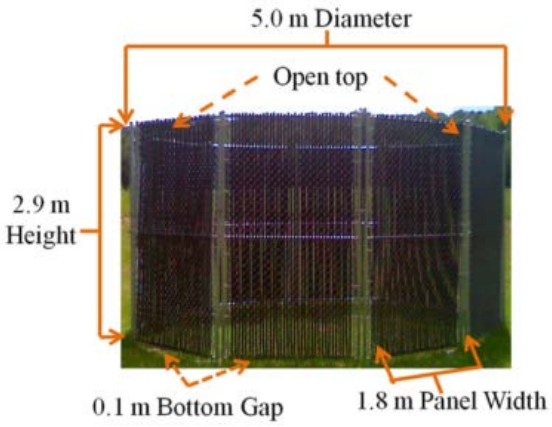

(c)

(d)

Figure 1.1 (a) A 90 mm diameter porous microphone windscreens, (b) a 750 mm diameter semi-spherical secondary windscreen on board [13], (c) a 5 m diameter wind fence enclosure [8], and (d) a 18 m diameter porous hose rossete [14].

The overall objective of this research was to develop a new compact low frequency acoustic measurement system that is small in size but effective in reducing wind noise. The specific aims were to:

1) investigate the wind noise generation mechanism;
2) study the physical mechanism of wind noise reduction by porous microphone windscreens; and
3) develop a new compact acoustic measurement system that is insensitive to wind noise.

1.2 Contributions and outcomes

The main contributions of this thesis include:

- proposing a theoretical model for wind noise spectra in outdoor atmospheric turbulence, where the Reynolds number is sufficiently large (4250 ~ 19500);
- proposing a theoretical model for wind noise spectra in indoor fan generated turbulent flows, where the Reynolds number is small (~432);
- discovering that the design of porous microphone windscreens should take into account both turbulence suppression inside and wake generation behind the windscreens to achieve optimal performance;
- discovering that porous microphone windscreens are the most effective in attenuating wind noise in a certain frequency range, where the windscreen diameter is approximately 2 to 4 times the turbulence wavelengths, and that the wind noise reduction is related to the spatial decorrelation of wind noise signals provided by porous microphone windscreens; and
- developing a low pass filter method in the spherical harmonics domain to extract a desired sound signal from the measured sound pressure which is contaminated by wind noise.

The main outcomes of the author during the PhD candidature include:

- publications (see Appendix A for details)
    - 4 articles published in *The Journal of the Acoustical Society of America*;
    - 2 peer-reviewed conference papers presented at *ACOUSTICS 2016*; and
    - 2 peer-reviewed conference papers presented at *INTER-NOISE 2017*;

and

- awards/accolades
    - Young Professional Grant from the International Institute of Noise Control Engineering (2017);
    - Higher Degree by Research (HDR) Publication Incentive Grant for quality research publication from the School of Engineering, RMIT University (2017 & 2018);
    - HDR Travel Grant from the School of Engineering, RMIT University (2017); and
    - HDR Travel Grant from the School of Graduate, RMIT University (2016).

1.3 Thesis outline

The rest of the thesis is organised as follows. Chapter 2 gives an extensive and critical literature review in the field of wind noise generation and reduction. Chapter 3 proposes two theoretical models to predict wind noise spectra in outdoor atmospheric turbulence with large Reynolds number and indoor fan generated turbulent flows with small Reynolds number. Chapter 4 is devoted to the investigation of the wind noise reduction mechanism of small porous microphone windscreens. Chapter 5 develops a low pass filter method in the spherical harmonics domain to attenuate wind noise but retain the desired sound signal with a compact

spherical microphone array. Finally, conclusions are drawn and future work is discussed in Chapter 6.

2 Literature review

Wind-induced noise is the noise measured by a microphone in the presence of turbulent flows, including the pseudo-sound pressure fluctuations produced by turbulence in incoming flows, self-noise due to interaction of the incoming flow with microphone, and aeroacoustic noise caused by wind interaction with nearby objects [1]. It has been shown that in outdoor acoustic measurements in large open spaces, the self-noise and aeroacoustic noise due to the interaction of wind with nearby objects such as buildings and vehicles are much smaller than the pseudo-sound pressure fluctuations on microphones [15]. The wind noise in this thesis targets at the pseudo-sound noise caused by turbulent pressure fluctuations.

Wind noise affects outdoor acoustic measurement accuracy, such as wind turbine noise, where wind noise is inevitable because measurements cannot be made in still conditions. On average, approximately 90% of wind noise energy is concentrated below 15 Hz and 95% below 30 Hz [16], which presents challenges in the measurements of low frequency dominated wind farm noise [1]. Kendrick et al. [17,18] studied the effect of wind noise on the amplitude modulation metrics for wind turbine noise, and found that bias errors of over 4 dBA are produced by wind noise even at a low wind speed of 2.5 m/s.

Wind noise can also corrupt outdoor audio recordings and cause problems for users of hearing aids. Perceptual tests were carried out by Jackson et al. [17] to evaluate the audio quality of speech recordings contaminated with wind noise, where the average A-weighted sound pressure level of the wind noise was found to dominate the perceived degradation of audio quality, while gustiness was mostly unimportant. In addition, verbal communications in windy environments can become problematic for both the hearing aid and cochlear implant users, where the wind noise significantly lowers the signal-to-noise ratio at the microphone and consequently reduces the speech intelligibility [19–21].

Although wind noise is of broad interest to a wide range of applications, the mechanism of wind noise generation has not been understood well. This chapter presents an extensive literature review regarding the generation and reduction of wind noise.

2.1 Wind noise generation

There has been a large amount of research on pressure fluctuations in turbulent flows, which is the main source of wind noise. The theoretical research on pressure fluctuations in turbulent flows started in the first half of the 20th century. However, the wind noise research in the 20th century was focused on experimental studies, and little theoretical progress is published until the 21st century.

2.1.1 Pressure fluctuations in turbulent flows

The theoretical studies of turbulent pressure fluctuations were mostly based on the energy cascade theory proposed in 1922 by Richardon [22] and quantitatively developed in 1941 by Kolmogorov [23] for turbulence. According to the energy cascade theory, turbulence can be considered to be composed of eddies with different sizes, as shown in Figure 2.1. The kinetic energy enters the turbulence at the large scales of motion and then transfers to smaller and smaller scales until the energy is dissipated into heat by viscous effect at the smallest scales [23]. The anisotropic large eddies are affected by the boundary conditions of the flow, and bulk energy is contained in the large eddies of the size ranging from $L/6$ to $6L$ (L is the characteristic length scale of the mean flow), which is therefore called the energy-containing range [24].

As the kinematic energy transfers to smaller eddies, the directional information of the turbulent eddies is lost and the statistics of motions are in a sense of universal. When the size of eddies is much larger than the smallest eddies, the statistics of motion is uniquely determined by the energy dissipation rate and independent of the kinematic viscosity and the

boundary conditions of the flow. This is the inertial range where eddy motions are determined by inertial effects and the viscous effects are negligible [24]. As the kinematic energy further transfers to successively smaller eddies, approaching the smallest eddy, the statistics of motion have a universal form that is uniquely determined by the kinematic viscosity and the energy dissipation rate. The size of the smallest dissipative eddies is about $(\nu^3/\varepsilon)^{1/4}$ (ε is the energy dissipation rate, ν is the kinematic viscosity [23]). This is the dissipation range where the eddy motions experience significant viscous effects [24].

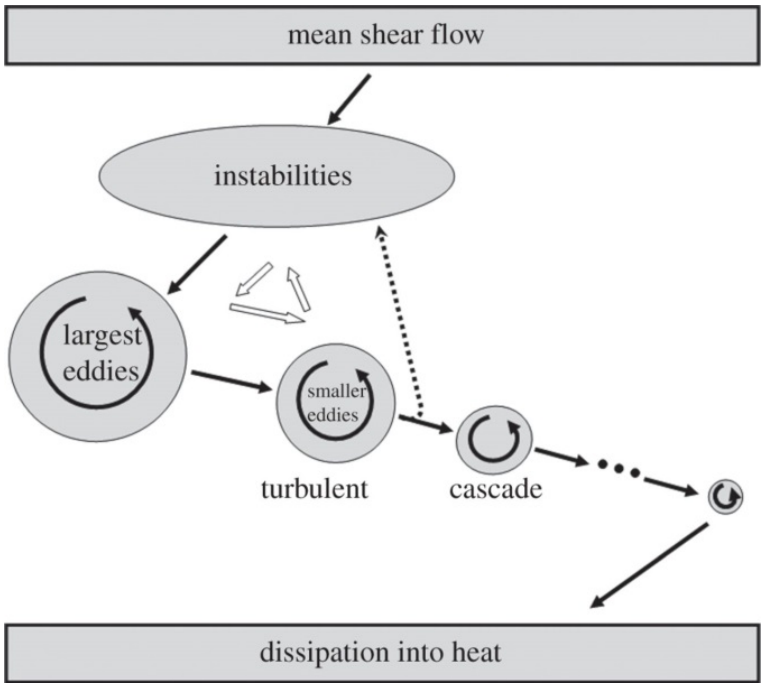

Figure 2.1 Illustration of the energy cascade in turbulence [25].

To quantitatively investigate the pressure fluctuations in turbulent flows, most of the theoretical studies were based on the Poisson equation, which relates the pressure fluctuations in a viscous incompressible fluid flow to the velocity fluctuations, i.e.,

$$\frac{1}{\rho}\nabla^2 P = -\frac{\partial^2 V_i V_j}{\partial x_i \partial x_j} \tag{2.1}$$

where ρ is the fluid density, P is the instantaneous static pressure, and V_i is the velocity along the x_i direction [26]. It is noteworthy that the wind noise caused by turbulent pressure fluctuations is not a propagating compressible acoustic wave, but a pseudo-sound [27]. In the scenario of acoustic measurement under windy conditions, the wind speed is usually much smaller than the speed of sound, hence the turbulent flow can be approximated as incompressible turbulence in Eq. (2.1).

Batchelor derived the pressure correlation function from the Poisson Equation based on the assumption that the velocities at two spatial points are joint Gaussian [26]. He pointed out that the joint Gaussian assumption produced the same results as Heisenberg's assumption that the Fourier components of velocities are statistically independent [26]. From the pressure correlation function, it can be shown that the pressure structure function varies as $r^{4/3}$ (r is the separation distance between two spatial locations) and hence the pressure spectrum varies as $k^{-7/3}$ (k is the wavenumber) within the inertial range [26,28]. The joint Gaussian assumption is consistent with the experimental results that the distribution of the velocity at one point is closely normal [26,29]. However, when the separation distance is very small, the assumption cannot be held because the effect of the non-linear inertial terms cannot be ignored [26].

Instead of using the joint Gaussian assumption, Obukhoff and Yaglom [30] found that $D_p(r) \sim \varepsilon^{4/3} r^{4/3}$ based on the dimensional analysis by assuming the eddy motions are determined by the energy dissipation rate in the inertial range, where $D_p(r) = \langle (p(x) - p(x+r))^2 \rangle$ is the pressure structure function. More than 40 years later, Hill and Wilczak [28] developed a theoretical model to relate the pressure structure function to the fourth-order velocity structure functions and claimed that the new theory is valid for all Reynolds numbers and for all spatial separations and wavenumbers. Based on this, the $k^{-7/3}$ pressure spectrum in the inertial range was also obtained [28].

In an alternative approach, George et al. [31] developed spectral models for turbulent pressure fluctuations by directly Fourier transforming the integral solution to the Poisson equation, and showed that the pressure spectrum consists of two source terms. One is the turbulence-turbulence interaction that possesses the well-known $k^{-7/3}$ inertial range and dominates the high-wavenumber region. The other is the mean shear-turbulence interaction that is dominant in the energy-containing range and falls off as $k^{-11/3}$ in the inertial range [31].

In summary, studies on the pressure spectrum in turbulent flows have been focused in the inertial range for intermediate size turbulent eddies in the existing literature. In contrast, the studies of the pressure spectra in the energy containing range and for large eddies and the dissipation range for small eddies are relatively rare. Raspet et al. [6] pointed out that the pressure spectra are near constant in energy-containing range based on measurements, and proposed a model based on van Karman spectra to curve fit the measurement results. However, this model is based on experimental results and no theoretical analysis was given. The pressure spectra in the energy-containing range and the dissipation range need further theoretical study.

2.1.2 Wind noise spectra

Recently, Raspet et al. [5] utilized Batchelor's theory to predict the pressure fluctuation spectrum in the inertial range from the measured velocity fluctuation spectrum. They studied three components of wind noise: the stagnation pressure due to the interaction of the incoming flow with the microphone, the self-noise due to the microphone windscreen, and the intrinsic turbulence in the incoming flow including the turbulence-turbulence interaction pressure and the mean shear-turbulence interaction pressure [5].

The stagnation pressure is the maximum pressure fluctuations measured on a bluff body in turbulent flows, which can be calculated as [5]

$$P(t)=\frac{1}{2}\rho V(t)^2=\frac{1}{2}\rho\left(U+u(t)\right)^2=\frac{1}{2}\rho U^2+\rho U u(t)+\frac{1}{2}u(t)^2 \tag{2.2}$$

where $P(t)$ is the instantaneous pressure, $V(t) = U + u(t)$ is the instantaneous turbulent velocity, and U and $u(t)$ are the mean flow speed and velocity fluctuations, respectively. For outdoor measurements at moderate to high wind speeds, the root-mean-square fluctuation velocity is usually much smaller than the mean wind speed, so Raspet et al. [5] approximate that

$$p(t)\cong\rho U u(t) \tag{2.3}$$

where $p(t)$ is the fluctuating pressure. Raspet et al. [5] measured the velocity fluctuations $u(t)$, from which the stagnation pressure $p(t)$ is calculated and used to predict the wind noise measured by a bare microphone.

The turbulence-turbulence interaction pressure and the mean shear-turbulence interaction pressure are due to the intrinsic turbulence in the incoming flow [31]. It is known that the governing equation for the static pressure field in an incompressible fluid can be written as the Poisson equation in Eq. (2.1) [31]. By decomposing the pressure and velocity into mean and fluctuating parts and integrate Eq. (2.1), one obtains [31]

$$p(\mathbf{x})=-\frac{\rho}{4\pi}\int\left[\frac{\partial U_i}{\partial y_j}\frac{\partial u_j}{\partial y_i}+\frac{\partial U_j}{\partial y_i}\frac{\partial u_i}{\partial y_j}\right]\frac{\mathrm{d}^3\mathbf{y}}{|\mathbf{y}-\mathbf{x}|}-\frac{\rho}{4\pi}\int\frac{\partial^2}{\partial y_i\partial y_j}\left[u_iu_j-\left\langle u_iu_j\right\rangle\right]\frac{\mathrm{d}^3\mathbf{y}}{|\mathbf{y}-\mathbf{x}|} \tag{2.4}$$

where $p(\mathbf{x})$ is the fluctuating pressure at location $\mathbf{x}$, U_i and u_i are the mean and fluctuating velocities in the i-th direction, and <> denote the average operation. It is clear that the first term on the right hand side of Eq. (2.5) is due to the interaction of the turbulence (fluctuating velocity) with the mean shear, whereas the second term is due to the interaction of the turbulence with itself. Therefore, the mean shear-turbulence interaction pressure and the turbulence-turbulence interaction pressure are defined as the first and second term on the right hand side of Eq. (2.5), respectively.

In comparison with the measurement results, Raspet et al. [5] found that the stagnation pressure agreed well with the measured wind noise of a bare microphone and the turbulence-turbulence interaction pressure was consistent with the wind noise measured in a large fiberglass windscreen of diameter 0.9 m. Therefore, they concluded that the stagnation pressure and turbulence-turbulence interaction pressure provide the upper and lower bound on the wind noise measured outdoors [5].

In a further study, Raspet et al. [6] extended the predicted stagnation pressure, the turbulence-turbulence interaction pressure, and the mean shear-turbulence interaction pressure to lower frequencies in the energy-containing range. Comparison with the measurement results showed that the stagnation pressure predictions agreed well with the unscreened gridded microphone measurements and the predictions of the turbulence-turbulence interaction pressure agreed well with the measurements made within large windscreens of 1.0 m diameter [6]. Therefore, they concluded that the turbulence-turbulence interaction pressure and the mean shear-turbulence interaction pressure are intrinsic to a turbulence flow and would be measured even if the wind screen design were ideal [6].

It is noteworthy that the above predictions of the turbulence-turbulence interaction pressures depend on a coefficient to be determined by fitting the velocity fluctuation spectrum to the measurement results. In Refs. [5,6], Raspet et al. compared the measured wind noise spectra *inside* the porous microphone windscreens with the predicted turbulence-turbulence interaction pressure derived from the velocity spectra measured *outside* windscreens. This might lead to inaccurate comparisons and even wrong interpretations because both the mean wind speed and turbulence intensity *inside* the porous microphone windscreen are lower than that *outside* the windscreens.

Different from the abovementioned studies which did not account for the effect of ground surface, Yu et al. [32,33] investigated the wind noise spectra measured at the ground using

the mirror flow model of anisotropic turbulence, which was originally proposed by Kraichnan [34] for pressure fluctuations over a flat plate. Yu et al. [32,33] showed that the wind noise measured at the ground surface with a microphone underneath the thin layers of foam agree closely with the predictions, demonstrating the applicability of the mirror flow model for outdoor turbulence and illustrating that the mean shear-turbulence interaction pressure is the dominant source of wind noise at the ground surface. However, this model is limited to the wind noise on the ground surface. In a following paper, Yu et al. [35] extended the mirror flow model to predict the wind noise spectra above the ground surface by incorporating a realistic wind velocity profile and realistic turbulence anisotropy. The revised prediction model of the mean shear-turbulence interaction pressure was found to compare favourably with the wind noise measured inside large windscreens at low frequency.

The theoretical models developed by Raspet et al. [5,6] and Yu et al. [32,35] were utilized to predict the wind noise measured in outdoor experiments. Raspet and Webster [36] measured the wind noise levels, turbulence spectra and wind velocity profiles in a pine forest, and found that the wind noise spectrum is a sum of the low frequency wind noise generated by the mean shear-turbulence interaction above the top of trees and the higher frequency wind noise generated by the turbulence-turbulence interaction near the ground within the tree layer. Similar wind noise spectra were measured by Webster and Raspet [37] under a deciduous tree canopy. The low frequency peak in the wind noise spectra due to the mean shear-turbulence interaction was found to have little dependence on whether the trees have leaves or not, while the higher frequency contribution with leaves was approximately one order of magnitude smaller than the contribution without leaves [37].

In addition to the aforementioned theoretical and experimental studies of wind noise spectra, Kamiakito et al. [38] developed a regression function to estimate the 1/3-octave band wind noise level, i.e.,

$$L_{1/3} = A(f) + B(f)\log_{10}(1+I)^2 + C(f)\log_{10}(U_0)^2 \quad (2.5)$$

where U_0 is the mean wind speed, I is the turbulence intensity, f is the centre frequency of the 1/3-octave band, and the coefficients A, B, and C are determined from measurements of wind noise, which were found to be dependent on frequency and the surface roughness of surrounding terrain. However, in practice, it is hard to use this model because it is not possible to do the accurate regression analysis in the vicinity of an operating wind farm due to the influence of the wind-farm-generated noise [1].

In summary, outdoor wind noises have been measured and modelled theoretically and empirically by different researchers with various methods. These theoretical models were focused in the inertial range and deviated from the wind noise spectra measured in wind tunnels. This might because the Reynolds number in outdoor atmospheric turbulence is much larger than that in indoor turbulent flows generated by wind tunnels and fans. The existing models did not take into account the Reynolds number effect, and there are no theoretical models to describe the wind noise spectra in small Reynolds number turbulent flows to date.

2.2 Wind noise reduction with physical structures

Various physical structures and materials have been utilized to reduce wind noise, from small porous microphone windscreens with a diameter of a few centimetres to large spatial filters in tens or even hundreds of metres. An ideal windscreen blocks the pressure fluctuations caused by turbulent flows but is transparent to the propagating sound wave. This section summarises the existing studies on the wind noise reduction devices. However, the nose cone and tubular windscreens [39,40] are not included here, because it is usually used in wind tunnel measurements with constant wind direction and low turbulence intensity, which is distinctly different from the outdoor wind noise in acoustic measurements [1].

2.2.1 Small porous microphone windscreens

Porous microphone windscreens have been widely used in outdoor noise and ventilation system acoustic measurements to minimize the effect of wind noise due to its portability, durability and low cost [41,42]. Although this measure for reducing wind noise is well known and widely used, the mechanisms of the wind noise reduction by porous microphone windscreens have not been fully understood.

Strasberg [43] investigated the wind noise sensed by microphones in spherical and cylindrical windscreens of various diameters and found that the 1/3-octave band wind noise levels measured by different authors with different windscreens form a single curve when plotted against the Strouhal number (fD/U_0), i.e.,

$$L_{1/3} = 61 + 40\log_{10} U_0 - 23\log_{10} \frac{fD}{U_0} \tag{2.6}$$

where f is the frequency, D is the windscreen diameter, U_0 is the mean wind speed. It was shown that the wind noise level decreases linearly with the dimensionless frequency in log-scale for values of fD/U up to 5 [43,44].

Morgan and Raspet [15] pointed out that Strasberg's analysis [43] is only valid for low-turbulence environments because the data used by Strasberg were measured in laboratories by moving the screened microphones through substantially quiet air. In contrast, the dominant source of pressure fluctuations at the microphone outdoors is the intrinsic turbulence in the incoming flows, hence the optimum design of windscreens for outdoor measurements may require consideration of factors other than the wake generation and reduction of flow through windscreens [15]. Raspet et al. [5,6] proposed that the minimum wind noise inside windscreens is the intrinsic turbulence in the incoming flow, including the turbulence-turbulence interaction pressure and the mean shear-turbulence interaction pressure. Based on an analysis of the outdoor measurement results from different authors, van den Berg [45,46]

proposed that windscreens could be treated as a first order low pass filter for pressure fluctuations due to atmospheric turbulence.

In addition to the abovementioned studies for outdoor noise measurement, the wind noise reduction effects of windscreens were also investigated in wind tunnels. Lin et al. [47] measured the wind noise reduction of different types of windscreens in the low frequency range from 20 Hz to 200 Hz, showing that the noise reduction performance of various types of windscreens is similar when the wind speed is under 1.5 m/s; however, for wind speeds above 2.0 m/s, the larger spherical porous windscreen (20 cm diameter) reduced more wind noise than the smaller windscreen (7 cm diameter) made of the same material. The experimental setup used by Lin et al. [47] to measure the wind noise inside the porous microphone windscreens are shown in Figure 2.2.

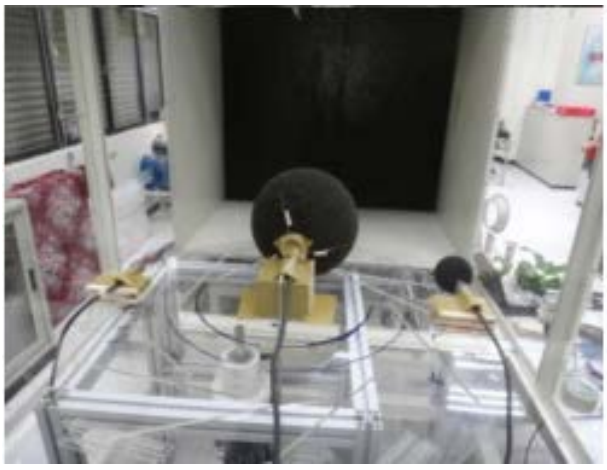

Figure 2.2 Experimental setup to measure wind noise inside the large (20 cm diameter) and small (7 cm diameter) porous microphone windscreen [47].

Wang et al. [48] measured the self-noise of microphone windscreens in an anechoic wind tunnel and found that the wind noise is generally more effectively attenuated by windscreens with larger diameters, but windscreens with diameters of 60 mm and 90 mm showed similar performance. Alamshah et al. [49] investigated the effects of turbulent flow characteristics on

wind noise generation in microphone windscreens, and found that the wind noise at very low frequencies increases with the average turbulent length scales while the overall wind noise inside windscreens is insensitive to the incoming flow turbulence intensity. The experimental setup used by Wang et al. [48] and Alamshah et al. [49] is illustrated in Figure 2.3, where the microphone inside windscreens are placed at the outlet of a small anechoic wind tunnel, and a reference microphone is placed outside the air flow.

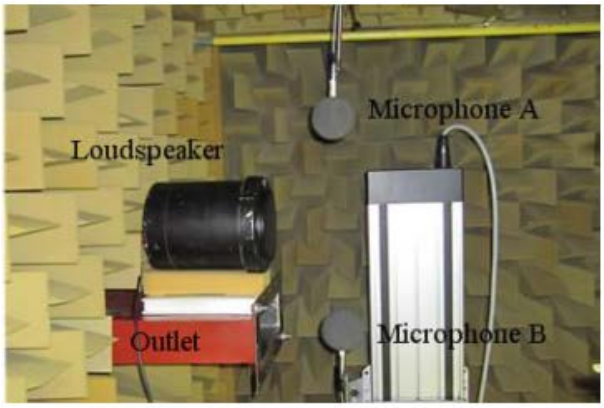

Figure 2.3 Experimental setup to measure wind noise inside a 90 mm diameter porous microphone windscreen, where Microphone A works as the reference microphone outside the air flow [48].

Raspet et al. [50] measured the correlation length of pressure fluctuations inside a 180 mm diameter porous microphone windscreen at various separation distances, as shown in Figure 2.4, where metal tubes placed inside the porous windscreens are connected to the microphones at the other end. It was found that the wind noise reduction mechanism by microphone windscreens is attributed to the spatial decorrelation of the pressure fluctuations [50].

(a) (b)

Figure 2.4 Experimental setup to measure wind noise inside a 180 mm diameter porous microphone windscreen at various separation distances [50].

Although many different windscreens were used in both indoor and outdoor measurements, the noise reduction mechanism of windscreens still lacks theoretical analysis. A primarily intuitive explanation is that the windscreens can reduce the wind speed at the microphone, hence reduce the measured wind noise [51]. Phelps [51] modeled the windscreen as a rigid sphere and calculated the pressure inside the sphere by averaging the pressure distribution on the spherical surface, with the assumption that the air flow is inviscid, incompressible and irrotational. Zheng and Tan [52] modeled the microphone windscreen as a rigid impermeable sphere to investigate the effects of Reynolds number on the wind noise reduction performance. The analytical solutions for the inviscid and Stokes flows were pursued as the two extreme cases for infinite and low Reynolds number flows, respectively, and the intermediate and high Reynolds number flows were studied with a numerical scheme [52]. These models are simplified because the windscreens are treated as a rigid impermeable sphere, and the air around windscreens is assumed to be steady-state laminar flows, both of which are different from practical situations.

To narrow the gap between the rigid sphere model and realistic windscreens, Xu et al. [27,53,54] modeled the windscreens as porous material and used an upstream rigid cylinder to generate turbulence on the downstream porous microphone windscreens in their numerical simulations. The effects of windscreen shape and the porous material properties (i.e., flow resistivity) were investigated, and it was found that the circular and horizontal ellipse windscreens have similar overall wind noise reduction performance, while the horizontal ellipse windscreen with medium flow resistivity provides larger wind noise reduction [27].

Nonporous windscreens were also used to reduce wind noise, especially in the infrasonic range [41,55–57]. Shams et al. [41] developed compact nonporous microphone windscreens for infrasonic acoustic measurements based on the assumption that the infrasound can penetrate any barrier of practical thickness while the wind fluctuations are blocked by the solid nonporous walls. The experimental results showed that a windscreen composed of closed-cell polyurethane foam with an internal diameter and height of 3×9 $inch^2$, and a wall thickness of 0.5 inch achieved the best performance, as shown in Figure 2.5(a). Dauchez et al. [56] studied the performance of a windscreen constructed from a squared plate coupled with a nonporous cavity as illustrated in Figure 2.5(b), and showed the mechanism of wind noise reduction to be the spatial averaging of the pressure fluctuations over the plate.

(a) (b)

Figure 2.5 Compact nonporous microphone windscreens developed by (a) Shams et al. [41] and (b) Dauchez et al. [56].

In summary, although the wind noise reduction performance of porous microphone windscreens has been measured in various studies, the wind noise reduction mechanism is still unclear yet. In addition, the existing theoretical models for porous microphone windscreens are too simplified and much different from the practical situations.

2.2.2 Semi-spherical shell windscreens

Small porous microphone windscreens for outdoor noise measurements are mostly restricted to wind speeds below 5 m/s [1,13]. For wind turbine noise measurement applications, it is often necessary to measure the turbine noise under typical operating

conditions with wind speeds up to 12 m/s [13]. This introduces extra noise on microphones, especially at low and infrasonic frequency range, and normal small spherical porous microphone windscreens are not adequate to attenuate wind noise [13]. Therefore, the international standard IEC61400-11 recommends a secondary windscreen of at least 450 mm in diameter to be used on a flat hard circular board on the ground [58].

Bleazey [59] studied the wind noise reduction by multi-layer windscreens and showed that the best performance is achieved by the largest windscreen and that fine mesh silk provides optimal wind noise attenuation. Besides, the wind noise reduction is only slightly improved by increasing the number of layers and no further performance enhancement is achieved by more than three layers [59]. The wind velocity fluctuations inside a multi-layer windscreen was measured by Iamizumi and Takahashi [60] using a hot-wire anemometer in an outdoor large field, where a significant reduction in both mean wind speed and velocity fluctuations was noticed compared to what was measured with no windscreen. Lin et al. [47] measured the wind noise reduction of a single layer (with and without fabric convering) and double layer semi-spherical shell windscreens in the low frequency range from 20 Hz to 200 Hz in an indoor wind tunnel, as shown in Figure 2.6. It was found that the noise reduction of 40 cm diameter single layer windscreen with fabric covering is larger than that of the double layer (30 cm and 40 cm diameters) frame windscreen without coverings [47].

(a) (b)

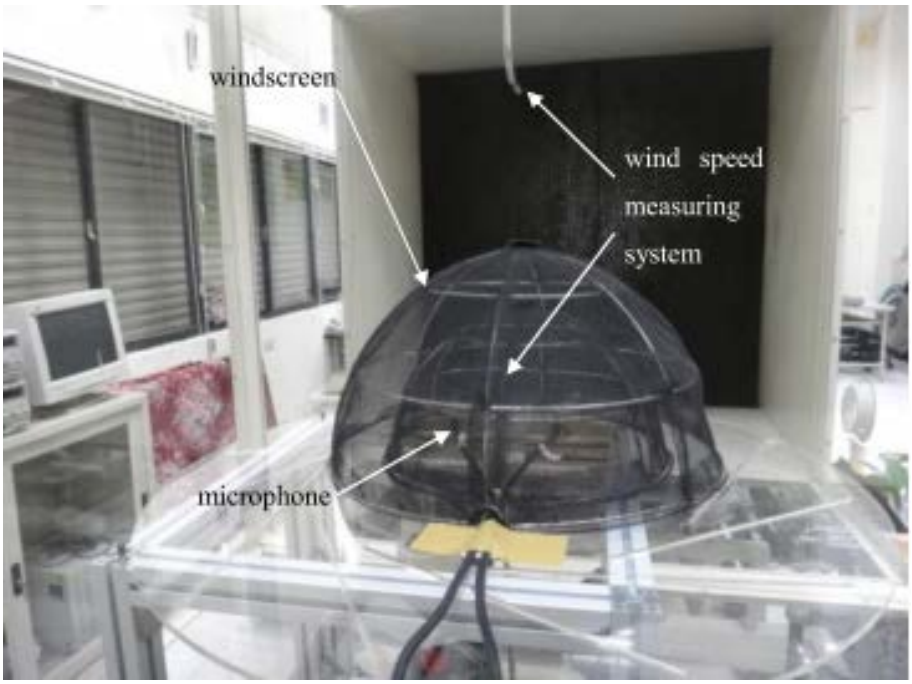

(c)

Figure 2.6 Experimental setup to measure the wind noise reduction of semi-spherical shell windscreen by Lin et al. [47] for (a) a 40 cm diameter single layer windscreen with fabric covering, (b) a 40 cm diameter single layer windscreen with fur covering, and (c) double layer windscreen (30 cm and 40 cm diameters).

Novak et al. [13] compared the wind noise reduction performance of three different secondary windscreens, i.e., a 750 mm diameter semi-spherical wireframe windscreen covered by an acoustically transparent material, a foam cylindrical windscreen of

approximately 10 mm thick and 300 mm tall, and a spherical windscreen of diameter 400 mm, as depicted in Figure 2.7. It was found that using the secondary windscreens together with a primary 90 mm diameter spherical porous windscreen attenuated much more wind noise compared to using the primary windscreen only, especially in the infrasonic range from 1 Hz to 20 Hz, where around 10 dB additional wind noise reduction is achieved [13].

Figure 2.7 Experimental setup of Novak et al. [13] to compare the performance of 3 different secondary windscreens.

Similarly, Hansen et al. [61] measured both the wind noise reduction and the insertion loss of three different secondary windscreens, i.e., a semi-spherical shell windscreen of diameter 450 mm covered by a layer of 16 mm thick SoundMaster acoustic fur, a 450 mm diameter spherical windscreen covered by the same material, and an underground 120 mm × 120 mm × 280 mm plywood box with a foam lid of 50 mm thick. The experimental setup is illustrated in Figure 2.8 and the measurement results showed a good agreement at low frequencies for the three windscreen configurations, and each secondary windscreen can successfully measure wind turbine noise in windy conditions [61].

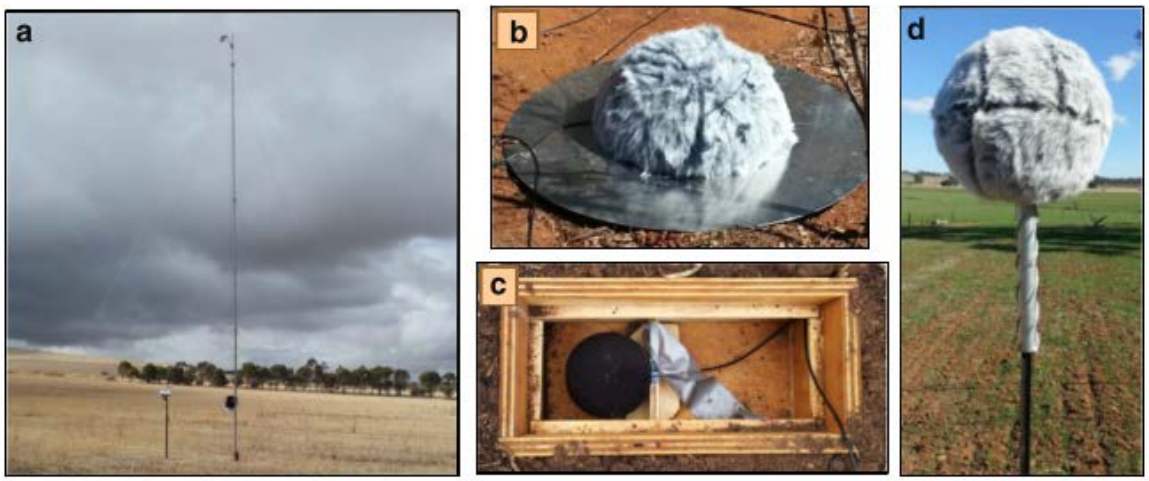

Figure 2.8 Experimental setup of Hansen et al. [61] to measure the wind farm noise with 3 different secondary windscreens, (a) the Davis weather stations at 1.5 m and 10 m, (b) the hemispherical windshield, (c) the box windshield and (d) the spherical windshield.

Recently, both porous and nonporous fabric domes with a diameter of 2 m have been used to reduce the infrasonic wind noise, as shown in Figure 2.9 [14,62–64]. Noble et al. [14] showed that the nonporous dome introduces too much distortion into the sound signals while the 7 percentage open porous dome made of acrylic and PVC blend fabric was found to have the best overall performance by maximising the wind noise reduction but losing only a small amount of sound signal. Collier et al. [63] and Abbott et al. [64] analysed the main wind noise source inside fabric domes by dividing the air flow into three regions, i.e., interior of the dome, surface of the dome, and undisturbed area outside the dome. Calculation of the turbulence-turbulence interaction, mean shear-turbulence interaction and turbulence-sensor interaction showed that the principle noise source is the pressure fluctuations on the surface of the domes and the turbulence interactions for undisturbed region contribute only at lowest frequencies [63,64].

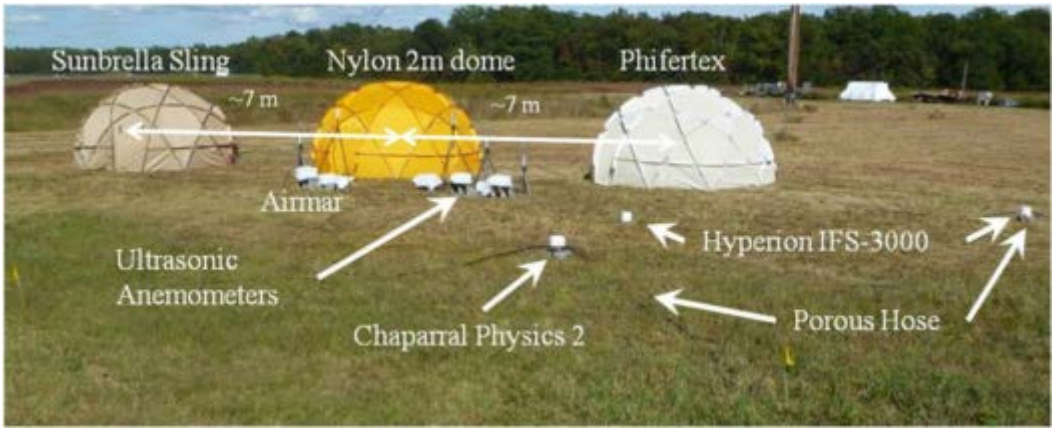

Figure 2.9 Illustration of 3 different fabric domes for infrasonic wind noise reduction [14].

The mechanism of enhanced wind noise reduction by secondary semi-spherical shell windscreens was believed to be that the layer of air gap behind the shell layer provides a region for viscous dissipation to reduce the turbulence inside the windscreens [1,15,61]. However, no direct evidence supports this hypothesis at present, and further study and measurements of both velocity and pressure fluctuations inside and outside the shell layer are needed for a deeper understanding.

2.2.3 Large spatial filters and wind fence enclosures

Another structure for reducing wind noise at a microphone is the wind fence enclosures or large spatial filters, which are particularly useful for wind noise reduction at infrasonic frequencies [1,65,66]. In the 1950s, Daniels [67,68] proposed a spatial filter consisting of a series of different tapered pipes with sensing inlets distributed uniformly along its length and a microphone connected to one end, based on the assumption that the sound signal is correlated while the wind noise is uncorrelated in each inlet. For infrasound measurements, the filter must be very large and pipe diameters and inlet impedance have to be carefully selected to inhibit internal resonance. A prototype filter of around 600 m long with 100 equally spaced openings achieved noise reduction of about 20 dB in high wind speeds up to 12 m/s [65,68]. The Daniels filter is effectively a line microphone, and the response is a

function of the angle between the sound direction and the pipe for shorter wavelengths, although it is omnidirectional for wavelengths much larger than the filter size [65].

A rosette filter is an extension of the Daniels filter and the inlets are arranged in a geometrically regular pattern around a circle to provide an omnidirectional infrasound response, as shown in Figure 2.10 [9,69]. The rosette filter is the standard wind-noise filter used at the International Monitoring System (IMS) [70]. Experiment results showed that a rosette filter with a diameter of 18 m reduced wind noise by 20 dB above 0.2 Hz and a 70 m diameter rosette filter reduced wind noise by a similar amount between 0.02 and 0.7 Hz [9,71]. Similar to the pipe filters, Howard et al. [72] utilized 1.6 cm diameter microporous hoses to collected infrasound data. However, both the rosette filters and microporous hoses are expensive to build and deploy, and occupy a considerable amount of space, which make it inconvenient for ordinary outdoor noise measurements [65].

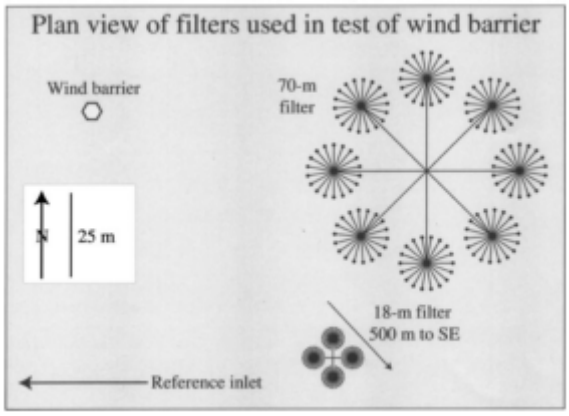

Figure 2.10 Diagram of a rosette filter with a diameter of 70 m [9,69].

Different from the mechanical rosette filters and microporous hoses, the optical fiber infrasound sensor (OFIS) directly measured the integrated pressure change along a path with a laser beam, which does not rely on the propagation of sound signals through a narrow tube [73–77]. A prototype OFIS sensor of 89 m was found to reduce the wind noise as much as

similar size mechanical arrays, but the phase delays of the sound signals are negligible in OFIS because the OFIS integrates pressure variations at light-speed rather than the speed of sound [73]. Dewolf et al. [78] found that the measured wind noise reduction is a logarithmic function of the OFIS length and depends on the orientation of the OFIS with respect to wind direction. The linear OFISs ranging in length from 30 m to 270 m provided a wind noise reduction of up to 30 dB in wind up to 5 m/s, and the parallel orientation to the wind direction achieved around 4 dB greater wind noise reduction than the perpendicular orientation.

Instead of averaging over a number of sensing surfaces, wind fence enclosures are used to isolate the sensor from the advected turbulence to reduce the turbulence-sensor interaction pressure [8,9,79,80]. Hedlin and Raspet [9] measured the wind noise reduction of a cylindrical barrier of 2 m height in a diameter of 5.5 m depicted in Figure 2.11(a), and compared it to that of the rosette filters with diameters of 18 m and 70 m in atmosphere. It was found that the rosette filters only produce reductions if the turbulence scale is smaller than the diameter of the rosette, and the cylindrical barrier has large reductions only when the scale size of the turbulence is smaller than the height of the barrier [9].

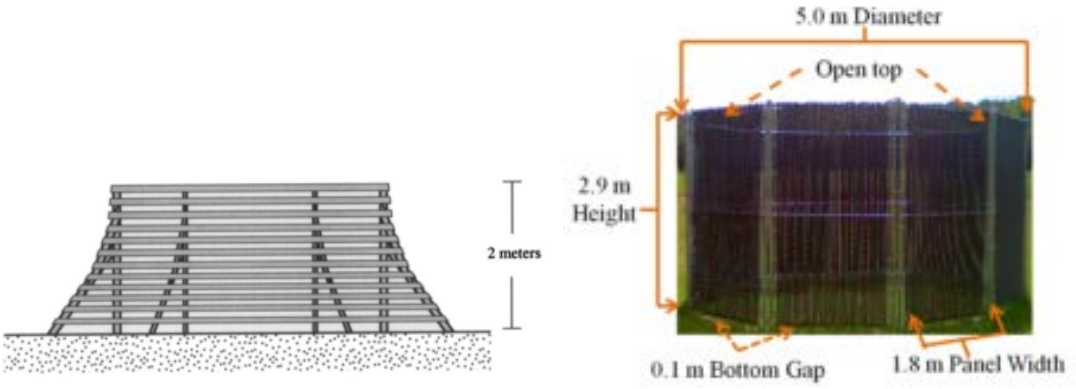

(a) (b)

Figure 2.11 Illustration of the wind fence enclosures studied by (a) Hedlin and Raspet [9] and (b) Abbott et al. [8] for infrasonic wind noise reduction.

Abbott et al. [8] optimized the wind noise reduction of a porous wind fence enclosure which is 2.9 m high and has a diameter of 5.0 m shown in Figure 2.11(b), and found that the most important parameters in achieving significant noise reduction were the size and porosity of the wind fence enclosure. The best reduction was achieved with a surface porosity between 40% and 55%, supplemented by a secondary dome windscreen of 0.6 m high with a 1.06 m interior diameter, 1.22 m exterior diameter, 0.08 m thick walls and pore count of 40 pores per inch [8]. In a following paper, Abbott and Raspet [79] proposed a calculation model to predict the wind noise measured at the center of large porous wind fence enclosures, which was found to provide a good prediction of the measured wind noise, with an agreement within ±5 dB. The mean shear-interaction pressure outside the enclosure was found to dominate the wind noise at low frequency, while at higher frequencies the measured wind noise was due to the combination of the turbulence-turbulence and mean shear-turbulence interactions inside the enclosure and the turbulence interaction on the surface of the enclosure[79].

The spatial filters and wind fence enclosures are not often used for wind turbine measurements because they are relatively large structures and are difficult to transport and erect, which make them not a realistic option for compliance measurements at a number of different locations [1].

In summary, various physical structures have been utilized to reduce wind noise in outdoor environment, including small porous microphone windscreens, nonporous windscreens, semi-spherical shell windscreens and large wind fence enclosures. The existing studies in literature are summarized in Table 2.1, where the size, frequency range and material/design of the physical structures are briefly introduced.

Table 2.1 Summary of the physical structures for wind noise reduction in literature

Type	References	Size (D)	Frequency Range (f)	Material/Design
Small porous microphone windscreens	Strasberg, 1988 [43]	$fD/U < 5$ (U is the mean wind speed)		Spherical /cylindrical porous
	Morgan and Raspet, 1992 [15]	90 mm 150 mm 180 mm	1.6 Hz < f < 1250 Hz	Porous sphere with porosity 10 ppi, 20 ppi and 40 ppi
	Raspet et al., 2006 [5]	180 mm 900 mm	0.1 m^{-1} < U/f < 200 m^{-1}	30 ppi Foam sphere; fibreglass ball
	Raspet et al., 2008 [6]	600 mm 1000 mm	0.001 m^{-1} < U/f < 100 m^{-1}	Fibreglass ball; loose fiberglass ball
	Van den Berg, 2006 [45,46]	25 mm ~ 100 mm	1 Hz < f < 1000 Hz	Foam sphere
	Lin et al., 2014 [47]	70 mm 200 mm	20 Hz < f < 200 Hz	Foam sphere
	Wang et al., 2012 [48]	45 mm ~ 180 mm	1 Hz < f < 1000 Hz	Foam sphere
	Alamshah et al., 2015 [49]	60 mm 90 mm	1 Hz < f < 1000 Hz	Foam sphere
Nonporous windscreens	Shams et al., 2005 [41]	25 mm ~ 100 mm	0.7 Hz < f < 20 Hz	Woods, closed-cell polyurethane foam and Space Shuttle tile material cylinders
	Dauchez et al., 2016 [56]	295 mm × 295 mm	0.02 Hz < f < 4 Hz	Rigid box with an elastic plate
Semi-spherical shell windscreen	Lin et al., 2014 [47]	300 mm 400 mm	20 Hz < f < 200 Hz	Mesh w/o fabric and fur coverings
	Novak et al., 2014 [13]	450 mm	0.02 Hz < f < 20 kHz	Wire frame with Reinhardt cloth
	Hansen et al., 2014 [61]	450 mm	0.5 Hz < f < 200 Hz	Wire frame with a 16 mm layer of acoustic foam and a layer of SoundMaster acoustic fur.
	Noble et al., 2014 [14] Collier et al., 2014 [63]	2 m	0.5 Hz < f < 100 Hz	Denier Nylon with polyurethane; Acrylic and PVC blend fabric;
Wind fences	Hedlin and Raspet, 2003 [9]	Height 2 m Width 5.5 m	0.01 Hz < f < 10 Hz	50% porous sides coated with a fine wire mesh
	Abbott et al. [8]	Height 2.9 m Width 5 m	0.1 m^{-1} < U/f < 100 m^{-1}	Chain link fence panels with vinyl slats

2.3 Wind noise reduction with signal processing

In addition to using physical structures to mitigate wind noise, signal processing techniques have also been explored for wind noise reduction. Chung [81] proposed a coherence function method for flow noise rejection using three pressure transducers based on the assumption that the flow noise is mutually uncorrelated at each transducer. Jackson et al. [17] estimated the wind noise level and signal to noise ratio based on machine learning algorithms to infer the perceived degradation of audio quality caused by wind noise. Wilson and White [82] analyzed the spatial and temporal characteristics of the wind noise with a planar microphone array, and discriminated the sound signal from wind noise with a Gaussian-mixture-model classifier.

Oerlemans et al. [10,83] measured the wind turbine noise with a planar microphone array of 270 m^2 consisting of 148 microphones and extracted the location of the wind turbine noise sources. Ramachandran et al. [11,84,85] used a compact planar microphone array of 1.5 m^2 to measure the wind turbine noise and showed that a compact microphone array is sufficient to study wind turbine noise if an advanced deconvolution method such as the linear programming algorithm is applied. However, the above studies did not investigate the effect of wind noise on the beamforming performance, and a simple diagonal removal of the cross spectrum matrix is used to eliminate the wind noise on microphones with the assumption that the wind noise is uncorrelated between microphones [84].

Unfortunately, this assumption is not valid in the lower frequency range which corresponds to the large scale turbulent eddies. Shields [86] employed a three-axis orthogonal microphone array with 10 sensors in each arm to measure outdoor wind noise and showed that the time domain correlation as a function of sensor separation varies as $e^{-3.2X}\cos(2\pi X)$ in the downwind direction and decays as e^{-7Y} in the crosswind direction, where X and Y are the separation in wavelengths in the downwind and crosswind directions, respectively. Wilson et

al. [12] measured the outdoor wind noise with a 7×7 planar horizontal microphone array and found that the wind noise is substantially correlated for microphone separations smaller than the size of the turbulent eddies. Bass et al. [87,88] showed that the cross correlation between pairs of microphones in a three element array could be used to determine wind speed and direction.

In an alternative approach, McGuinn et al. [89] proposed to reduce the flow induced noise in ducts by use of the adaptive Least Mean Square (LMS) algorithm to filter out the flow velocity fluctuations measured by a hot wire anemometer before subtraction from the pressure fluctuations measured by a microphone. This was based on the assumption that the flow velocity fluctuations are highly correlated with the flow induced noise [90]. Similarly, Shust and Rogers [91] studied the performance of wind noise removal from outdoor microphones using velocity measurements from a four channel anemometer and a simple model to transform the wind velocity fluctuations into wind noise estimates based on the Bernoulli equation. Unfortunately, the Bernoulli equation is only valid for fluid flows without turbulence and the coherence between the hot wire anemometer signal and the microphone signal is lower in outdoor environments, thus the performance was unsatisfactory [92].

Besides the abovementioned applications of signal processing techniques on wind noise attenuation in acoustic measurements under windy conditions, there have been much research devoted into speech enhancement algorithms on wind noise reduction in the last decade [93–97]. Kuroiwa et al. [98] proposed a wind noise reduction method for speech recording using multiple noise templates and observed spectrum fine structure. Nemer and Leblanc [99] presented a time domain adaptive post-filtering algorithm for detecting and attenuating wind noise in speech signals originating from mobile terminals. Hofmann et al. [100] developed a morphological approach for wind noise suppression by exploiting the neighborhood relations in the time-frequency spectrogram image. Thune et al. [101] applied the maximum likelihood

approach to adaptive multichannel Wiener post-filtering for wind noise reduction. Lee et al. [102] exploited the recurrent neural network algorithm to reduce wind noise and improve speech quality.

To further improve the wind noise reduction performance, dual channel systems have also been explored to enhance the speech signals in windy environments. Franz and Bitzer [103] proposed a multi-channel algorithm for wind noise reduction and signal compensation in binaural hearing aids. Nelke and Vary [104] utilized the phase variance of the complex coherence function in a dual microphone system to detect the wind noise and exploited the magnitude of the complex cross power spectral density to enhance the distorted speech signals. Sakai et al. [105] compared three types of coherence analysis on wind speed estimation and wind noise reduction using a two-channel small microphone array. Park et al. [106] proposed a two-step method, which exploits the coherence of input signals and uses a Wiener filter to wind noise regions, to reduce wind noise with a dual microphone system.

Although the speech enhancement algorithms have been reported to be able to reduce the wind noise and improve speech intelligibility, it is unclear if these methods can be applied to increase the signal to noise ratio in the low frequency acoustic measurements under windy conditions. The coherence structure of wind noise in the low frequency range makes it challenging to extract the desired sound signal from the wind noise, and further work is needed to develop a robust and compact acoustic measurement system for outdoor low frequency noise.

In summary, most of the existing wind noise reduction studies with microphone arrays were based on the assumption that wind noise is uncorrelated at each microphone. However, recent measurement results found that this assumption is not true, especially in the low frequency range, where the turbulence wavelength is larger than the separation distance between microphones. To mitigate the low frequency wind noise, microphone arrays must be

very large in size, which makes it inconvenient. Therefore, novel signal processing techniques are desirable to distinguish sound signal from wind noise.

2.4 Summary

This chapter presents an extensive literature survey on the generation and reduction of wind noise. In Section 2.1, the background of the energy cascade theory in turbulence is introduced first, and then the seminal research on the turbulent pressure fluctuations was summarized in Section 2.1.1, which provides the fundamental theories for the following investigations of wind noise spectra in Section 2.1.2. Based on the knowledge in this section, two theoretical models are presented in Chapter 3 to describe the wind noise spectra in large and small Reynolds number turbulent flows, respectively.

In Section 2.2, the major physical structures which are widely used in outdoor acoustic measurements for wind noise reduction are surveyed, including the small spherical porous microphone windscreens in Section 2.2.1, the semi-spherical shell windscreens in Section 2.2.2, and the large spatial filters and wind fence enclosures in Section 2.2.3. The spatial filters and wind fence enclosures are large in size and difficult to transport and install, although they showed better wind noise reduction in the infrasonic range. While the small spherical porous microphone windscreens have been widely studied both experimentally and numerically, the wind noise reduction mechanism is still unclear yet. This section provides the background knowledge for the work in Chapter 4, which is devoted to the investigation of the wind noise reduction mechanism of porous microphone windscreens.

Finally, the signal processing methods that have been used for wind noise reduction are summarized in Section 2.3. The coherence structure of the wind noise in the low frequency range makes it challenging to extract the desired sound signal from wind noise with the conventional planar microphone array. This motivates the work in Chapter 5, where a rigid

spherical microphone array is utilized to reduce wind noise in the spherical harmonics domain.

To develop a new compact acoustic measurement system that is insensitive to wind noise, the following research questions are identified:

- What is the generation mechanism of wind noise?
- What is the wind noise reduction mechanism of porous microphone windscreens?
- What are the key factors determining the wind noise reduction of existing windscreens?
- What are the main difference between wind noise signals and how to distinguish them with signal processing techniques?

3 Wind noise spectra

The work presented in this chapter has been published in two papers in *The Journal of the Acoustical Society of America*, i.e., Zhao et al. (2016), J. Acoust. Soc. Am. **140**, 4178-4182, and Zhao et al. (2017), J. Acoust. Soc. Am. **142**, 3227-3233. Please see Appendix A for details.

3.1 Introduction

Wind noise is the pressure fluctuations caused by turbulence around microphones, which has been widely studied, as summarized in Section 2.1 with a detailed literature review. Pressure fluctuations in turbulent flows are usually denoted by the pressure structure function in the spatial domain, which describes the spatial relationship between pressures at two locations by [28]

$$D_p(r) = \left\langle \left(p(x) - p(x+r) \right)^2 \right\rangle \tag{3.1}$$

where $p(x)$ is the pressure at position x, r is the separation distance between two spatial locations, and $\langle\cdot\rangle$ denotes the ensemble average. The pressure structure function can be related to the pressure correlation function by [30]

$$D_p(r) = 2R_p(0) - 2R_p(r) \tag{3.2}$$

where $R_p(r) = \langle p(x)p(x+r)\rangle$ is the pressure correlation function. The structure function was shown to be computed at higher accuracy than the correlation function but with less data, hence was widely used in the research of turbulence [107].

The pressure spectrum can be calculated from the pressure structure function by [108]

$$P(k) = -\frac{1}{2\pi}\int_0^\infty D_p(r)\sin(kr)\,kr\,dr \tag{3.3}$$

where k is the wavenumber. Therefore, once the pressure structure function is known, the pressure spectrum can be readily obtained with the integral in Eq. (3.3). According to the

energy cascade theory mentioned in Section 2.1.1, the turbulence can be considered to be composed of three ranges with turbulent eddies of different sizes, i.e., the energy-containing range, the inertial range, and the dissipation range. Hill and Wilczak [28] proposed a theoretical model to relate the pressure structure function to the fourth-order velocity structure function based on the Poisson equation in Eq. (2.1), and derived the asymptotic form of the pressure structure function in the energy-containing range, the inertial range and the dissipation range, respectively.

In the inertial range, where the separation distance r is much smaller than the size of the largest eddy but much larger than the size of the smallest eddy, the eddy motions are solely determined by the energy dissipation rate. The pressure structure function in this range increases with the separation distance according to an exponent of 4/3, which can be written in a universal form as [28],

$$D_p(r) \approx C_p \varepsilon^{4/3} r^{4/3} \tag{3.4}$$

where C_p is a constant and ε is the energy dissipation rate. In the existing research that focused on the inertial range, Eq. (3.4) was substituted into Eq. (3.3) to calculate the pressure spectrum in the inertial range, i.e., [28]

$$P(k) \approx 0.328 C_p \varepsilon^{4/3} k^{-7/3} \tag{3.5}$$

This inertial range pressure spectrum with a −7/3 power law is consistent with Kolmogorov's dimensional analysis and previous theoretical models [26,31], and has been validated by many simulations and experimental results when the Reynolds number is sufficiently large [109,110]. Unfortunately, the pressure spectrum in the energy-containing range and the dissipation range cannot be obtained directly from the integral Eq. (3.3). This chapter presents two theoretical models to extend the pressure spectrum to higher frequencies in the dissipation range and lower frequencies in the energy-containing range.

3.2 Wind noise spectra in large Reynolds number turbulent flows

The existing theories focus on the inertial range and assume that the pressure spectrum with the −7/3 power law is also valid for the higher frequency region in the dissipation range. However, recent numerical simulations and experimental results showed that the pressure spectrum falls off much faster than the −7/3 power law at higher frequencies, but no theory exists for predicting the pressure spectrum in the dissipation range [109,110]. To describe the pressure spectrum in the higher frequency region, a pressure structure function model that incorporates both the inertial and the dissipation ranges is proposed, from which the pressure spectrum extending to the dissipation range can be obtained. Existing simulation and measurement data from the literature and wind noise spectra measured outdoors are used to validate the proposed pressure structure function model and the obtained pressure spectrum.

3.2.1 Theoretical model

In the dissipation range, the pressure structure function for small separation distance r can be approximated as [28,30]

$$D_p(r) \approx \frac{1}{3} A r^2 \tag{3.6}$$

where $A = \int_0^\infty y^{-3} D_{1111}(y)\, dy$ is independent of r [111], $D_{1111} = \langle (u(x) - u(x+r))^4 \rangle$ is the fourth order longitudinal velocity structure function, u is the longitudinal velocity and the subscript number 1 denotes the longitudinal direction. Eq. (3.6) shows that in the dissipation range, the square of the pressure difference at two spatial locations increases with the squared separation distance and increases at a faster rate than that in the inertial range shown in Eq. (3.4).

Unfortunately, the pressure spectrum in the dissipation range cannot be obtained by directly substituting Eq. (3.6) into Eq. (3.3), because the integral does not converge [112]. To

predict the pressure spectrum in a wider range, a pressure structure function model that incorporates both the inertial range (Eq. (3.4)) and the dissipation range (Eq. (3.6)) is proposed as

$$D_p(r) \approx \frac{1}{3} \frac{Ar^2}{\left[1+\left(r/r_\mathrm{d}\right)^2\right]^{1/3}} \tag{3.7}$$

where $r_\mathrm{d} = (3C_p\varepsilon^{4/3}/A)^{3/2}$ denotes the transition distance from the inertial range to the dissipation range in the pressure structure function, and can be obtained by equating Eq. (3.4) to Eq. (3.6). Previous results from experiments showed that the transition between the inertial range and dissipation range occurs at about $8.74\eta < r_\mathrm{d} < 11.25\eta$, where η is the Kolmogorov scale of the smallest eddies [113]. For $r >> r_\mathrm{d}$, Eq. (3.7) approaches Eq. (3.4) in the inertial range while for $r << r_\mathrm{d}$, Eq. (3.7) approaches Eq. (3.6) in the dissipation range.

By substituting Eq. (3.7) into Eq. (3.3), the pressure spectrum can be obtained [113],

$$P(k) = \frac{2^{\frac{1}{6}} A r_\mathrm{d}^{\,3}}{6\sqrt{\pi}\,\Gamma\left(\frac{1}{3}\right)} \left[\frac{4}{3} (kr_\mathrm{d})^{-\frac{1}{6}} K_{\frac{13}{6}}(kr_\mathrm{d}) + (kr_\mathrm{d})^{\frac{5}{6}} K_{\frac{7}{6}}(kr_\mathrm{d}) \right] \tag{3.8}$$

where $\Gamma()$ is the gamma function, and $K_n()$ is the second kind modified Bessel function of order n, which can be expanded in asymptotic forms as [114]

$$K_n(z) \approx \begin{cases} \frac{1}{2}\Gamma(n)\left(\frac{1}{2}z\right)^{-n}, & z << 1 \\ \left(\frac{\pi}{2}\right)^{\frac{1}{2}} z^{-\frac{1}{2}} e^{-z}, & z >> 1 \end{cases} \tag{3.9}$$

Applying Eq. (3.9) to Eq. (3.8), the asymptotic form of the pressure spectrum can be obtained

$$P(k) \approx \begin{cases} \dfrac{2^{\frac{7}{3}} A\Gamma\left(\dfrac{13}{6}\right) r_d^{\,3}}{9\sqrt{\pi}\Gamma\left(\dfrac{1}{3}\right)} (kr_d)^{-\frac{7}{3}}, & kr_d << 1 \\ \dfrac{2^{\frac{1}{6}} A r_d^{\,3}}{12\Gamma\left(\dfrac{1}{3}\right)} (kr_d)^{\frac{1}{3}} e^{-kr_d}. & kr_d >> 1 \end{cases} \tag{3.10}$$

Eq. (3.10) shows that the transition between the inertial range and the dissipation range occurs at $k = 1/r_d$ in the pressure spectrum, and the inertial range and the dissipation range in the wavenumber space can be denoted as $k << 1/r_d$ and $k >> 1/r_d$, respectively. In the inertial range ($kr_d << 1$), the pressure spectrum obtained from the proposed model shows the –7/3 power law, which is consistent with previous studies. In the dissipation range ($kr_d >> 1$), the pressure spectrum follows the exponential decay, falling off much faster than the –7/3 power law, consistent with the simulation and experiment results in the literature [109,110].

In the next section, the proposed pressure structure function model and the obtained pressure spectrum will be validated with data from existing literature and wind noise spectra measured outdoors in a car park.

3.2.2 Verifications

Figure 3.1 compares the proposed pressure structure function model in Eq. (3.7) with existing experimental results from Ref. [115]. Because the values of η and r_d were not given in the reference with the experimental results, the proposed pressure structure function model was fitted to the experimental results in Figure 3.1 with $r_d = 10\eta$. The experimental results in Figure 3.1 are from the turbulent water flows between a pair of counter-rotating disks, which can be described by the incompressible viscous Navier-Stokes equations [115]. The proposed model is based on the structure functions derived from the Poisson equation, which is also deduced from the incompressible viscous Navier-Stokes equations. Therefore, the experimental results can be used to validate the proposed model. Different from previous

theories that assume that the inertial range ($D_p(r) \sim r^{4/3}$) extends to an infinitely small separation distance, the proposed model in Eq. (3.7) shows better agreement in Figure 3.1 for small separation distances, where eddies in the dissipation range dominate the pressure structure function.

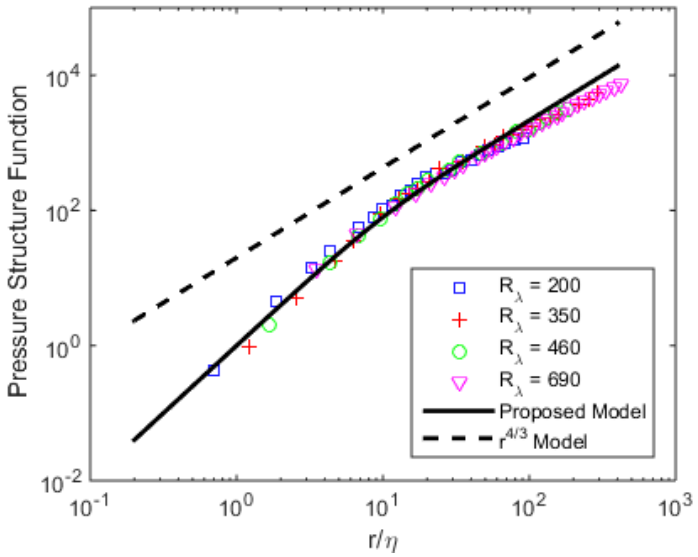

Figure 3.1 Comparison of the proposed pressure structure function model in Eq. (3.7) with the experimental results from Ref. [115]. The abscissa is normalized with the Kolmogorov scale η.

The pressure spectrum obtained from the proposed model in Eq. (3.8) is compared with the existing Direct Numerical Simulation (DNS) and experimental results in Figure 3.2 [109,110]. The experimental results in Figure 3.2(b) were measured on the centre line in the free jet from a small wind tunnel with a 40×40 mm^2 nozzle and a large wind tunnel with a 400×700 mm^2 nozzle. The Taylor microscale Reynolds number is in the range of $200 \leq R_\lambda \leq 1200$. The pressure fluctuations were measured with a standard 1/4" condenser microphone for $R_\lambda < 350$, and with a small piezoresistive transducer for $R_\lambda > 350$ [110]. The values of η and r_d were not given in the literature with the simulation and experimental results, therefore

the obtained pressure spectrum in Eq. (3.8) was fitted to the experimental results in Figure 3.2 with $r_d = 10\eta$.

Figure 3.2 shows that the simulated and measured pressure spectra decay following the –7/3 power law in the inertial range at about $k\eta < 0.2$, but they begin to fall off rapidly at about $k\eta > 0.2$, which deviates from the conventional $k^{-7/3}$ model. The pressure spectrum obtained from the proposed model in Eq. (3.8) is consistent with the simulation and experimental results in this rapid decay region in the dissipation range as well as the –7/3 power law in the inertial range, which cannot be predicted with the traditional asymptotic form pressure spectrum.

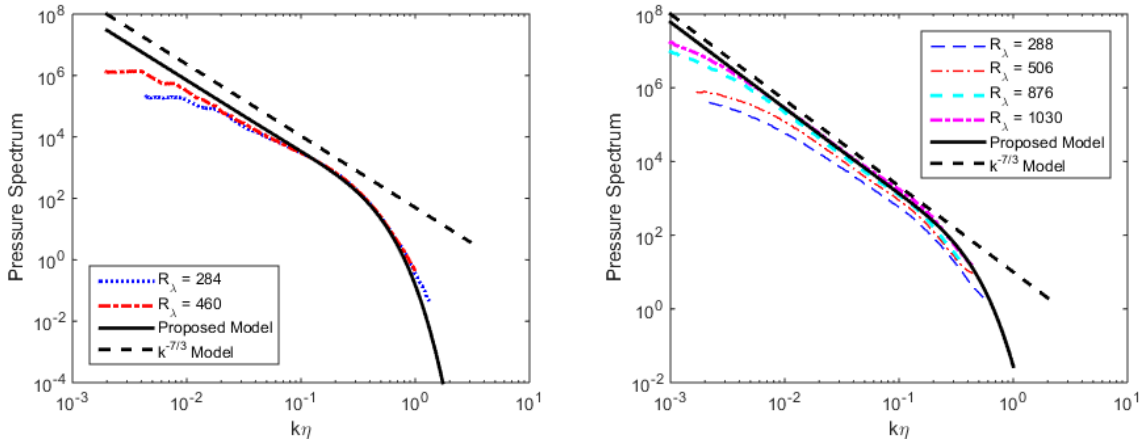

(a) (b)

Figure 3.2 Comparison of the pressure spectrum obtained from the proposed model in Eq. (3.8) with existing results, (a) DNS simulations from Ref. [109], and (b) wind tunnel experimental results from Ref. [110]. The abscissa is normalized with the Kolmogorov scale η.

To validate the pressure spectrum obtained from the proposed model, outdoor wind noise spectra were measured at different wind speeds. The experiments were carried out at dawn on

8th October 2015, at a car park in Taiwan, where there were no obstacles or reflective surfaces nearby, as shown in Figure 3.3. The wind speed was measured with a WindSonic Ultrasonic Wind Sensor anemometer, and wind noise spectra were measured with an unscreened RION NL32 Type UC-53A 1/2" microphone. The anemometer and the microphone were mounted at the same height, about 1.2 m above the ground, with a horizontal distance of around 0.5 m. The anemometer and the microphone were both connected to a RION DA-20 multi-channel processor.

The measurement lasted 30 minutes and both the wind speed and the one-third octave band sound pressure level up to 16 kHz were logged every second. The measurement results were originally in one-third octave bands, thus the narrow band spectrum of the conventional $k^{-7/3}$ model and the pressure spectrum obtained from the proposed model in Eq. (3.8) were converted to one-third octave band spectra to compare with the measured wind noise spectra. The narrow band wavenumber pressure spectrum in Eq. (3.8) was first converted to the narrowband frequency pressure spectrum by $P(f) = (U/2p)P(k)$, where U is the mean wind speed [5]. Then the narrow band frequency pressure spectrum was the converted to the one-third octave band pressure spectrum by $P(f_n) = \sum_{f_{n1}}^{f_{n2}} P(f)$ where f_n is the centre frequency, and f_{n1} and f_{n2} are the lower and upper limits of the n-th one-third octave band, respectively. In the calculation of the summation, a 1 Hz frequency resolution of the narrow band pressure spectrum was used.

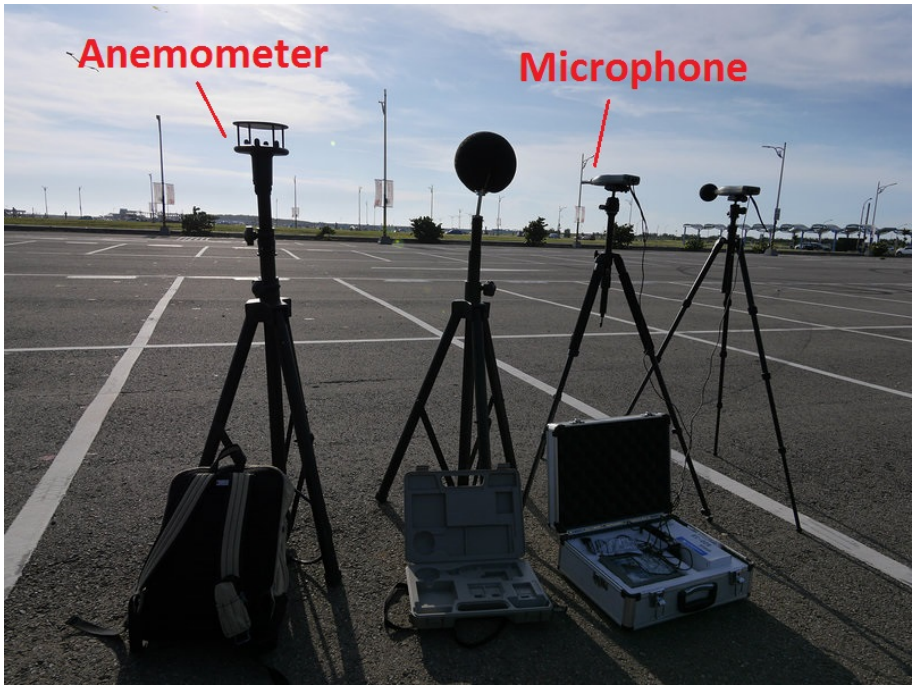

Figure 3.3 The experimental setup of the outdoor wind noise measurements at a car park in Taiwan.

The one-third octave band sound pressure spectrum obtained from the proposed model in Eq. (3.8) was fitted to the measurement results from the unscreened microphone in Figure 3.4 with r_d = 6.8 mm and r_d = 5.6 mm for the mean wind speeds of U = 4.5 m/s and U = 5.5 m/s, respectively. The corresponding transition frequency between the inertial range and the dissipation range can be calculated with the Taylor's frozen turbulence hypothesis, i.e., $f_d = U/2\pi r_d$, as illustrated by the black arrows in Figure 3.4. That is, f_d = 105 Hz and 156 Hz correspond to the mean wind speeds of U = 4.5 m/s and 5.5 m/s, respectively. The measured wind noise spectra in Figure 3.4 were averaged around $U \pm 0.5$ m/s for the mean wind speed U and the vertical bars indicate the standard deviation.

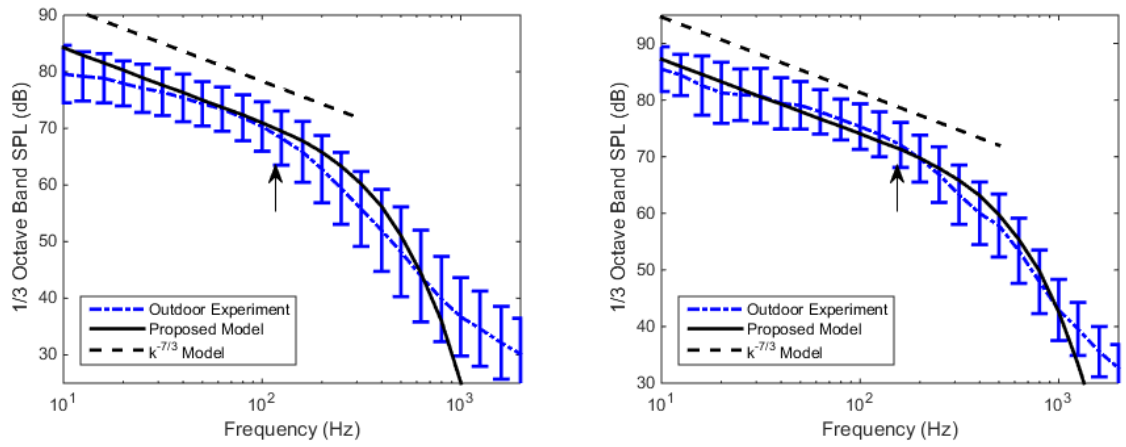

Figure 3.4 Comparison of the pressure spectrum obtained from the proposed model in Eq. (3.8) with the outdoor experimental results at the mean wind speeds of (a) U = 4.5 m/s and (b) U = 5.5 m/s. The black arrows denote the transition from the inertial range to the dissipation range.

Figure 3.4 shows that in the inertial range to the left side of the black arrow, the outdoor wind noise spectra are consistent with the conventional $k^{-7/3}$ model; however, in the dissipation range to the right side of the black arrow the measured outdoor wind induced noise spectra fall off much more rapidly and deviate from the conventional $k^{-7/3}$ model. In contrast, the pressure spectra obtained from the proposed pressure structure function model in Eq. (3.8) agree well with the measured outdoor wind noise spectra across the measured frequency range from 10 Hz to 1000 Hz.

The outdoor wind noise spectra in Figure 3.4 were measured with an unscreened 1/2" microphone, which might generate wake behind and hence alter the wind-induced noise [43]. However, it was shown that the dominant source of pressure fluctuations at the microphone outdoors is the intrinsic turbulence in the flow, rather than the fluctuating wake [15].

Therefore the effect of the microphone on the outdoor wind noise is not taken into account in Figure 3.4.

3.2.3 Discussions

This section proposes a pressure structure function model that incorporates both the inertial range and the dissipation range to extend the pressure spectrum to the dissipation range in turbulent flows. Comparisons with the literature data and wind noise spectra measured outdoors in a car park were found to match well with the proposed pressure structure function and the obtained pressure spectrum in both the inertial and the dissipation ranges.

The limitation of the current work is that the proposed pressure structure function model is only valid for sufficiently large Reynolds number because the inertial range with $D_p(r) \sim r^{4/3}$ (or equivalently $P(k) \sim k^{-7/3}$) always exists in Eq. (3.7). This might be not true for the small Reynolds number turbulent flows. Recent numerical simulation and experimental results showed that the inertial range with the −7/3 power law cannot be observed when the Reynolds number is small [109,110].

The numerical simulations by Gotoh and Fukayama [109] show that the −7/3 power law can be observed when the Taylor microscale Reynolds number is larger than 284, while the experimental results in wind tunnels by Tsuji and Ishihara [110] confirm the −7/3 power law when the Taylor microscale Reynolds number is larger than 600. Meldi and Sagaut [116] argued that a Taylor microscale Reynolds number larger than 10^4 is necessary to observe the −7/3 power law in the pressure spectrum. It is still not known whether there exists a cutoff value of the Reynolds number such that the −7/3 power law can be observed above this value.

It has been shown that the Reynolds number in atmospheric turbulence is usually large enough for the inertial range to be observed [117]. Therefore, the pressure spectrum obtained

from the proposed pressure structure function model could be used for predicting the noise spectra induced from outdoor wind.

In the comparison of the proposed pressure structure function and the obtained pressure spectrum with the simulations and experimental results, the proposed model was fitted to the measured data because the amplitude coefficient A and transition distance r_d in Eqs. (3.7) and (3.8) are not available. In theory, both A and r_d can be calculated from velocity fluctuations, which can be measured by a hot wire anemometer system. Because we did not have access to such systems while the research was conducted, the velocity fluctuations were not measured in this thesis. This will be pursued in the future work.

3.3 Wind noise spectra in small Reynolds number turbulent flows

Besides the above outdoor investigations, wind noises are often measured in indoor environments such as wind tunnels. Recent measurements of wind noise in a small anechoic wind tunnel showed that the noise spectrum does not change significantly in the lower frequency region but decays much faster than the −7/3 power law in the higher frequency region, which is inconsistent with wind noise measured outdoors [48,49]. This may be due to the smaller Reynolds number of the wind tunnel flows than those found in atmospheric flows. As mentioned above, simulations and experimental results found no inertial range with the −7/3 power law in the pressure spectra when the Reynolds number is small [109,110].

The Reynolds number based on the Taylor microscale in the atmosphere varies from 4250 to 19500, which is more than 10 times larger than that in the wind from a fan at low wind speeds [118]. Although wind noise spectra measured in outdoor atmospheric turbulence with a sufficiently large Reynolds number can be described by Eq. (3.8) in the inertial and dissipation ranges in Section 3.2, no theory exists to predict the pressure spectrum in small Reynolds number turbulent flows where the inertial range is absent.

To better understand the wind noise measured in indoor environments, such as that under fans or air conditioner outlets, this section proposes a pressure structure function model that incorporates the energy-containing and dissipation ranges to predict the pressure spectrum for small Reynolds number turbulent flows. Existing literature data and measurement results from indoor fan tests are used to validate the proposed pressure structure function model and the obtained pressure spectrum.

3.3.1 Theoretical model

Based on the asymptotic model derived from the Poisson equation by Hill and Wilczak [28], the pressure structure function is twice the pressure variance for the homogeneous and isotropic turbulence in the energy-containing range with sufficiently large separation distance, as given by

$$D_p(r) \approx 2\sigma_p{}^2 = 2\frac{\langle P^2 \rangle}{\rho^2} \tag{3.11}$$

where the pressure variance $\sigma_P{}^2$ is a constant for a certain turbulent flow.

It was proposed in Section 3.2 to combine the pressure structure function in the inertial range in Eq. (3.4) and the dissipation range in Eq. (3.6) so that the pressure spectrum can be extended to the dissipation range. However, this model is only valid for turbulent flows with sufficiently large Reynolds numbers such that the inertial range always exists. For turbulent flows with small Reynolds numbers, there is no inertial range [109,110]. To accurately describe the pressure spectrum in such flows, this section proposes an alternative pressure structure function model that incorporates the energy-containing range in Eq. (3.11) and the dissipation range in Eq. (3.6), namely

$$D_p(r) \approx \frac{1}{3}\frac{Ar^2}{\left[1+\left(r/r_{\mathrm{L}}\right)^2\right]} \tag{3.12}$$

where $r_L = (6\sigma_P^2/A)^{1/2}$ denotes the transition from the dissipation range to the energy-containing range, and can be obtained by equating Eq. (3.11) to Eq. (3.6). For $r >> r_L$, Eq. (3.12) approaches Eq. (3.11) in the energy-containing range while for $r << r_L$, Eq. (3.12) approaches Eq. (3.6) in the dissipation range.

Substitute Eq. (3.12) into Eq. (3.3), the pressure spectrum can be obtained as

$$P(k) = \frac{A r_L^3}{6\pi} e^{-kr_L} \tag{3.13}$$

The transition between the energy-containing range and the dissipation range occurs at $1/r_L$ in the wavenumber space. In the energy-containing range ($kr_L << 1$), the exponential term approaches to 1 so the proposed pressure spectrum model approaches a constant and does not vary with the wavenumber (or equivalently frequency), which is consistent with the measurement results of the wind noise spectra in a small anechoic wind tunnel [48,49].

In the dissipation range ($kr_L >> 1$), the pressure spectrum falls off rapidly as the exponential decay, which is consistent with the dissipation range spectrum in Eq. (3.9) in Section 3.2. The value of r_L depends on the constant A and the pressure variance σ_P^2 by $r_L = (6\sigma_P^2/A)^{1/2}$. The pressure variance can be calculated from the measured pressure fluctuations. The constant A is determined by the fourth order longitudinal velocity structure function. Therefore, the calculation of the exact value of the constant A needs accurate measurement of the longitudinal velocity at two spatial locations with various separation distances.

The physical meaning of the obtained turbulent pressure spectrum for small Reynolds number turbulent flows can be explained based on the energy cascade theory [24]. In turbulent flows, the largest eddies contain most of the kinetic energy whereas the smallest eddies convert the kinetic energy to thermal energy via the viscous dissipation. The intermediate size eddies in between are responsible for the kinetic energy transfer from the largest eddies to the smallest eddies, which is called the inertial range. The width of the inertial range depends on the difference between the size of the largest and smallest eddies.

For turbulent flows with very large Reynolds number, such as the atmospheric turbulence, the largest eddies in the energy-containing range can be in hundreds of meters while the smallest eddies in the dissipation range is the order of millimeters, therefore a wide inertial range can be observed in the pressure spectrum [119]. However, for the turbulent flows with small Reynolds number, such as the wind from fans used in this section, the largest eddies is the order of centimeters (determined by the fan blade length ~ 10 cm), which is much smaller than the atmospheric turbulence. In this case, the kinetic energy transfer to the smallest eddies and is dissipated into heat quickly, so there is no inertial range with the $k^{-7/3}$ law in the pressure spectrum.

The proposed pressure structure function model in Eq. (3.12) and the obtained pressure spectrum in Eq. (3.13) will be validated with both the existing numerical and experimental data from literature as well as the measured wind noise from an axial fan in next section.

3.3.2 Validations

The proposed pressure structure function model for small Reynolds number turbulent flows in Eq. (3.11) is compared with the experimental results in Ref [111] in Figure 3.5. The values of η and r_L were not given in the literature with the experiment results, so the proposed pressure structure function model in Eq. (3.12) was fitted to the experimental results in Figure 3.5 with $r_L = 30\eta$. It can be observed that for small Reynolds number turbulent flows, existing theories that assume $D_p(r) \sim r^{4/3}$ cannot describe the pressure structure function, whereas the proposed pressure structure function model in Eq. (3.12) shows good agreement in both the dissipation range with $D_p(r) \sim r^2$ for small separations and in the energy-containing range where $D_p(r)$ tends to constant for large separations. It is noteworthy that there is no inertial range with $D_p(r) \sim r^{4/3}$ in the experiment results because the Reynolds number is small.

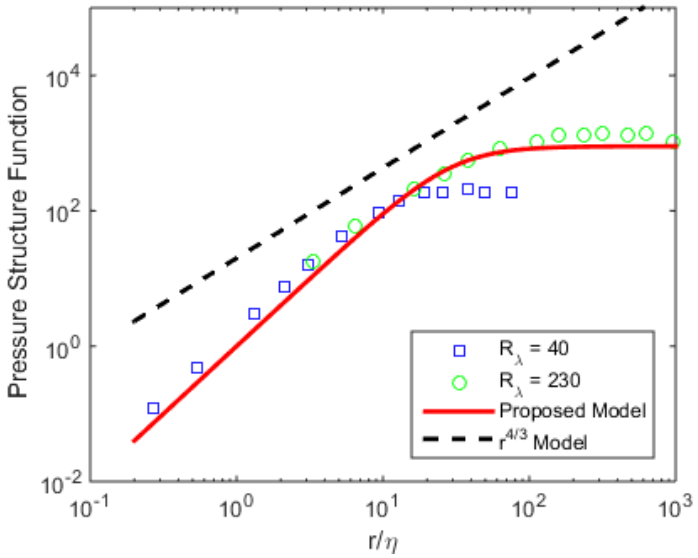

Figure 3.5 Comparison of the proposed pressure structure function model in Eq. (3.11) with the experimental results from Ref. [111]. The abscissa is normalized with the Kolmogorov scale η.

The pressure spectrum obtained from the proposed pressure structure function model in Eq. (3.13) is compared with the existing Direct Numerical Simulation (DNS) results in Figure 3.6 [109,120,121]. The pressure spectrum refers to the power spectrum of the pressure fluctuation and has a unit of Pa^2/Hz. The pressure spectrum normalized by the energy dissipation rate ε and the air viscosity ν, i.e., $P(k)/\varepsilon^{4/3}\nu^{-7/3}$, is read from the figures in the source literature, as shown in Figure 3.6. The values of the energy dissipation rate ε, the Kolmogorov scale η and the transition constant r_L were not given in the literature with the simulation results, so the pressure spectrum model in Eq. (3.13) was fitted to the simulation results in Figure 3.6 with $r_L = 10\eta$.

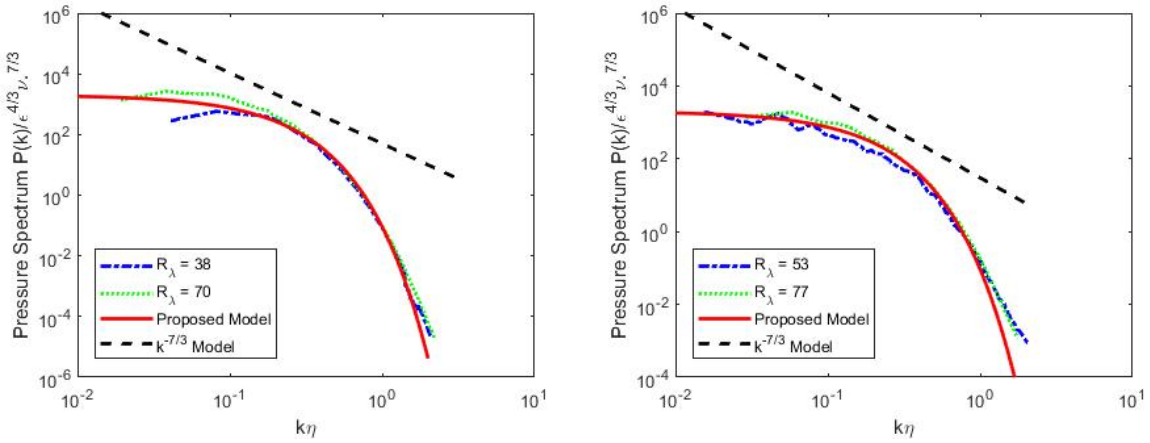

(a) (b)

Figure 3.6 Comparison of the pressure spectrum obtained from the proposed model in Eq. (3.13) with the existing DNS simulation results from (a) Ref [109], and (b) Refs. [120,121]. The abscissa is normalized with the Kolmogorov scale η.

Figure 3.6 shows that the simulated pressure spectrum tends to be constant in the lower frequency region while it decays rapidly in the higher frequency region. The pressure spectrum obtained from the proposed pressure structure function model in Eq. (3.13) agrees well with the simulation results, where the lower frequency region corresponds to the energy-containing range and the higher frequency region corresponds to the dissipation range. There is no inertial range in the simulation results due to the small Reynolds number, so the traditional $k^{-7/3}$ model is not valid in this case. The pressure spectra in the turbulent flows with small Reynolds numbers are predicted by the pressure spectrum obtained from the proposed pressure structure function model in Eq. (3.12), which cannot be obtained with the traditional asymptotic form pressure structure function.

To further validate the pressure spectrum obtained from the proposed pressure structure function model, the wind noise spectra from a fan were measured in the SIAL sound pod at RMIT University. The SIAL sound pod is a small room where the walls and floor are

finished with sound absorptive material. The fan and the microphone were about 0.8 m above the floor, with a separation distance of 0.5 m. The diagram and the photo of the experimental setup are shown in Figure 3.7.

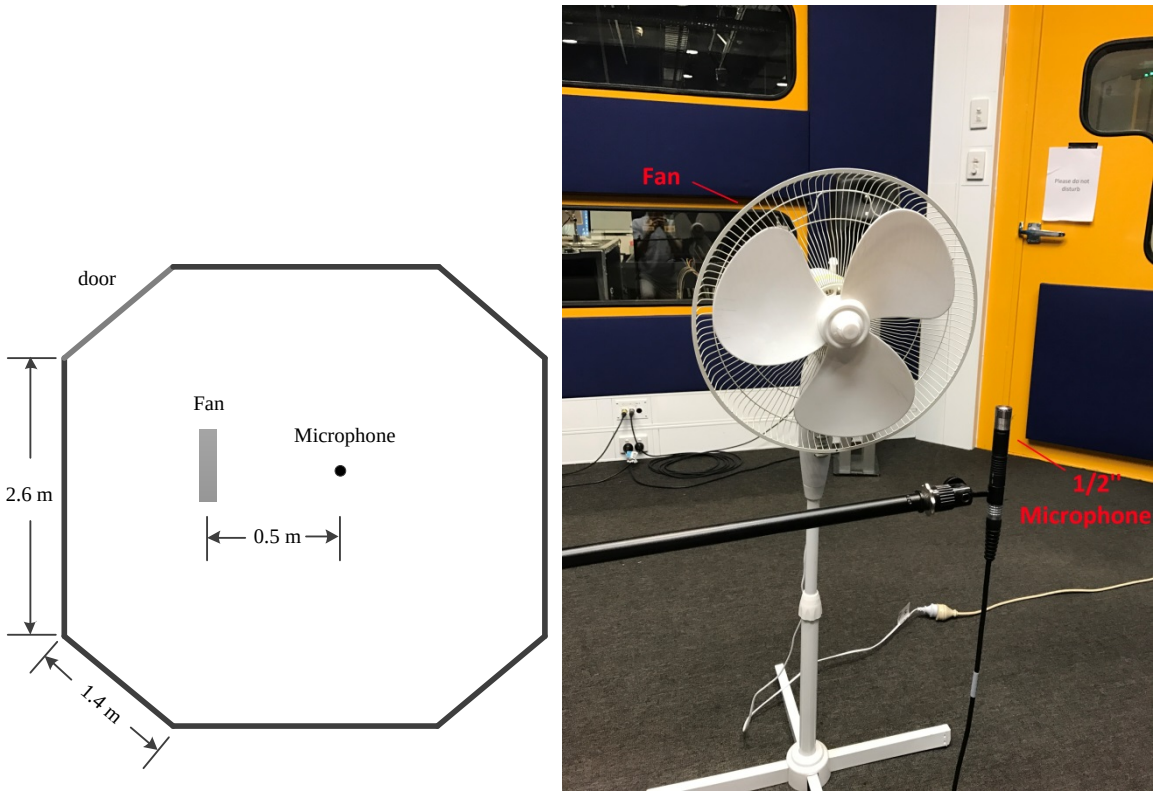

(a) (b)

Figure 3.7 (a) The diagram and (b) the photo of the experimental setup for indoor wind noise measurement with an axial fan.

The wind noise was measured with a B&K Type 4189 prepolarized free field 1/2" microphone whose frequency response is 2.8 Hz ~ 20 kHz, and a G.R.A.S Type 40BF 1/4" free field microphone, whose frequency response is 10 Hz ~ 40 kHz, respectively. The 1/2" microphone was connected to the B&K Type 2270 Analyser via a B&K Type ZC 0032 Preamplifier. The system was calibrated with a B&K Type 4231 calibrator. The 1/4" microphone was connected to a ZOOM H6 recorder via a G.R.A.S. Type 26AC preamplifier

and a G.R.A.S. Type 12AA power module. The system was calibrated with a G.R.A.S. Type 42AA Pistonphone. The mean wind speed was measured with a DIGITECH QM1646 Hand-held Anemometer by placing the anemometer at the position of the microphone, facing the axis fan.

To confirm the measured noise spectra is caused by wind from the fan when the microphone is placed inside the air flow, the 1/2" microphone was placed in front of the fan (inside the flow) and behind the fan (outside the flow) to measure the wind and mechanical noise of the fan, respectively. In the experiment, the fan ran at its highest speed and the mean wind speed around the microphone was about 4.2 m/s. The Reynolds number based on the dimension of the fan can be estimated as $Re = UD/\nu = 2.8\times10^4$ (U is the mean wind speed, D = 0.1 m is the length of the fan blade and ν is the air kinematic viscosity). The Taylor Reynolds number Re_λ is proportional to the square root of the Reynolds number, i.e., $Re_\lambda \approx (20Re/3)^{1/2} = 432$ [24]. The wind noise spectra were measured for 30 seconds with the 1/2" and 1/4" microphones, respectively. The pressure spectra were estimated by the Welch method with the MATLAB function pwelch. The 30 s recording was divided into 8 segments with a 50% overlap. Each segment was windowed with a Hamming window, and the modified periodograms were averaged the obtained the power spectral density estimate.

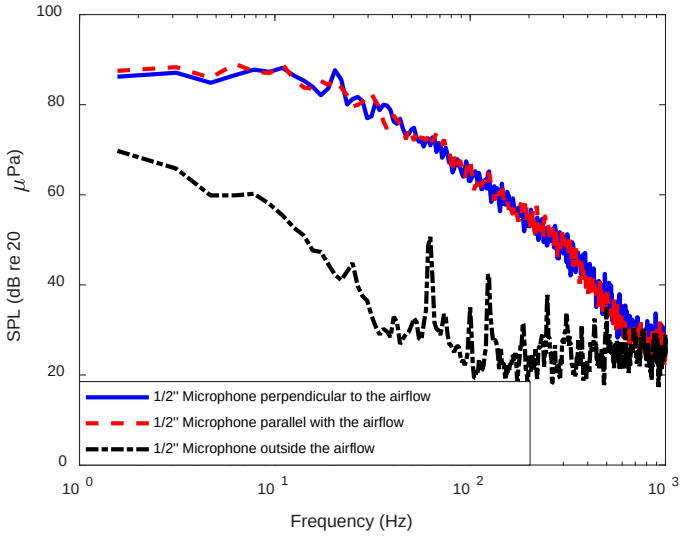

Figure 3.8 Comparison of the measurement results with the 1/2" microphone perpendicular and parallel to the air flow direction, where the black dash-dot line denotes the mechanical noise of the fan with the microphone placed outside the air flow.

The measurement results in Figure 3.8 indicate that the overall noise level is much lower when the 1/2" microphone is outside the flow, hence the measurement results with the microphone placed inside the air flow were primarily due to the turbulence in wind from the fan. The vertical axis in Figure 3.8 is the Sound Pressure Level (SPL) in dB scale with a reference pressure of 20 μPa. Figure 3.8 also shows the wind noise spectra measured with the 1/2" microphone parallel with the air flow direction, which is almost the same as that measured with the microphone perpendicular to the air flow direction. The following results were all measured with the microphone perpendicular to the air flow.

The measurement results with the 1/2" and 1/4" microphones placed inside and perpendicular to the air flow are compared with the obtained pressure spectrum in Eq. (3.13) and the conventional $k^{-7/3}$ model in Figure 3.9. The wind noise spectra are measured at wind speeds U = 1.0 m/s and U = 3.8 m/s, which correspond to the Taylor microscale Reynolds number of 210 and 410, respectively. The frequency response of the 1/4" microphone is 10

Hz ~ 40 kHz so the measurement results below 10 Hz are not accurate and not shown in Figure 3.9. The frequency response of the 1/2" microphone is 2.8 Hz ~ 20 kHz, therefore the measurement results with the 1/2" microphone are assumed to be accurate from 2.8 Hz to 10 Hz. In the frequency range above 10 Hz, the pressure spectrum measured with the 1/2" microphone deviates from that measured with the 1/4" microphone due to the interaction of the microphone with the air flow. The presence of the microphone has two effects on the measured pressure spectrum of the turbulent flow. The first is the wake generated behind the microphone [43] and the second is the averaging effect due to the finite size of the microphone diaphragm [122].

The wake generated by the microphone is usually much smaller than the intrinsic turbulence in the incoming flow, hence it can be neglected according to [15]. To confirm this claim, the wind noise was measured with the 1/2" microphone parallel to the air flow direction so that the wake was far from the diaphragm and had little influence on the measured wind noise spectrum. The measurement results with the 1/2" microphone parallel to and perpendicular with the airflow direction are compared in Figure 3.8, which shows that the measurement results were almost the same, hence we can conclude that the wake is negligible compared with turbulence in the incoming flow. In contrast, the averaging effect of the finite size of the microphone diaphragm can introduce undesirable errors in the measurements, especially in the higher frequency range with small eddies [122]. Therefore, the measurement results with the 1/4" microphone are considered to be more accurate than those from the 1/2" microphone in the higher frequency range above 10 Hz.

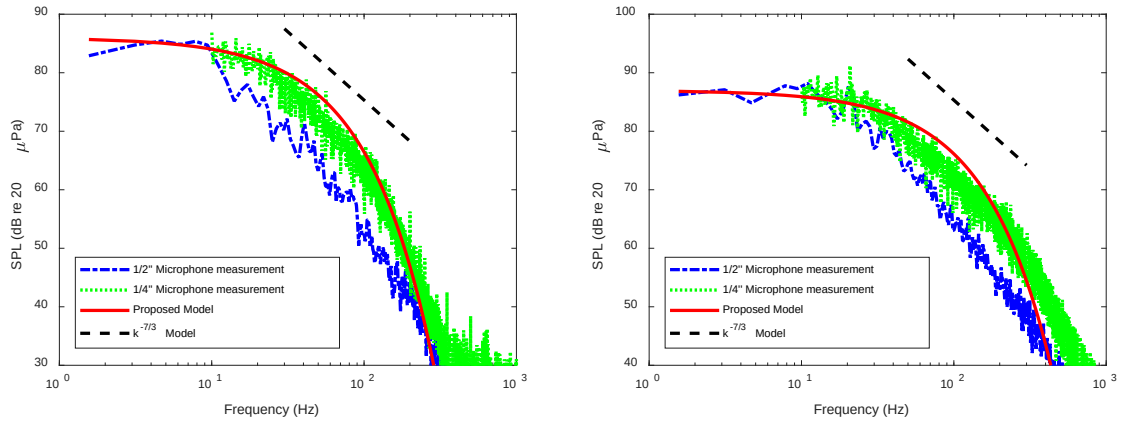

(a) (b)

Figure 3.9 Comparison of the obtained pressure spectrum in Eq. (3.12) with the indoor fan test results with a 1/2" microphone and a 1/4" microphone at (a) U = 1.0 m/s ($Re_\lambda \approx 210$) and (b) U = 3.8 m/s ($Re_\lambda \approx 410$).

It can be observed from Figure 3.9 that the pressure spectrum obtained from the proposed pressure structure function model agrees with the wind noise spectra measured with the 1/2" microphone below 10 Hz and that measured with the 1/4" microphone above 10 Hz, which is reasonable according to the above discussions. In contrast, the conventional $k^{-7/3}$ model fails to predict the wind noise spectra, especially in the lower frequency range. It is noteworthy that the calculation of the exact values of the constants r_L and A in Eq. (3.12) needs accurate measurements of the longitudinal velocity at two spatial locations with various separation distances, which requires two channel hot wire anemometers. However, no such hot wire equipment was available while the experiment was conducted, so the longitudinal velocity could not be obtained. In Figure 3.9 the proposed model is fitted to the measured wind noise spectra with $r_L = 1.67\times10^{-2}$ and $A = 4.0\times10^{5}$.

It is worth noting that the wind noise spectrum measured with the 1/4" microphone in Figure 3.9 shows an inertial range with the $k^{-7/3}$ law: 30 Hz ~ 100 Hz in Figure 3.9(a) and 50 Hz ~ 300 Hz in Figure 3.9(b). This is because the frequency range of the inertial range with

the $k^{-7/3}$ law depends on the Reynolds number. When the Reynolds number is very small, the inertial range is very small and even vanishes so that it cannot be observed in the pressure spectrum, such as the pressure spectrum in Figure 3.6 where the Taylor microscale Reynolds number Re_l is less than 77. This is the ideal case that can match the proposed pressure spectrum model.

As the Reynolds number increases, the inertial range extends to a larger range which is observable in the pressure spectrum, the frequency range of the $k^{-7/3}$ law increases with the Reynolds number, such as the wind noise spectrum in Figure 3.9 where the Taylor microscale Reynolds number is about 210 or 410, respectively. When the Reynolds number is as large as that in the atmospheric turbulence where the Taylor microscale Reynolds number is over 4250, the inertial range is so large that the pressure spectrum becomes dominant by the $k^{-7/3}$ law [5].

3.3.3 Discussions

The main contribution of this section is the proposed pressure structure function model in Eq. (3.12) and the derivation of the pressure spectrum in Eq. (3.13), which can be used to predict the pressure spectra in turbulent flows with small Reynolds numbers, such as the wind noise spectra caused by wind from fans and those measured in small anechoic wind tunnels. This is different from the previous models for outdoor wind noise spectra that focus on the inertial range [5], which assume that the Reynolds number is so large that the inertial range always exists.

The limitation of the proposed model is that it is only valid for turbulent flows with small Reynolds numbers where the inertial range is absent, and the effect of the Reynolds number is not explicitly expressed in the model. A good wind noise spectrum model should include all three turbulence ranges, the energy-containing range, the inertial range, and the dissipation range, in the pressure spectrum. Unfortunately, the mathematical derivation becomes too

complicated to obtain an explicit expression of the pressure spectrum if the pressure structure functions of all three ranges are combined into a single function and substituted in the integral equation in Eq. (3.3). Because of this difficulty and for the sake of simplicity, the inertial range is omitted in the proposed pressure structure function model in Eq. (3.12), so that an analytical form of the pressure spectrum could be obtained as Eq. (3.13).

Although the effect of finite Reynolds number is not accounted for in this model, it provides an explanation that the pressure spectrum in small Reynolds number turbulent flows approaches a constant in the lower frequency range and decays rapidly in the higher frequency range, which cannot be deduced from the conventional $k^{-7/3}$ model. The quantitative relationship between the finite Reynolds number and the frequency range with the $k^{-7/3}$ law in the pressure spectrum needs numerical integration of Eq. (3.3) and detailed measurements of wind noise spectra in turbulent flows with controlled Reynolds numbers, which will be investigated in the future.

3.4 Conclusions

This chapter proposed two theoretical models to predict the wind noise spectra for outdoor atmospheric turbulence with large Reynolds number and indoor fan generated turbulent flows with small Reynolds number, respectively.

Section 3.2 presents a pressure structure function model that incorporates both the inertial range and the dissipation range to extend the pressure spectrum to the dissipation range in turbulent flows. The proposed pressure structure function model and the obtained pressure spectrum were found to be consistent with existing experimental and numerical simulation results. For further validation of the proposed model, outdoor wind-induced noise was measured and comparisons with the pressure spectrum obtained from the proposed pressure structure function model were found to match well in both the inertial range and the

dissipation range. This model can be used to describe the wind noise spectra measured outdoors in atmospheric turbulence.

Section 3.3 proposes a pressure structure function model that combines the energy-containing and dissipation ranges, based on which the pressure spectra can be obtained for small Reynolds number turbulent flows where the inertial range is absent. The results show that the pressure spectra approach a constant in the lower frequency range in the energy-containing range but decay rapidly in the higher frequency range for the dissipation range. The proposed pressure structure function model and the obtained pressure spectra have been validated with both existing numerical and experimental results in the literature as well as indoor fan test measurement results. The pressure spectra obtained from the proposed pressure structure function model can be utilized to predict wind noise measured in indoor environments such as that from fans and wind tunnels.

Future work includes

- conducting detailed measurements of velocity fluctuations to calculate accurate values of the constant A and transition distances r_d and r_L in the proposed models;
- investigating the effect of finite Reynolds number on the wind noise spectra;
- studying the finite size effect of a microphone diaphragm on the measured pressure spectra; and
- investigating generation mechanism of turbulence which is the main source of wind noise.

4 Wind noise reduction mechanism of porous microphone windscreens

The work presented in this chapter has been published in two papers in *The Journal of the Acoustical Society of America*, i.e., Zhao et al. (2017), J. Acoust. Soc. Am. **142**, 2454-2463, and Zhao et al. (2018), J. Acoust. Soc. Am. **143**, 330-339, and presented at *INTER-NOISE 2017* in Hong Kong. Please see Appendix A for details.

4.1 Introduction

While porous microphone windscreens are widely used in both indoor and outdoor acoustic measurements, the noise reduction mechanism still lacks theoretical analyses. The impermeable rigid sphere model by Phelps [51] and Zheng and Tan [52] were too simplified and much different from practical situations. The numerical simulations by Xu et al. [27] modeled the porous microphone windscreens with a parameter flow resistivity to investigate the effect of the windscreen shape and viscous resistance on wind noise reduction.

In an alternative approach, this chapter investigates the wind noise reduction mechanism of porous microphone windscreens by accounting for both the viscous and inertial forces from the porous windscreens. In the simulations, the air flow outside the porous microphone windscreen is described by the Navier-Stokes equations for viscous incompressible flow [27],

$$\nabla \cdot \mathbf{u} = 0 \tag{4.1}$$

$$\frac{\partial \mathbf{u}}{\partial t} + (\mathbf{u} \cdot \nabla)\mathbf{u} = -\frac{1}{\rho}\nabla p + \nu \nabla^2 \mathbf{u} \tag{4.2}$$

where $\mathbf{u}$ is the velocity, p is the pressure, ρ is the fluid density and ν is the air viscosity. It is noteworthy that the turbulent flow is approximated as incompressible turbulence in Eqs. (4.1) and (4.2). The wind noise is actually the turbulent pressure fluctuations (pseudo-sound)

generated by the incoming flow on a microphone, while the sound waves measured at a microphone are compressible pressure disturbances.

The air flow inside porous microphone windscreen is governed by the continuity equation and the momentum conservation equation proposed by Nithiarasu et al. [123],

$$\nabla \cdot \mathbf{u} = 0 \tag{4.3}$$

$$\frac{1}{\phi}\frac{\partial \mathbf{u}}{\partial t} + \frac{1}{\phi^2}(\mathbf{u} \cdot \nabla)\mathbf{u} = -\frac{1}{\rho}\nabla p + \frac{\nu}{\phi}\nabla^2 \mathbf{u} - \frac{\nu}{K}\mathbf{u} - C|\mathbf{u}|\mathbf{u} \tag{4.4}$$

where ϕ is the porosity of the porous medium, $\mathbf{u}$ and p are the superficial (volume-averaged) velocity and pressure, respectively, K is the permeability of the porous medium, and C is the inertial coefficient. The derivation of Eq. (4.4) is based on the volume averaging technique. All quantities including the velocity, pressure, viscous and inertial coefficients in Eq. (4.4) are averaged over a representative elementary volume, which is much larger than any individual pore but is much smaller than the whole porous material (the porous windscreen in our case) [123]. The advantage of this generalized momentum conservation equation is that it can be reduced to the conventional Navier-Stokes equation when there is no porous media (both the viscous and inertial coefficients are 0 and the porosity is 1), so the Navier-Stokes solver can also be used for such equations.

The porous windscreen introduces two extra terms in the momentum conservation equation in Eq. (4.4) compared to the Navier-Stokes equation for the air flow without a porous medium. The third term on the right hand side of Eq. (4.4) is the Darcy term which represents the viscous forces resulting from the fluid-solid interaction along the surface of the pores in the porous medium. The fourth term on the right hand side of Eq. (4.4) is the Forchheimer term, which represents the inertial forces imposed on the fluid flow by the solid structure of the porous medium [124].

The physical mechanism of wind noise reduction by porous microphone windscreens was found to be the resistance forces caused by the porous windscreen on air flows to reduce the

fluctuation amplitude of the turbulent velocity and pressure [124]. The resistance forces consist of the viscous forces resulting from the viscous stresses along the fluid-solid interface of the pores and the inertial forces imposed on the fluid by the solid permeable medium. The viscous forces depend on the fluid viscosity and the permeability of the porous media *K*, while the inertial forces can be characterized by the inertial resistance coefficient *C*, which has the dimensions of length and is a function of the geometry of the media, the cell size, and the nature of the flow [125].

In this chapter, the effects of both viscous and inertial forces on the wind noise reduction of porous microphone windscreens are studied first by measuring the pressure fluctuations in the middle of the windscreens with a single microphone. Then two microphones are used to investigate the spatial structure of wind noise and the effect of porous windscreens on the wind noise structure. Experiments with a commercial axial fan are carried out to support the simulation results.

4.2 Viscous and inertial resistance to air flow due to porous windscreens

To study the effects of viscous and inertial forces on the wind noise reduction of porous microphone windscreens, the pressure fluctuations inside porous windscreens with various viscous and inertial coefficients are simulated, and the simulation results are analyzed and explained. The wind noise reduction by 5 different porous microphone windscreens is measured with a fan to verify the simulations results.

4.2.1 Simulation model

The diagram of the simulation model is shown in Figure 4.1(a), where the uniform air flow with a mean speed *U* enters the computation domain from the left boundary. The computation domain is 34*D* in the downwind direction and 10*D* in the crosswind direction.

An array of solid cylinders with diameter D is placed upstream to generate turbulence. The solid cylinder array is 4D from the flow inlet boundary and the interval between the solid cylinders is also D. The grey cylinder, 10D from the upstream solid cylinder array in the middle, denotes the microphone windscreen of diameter D_0, which is modelled as a porous medium. In the middle of the windscreen, a 1/2" microphone is modelled as a rigid cylinder, and the pressure averaged over the rigid cylinder is monitored to mimic the pressure fluctuations detected by the microphone.

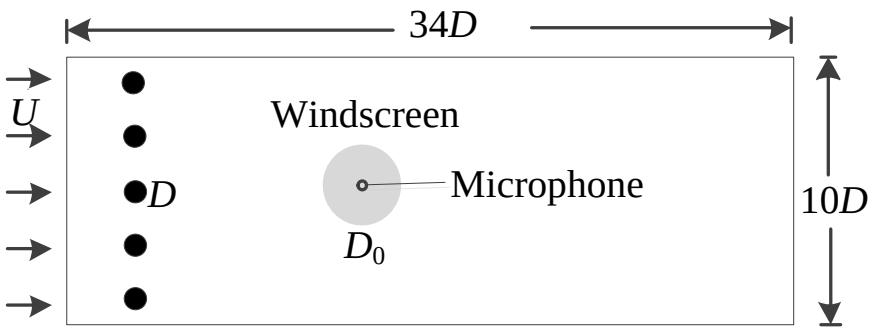

Figure 4.1 The diagram of the simulation model for porous windscreens with various viscous and inertial coefficients.

The models were built, and meshed in ANSYS Workbench 16.0. The air flow outside the porous microphone windscreen is described by Eqs. (4.1) and (4.2), and the air flow inside the porous microphone is determined by Eqs. (4.3) and (4.4), which were solved in FLUENT 16.0 by modeling the microphone windscreen as a “porous media zone” with the boundary condition of velocity and stress continuity at the windscreen surface. The boundary condition of the flow inlet was set to “velocity inlet”, the outlet boundary condition was set to “pressure outlet”, and the upper and lower boundaries were set as “wall”.

In the simulations, the wind speed at the inlet is U = 4 m/s, and the diameter of the upstream cylinder and the porous windscreen are D = 50 mm and D_0 = 90 mm, respectively.

The Reynolds number for the flow in the simulations can be estimated as $Re = UD/\nu = 1.3\times10^4$ (where $U = 4$ m/ is the mean flow speed, $D = 0.05$ m is the diameter of the upstream cylinders and $\nu = 1.511\times10^{-5}$ is the air kinematic viscosity at the temperature of 20 ^{o}C). The Reynolds number based on the Taylor microscale for the turbulent flow in the simulations is about $Re_\lambda \approx (20Re/3)^{1/2} = 294$.

To quantitatively examine the wind noise reduction performance of the windscreens, the Wind Velocity Reduction (WVR) and Wind Noise Reduction (WNR) as a function of frequency are defined in Eqs. (4.5) and (4.6), respectively.

$$WVR(f) = 10\log_{10}\frac{|u_0(f)|^2}{|u_{ws}(f)|^2} \quad \text{(dB)} \tag{4.5}$$

$$WNR(f) = 10\log_{10}\frac{|p_0(f)|^2}{|p_{ws}(f)|^2} \quad \text{(dB)} \tag{4.6}$$

where $u_0(f)$ and $p_0(f)$ are the incompressible turbulent velocity and pressure fluctuation without the windscreen at frequency f, and $u_{ws}(f)$ and $p_{ws}(f)$ are the corresponding incompressible turbulent velocity and pressure within the windscreen. The power spectral density is defined as the power per unit frequency, which can be calculated by [126]

$$P(f) = \mathrm{E}\left[\lim_{T\to\infty}\frac{1}{T}X(f)X^*(f)\right] \tag{4.7}$$

where E[·] denotes the expectation operator, the superscript * indicates the complex conjugate and $X(f)$ is the Fourier transform of the time domain signal $x(t)$ truncated within the time window T. In this thesis, the MATLAB function pwelch is used to estimate the power spectral density with the Welch method for both velocity and pressure fluctuations.

The overall WNR in a frequency range between f_1 and f_N is defined as

$$WNR = 10\log_{10}\frac{\sum_{f_1}^{f_N}\left|p_0(f_n)\right|^2}{\sum_{f_1}^{f_N}\left|p_{\mathrm{ws}}(f_n)\right|^2} \quad \text{(dB)} \tag{4.8}$$

The effect of the viscous and inertial resistance on wind noise reduction performance is simulated in the next section and the results are explained. It is noteworthy that throughout the text in this section, wind velocity and wind noise refer to the incompressible turbulent velocity and pressure fluctuations rather than the compressible acoustic particle velocity and pressure disturbances.

4.2.2 Simulation results

In the two dimensional simulations performed in this thesis, the pressure fluctuations were calculated from the Poisson equation in Eq. (2.1). The high Reynolds number means the flow is turbulent rather than laminar, therefore the Large Eddy Simulation (LES) with the Smagorinsky turbulence model was used. The simulation was run for 1 second. The meshsize was chosen based on the Courant–Friedrichs–Lewy (CFL) condition, i.e., $U\Delta t/\Delta x \leq 1$, where U is the flow velocity, Δt is the time step and Δx is the meshsize. The highest scale in the turbulence cascade should be much smaller than Δx. In the simulations, Δt is 0.1 ms (sampling rate 10 kHz), and U varies from 2 m/s to 14 m/s. Figure 4.2 shows the Power Spectral Density (PSD) of the pressure fluctuations as a function of the turbulent wavenumber ($2\pi/\xi$, where $\xi = U/f$ is the turbulent wave length) for various wind speeds. The "plateaus" at high wavenumber (corresponding to high frequency) above 1000 m^{-1} is due to the numerical noise, therefore the highest scale in the turbulence cascade is around 1000 m^{-1} in the simulations.

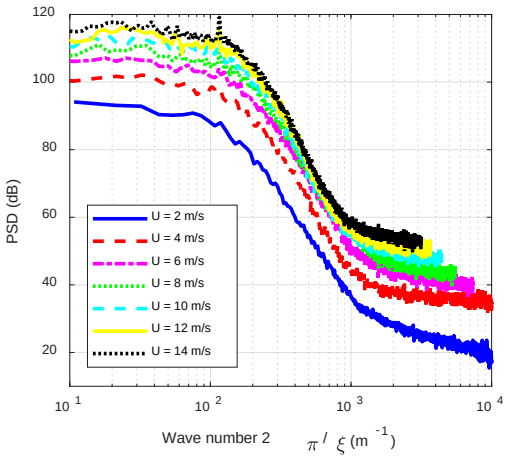

Figure 4.2 The Power Spectral Density (PSD) of the pressure fluctuations as a function of the turbulent wavenumber for various wind speeds.

Because the resistance on the air flow due to the porous windscreen consists of the viscous and inertial forces, the effect of the viscous and inertial forces on the wind noise reduction performance is investigated separately in two sets of simulations below.

A. The viscous effect

In the first set of simulations, a zero inertial coefficient is assumed so that no inertial force is applied on the air flow from the porous windscreen. In this case, the physical wind noise reduction mechanism of windscreens results only from the viscous forces on the air flow by the porous windscreen. This is actually the same scenario as the computational study in Ref. [27], where the flow resistivity is used to characterize the material viscous property. The flow resistivity σ is related to the viscous coefficient $1/K$ (K is the permeability) by $\sigma = \mu/K$, where μ is the air viscosity [27].

The simulation results of the wind velocity spectra and the wind noise spectra for various viscous coefficients are shown in Figure 4.3. The wind velocity and pressure level generally increase with wind speeds, and the wind speed U = 4 m/s is used in the simulations for consistency with the experimental conditions. It can be observed from Figure 4.3(a) that the

wind velocity inside the porous windscreen decreases with growing viscous coefficients 1/*K*. This is reasonable because for small viscous coefficients, the porous windscreen is highly permeable and has little effect on the incoming air flow, whereas the porous windscreen with a large viscous coefficient produces large viscous force on the air flow so the flow speed is damped heavily.

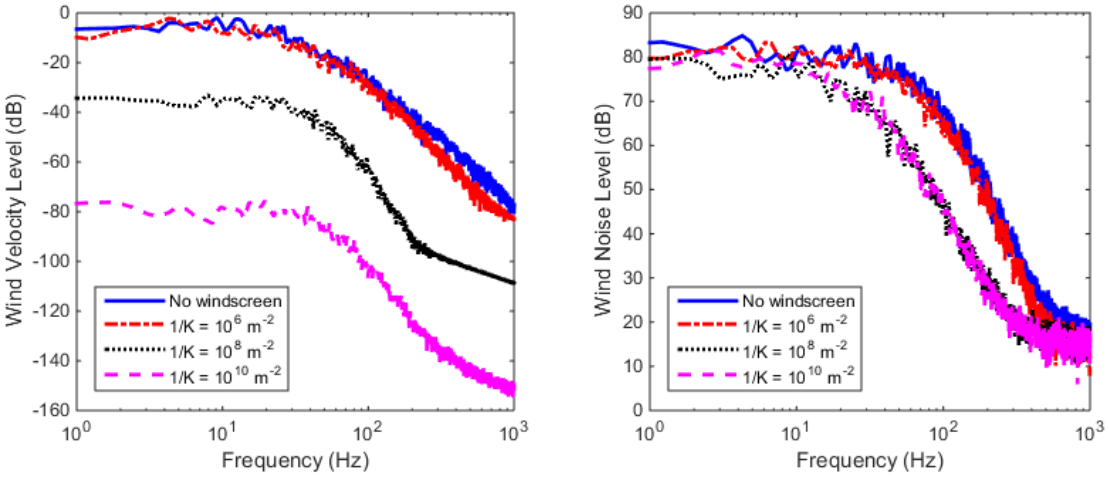

(a) (b)

Figure 4.3 (a) The wind velocity spectra and (b) the wind noise spectra for different viscous coefficients at the wind speed U = 4 m/s.

In contrast, Figure 4.3(b) shows that the wind noise level first decreases then slightly increases with the growing viscous coefficients. These results are consistent with the computational simulation in Ref. [27], where the windscreens with medium flow resistivity were found to have the most effective wind noise reduction performance. This can be more clearly observed from Figure 4.4(a), which shows the overall wind noise reduction (WNR) in a broad frequency range from 1 Hz to 1000 Hz. The WNR reaches its maximum when the viscous coefficient is around 10^8 m^{-2}, and decreases slightly afterward. This is also illustrated by Figure 4.4(b) for the WNR at different frequencies. The viscous coefficient is a quantity

for characterizing the viscous forces due to the fluid-solid interaction along the surface of the pores in the porous medium, which is related to the roughness of the pore surface.

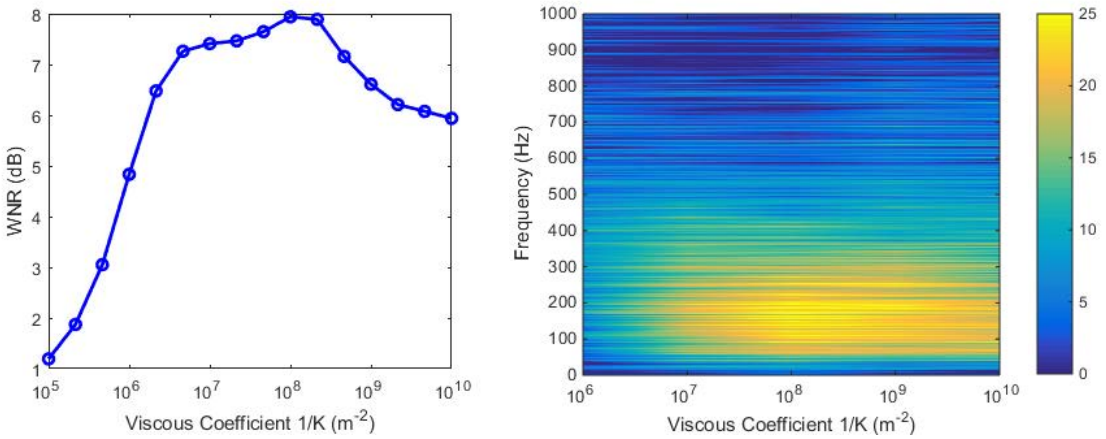

(a) (b)

Figure 4.4 (a) The overall Wind Noise Reduction (WNR) and (b) the WNR at different frequencies for 90 mm windscreens with different viscous coefficients at the wind speed U = 4 m/s.

The existence of the optimal viscous coefficient for porous windscreens on wind noise reduction can be explained physically. When there is no windscreen, the wind noise is primarily due to the turbulence in the incoming flow from the upstream solid cylinder array, as shown in Figure 4.5(a). When the windscreen is present, the wind noise is reduced because the windscreen suppresses the turbulence inside the porous material. For the viscous coefficient below 10^8 m^{-2}, the larger the viscous resistance, the greater the wind noise reduction, as shown in Figure 4.5(b) and (c). However, for a viscous coefficient larger than 10^8 m^{-2}, the windscreen tends to be a solid cylinder and a strong wake is generated behind the windscreen, which deteriorates the wind noise reduction performance, as shown in Figure 4.5(d).

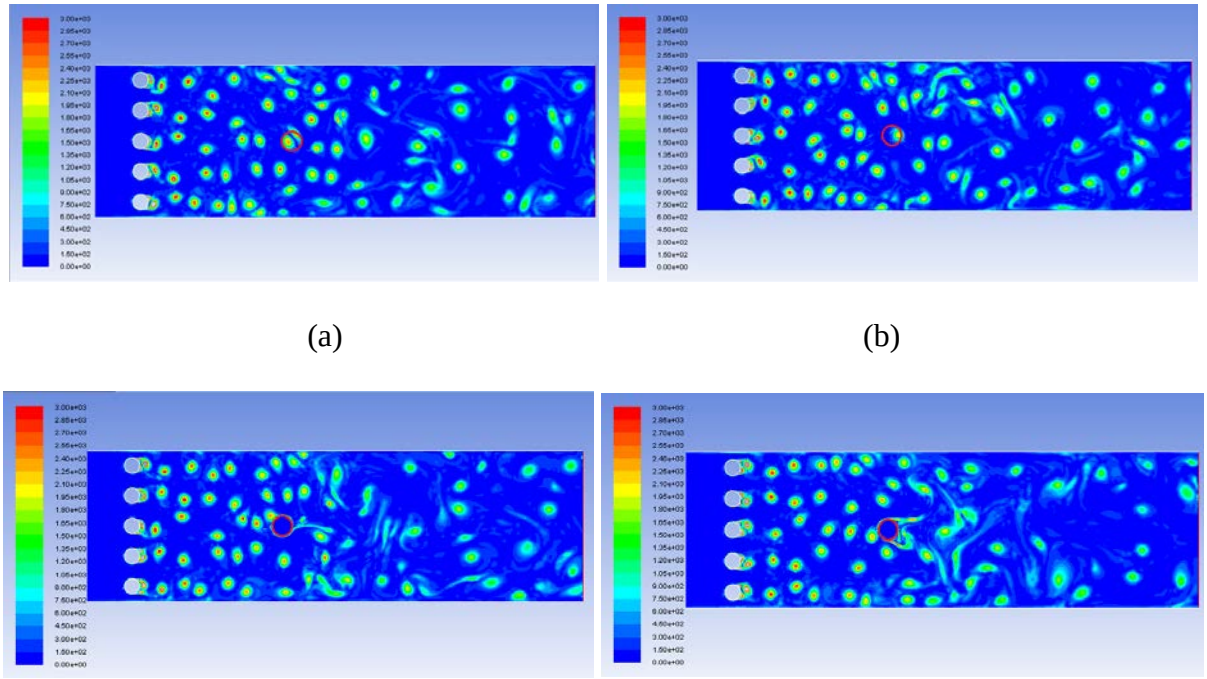

(a) (b)

(c) (d)

Figure 4.5 The vorticity contour for different viscous coefficients, (a) $1/K = 0$ (no windscreen), (b) $1/K = 10^6$ m^{-2}, (c) $1/K = 10^8$ m^{-2}, and (d) $1/K = 10^{10}$ m^{-2}. The red marker circle in the middle denotes the location of the microphone windscreen.

B. The inertial effect

In the second set of simulations, a zero viscous coefficient was assumed so that no viscous force was applied on the air flow from the porous windscreen. In this case, the physical wind noise reduction mechanism of the windscreens results from the inertial forces on the air flow by the solid frame of the porous windscreen.

The simulated wind velocity spectra and wind noise spectra are shown in Figure 4.6 for various inertial coefficients, which demonstrate that the wind velocity inside the porous windscreen decreases with growing inertial coefficients while the wind noise level first decreases then increases with inertial coefficients. Similar to the viscous effect, the WNR reaches its maximum near the inertial coefficient of 50 m^{-1} and decreases slightly afterward.

This is illustrated in Figure 4.7 with the overall WNR in the frequency band from 1 Hz to 1000 Hz. This phenomenon can again be explained by the trade-off between the turbulence suppression inside and the wake generation behind the windscreens, as shown in Figure 4.8. When the inertial coefficient is smaller than 50 m^{-1}, the turbulence inside the windscreen is suppressed while there is no wake generated behind due to the permeability of the windscreen. When the inertial coefficient is larger than 50 m^{-1}, the windscreen is less permeable and wake is formulated. The inertial coefficient is a characterization of the inertial force on the air flow to change the flow direction, which is dependent on the tortuosity of the porous medium.

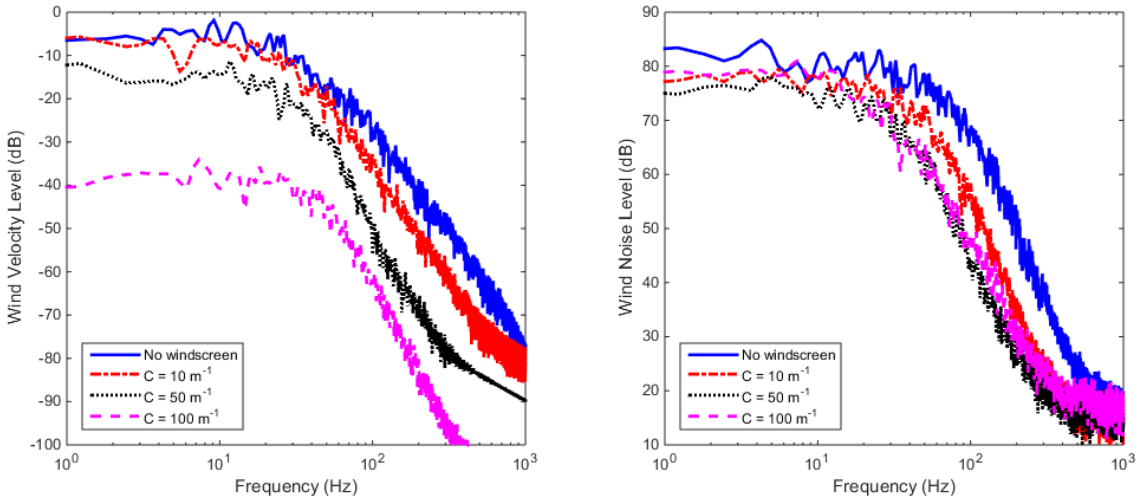

(a) (b)

Figure 4.6 (a) The wind velocity spectra and (b) the wind noise spectra for different inertial coefficients at the wind speed U = 4 m/s.

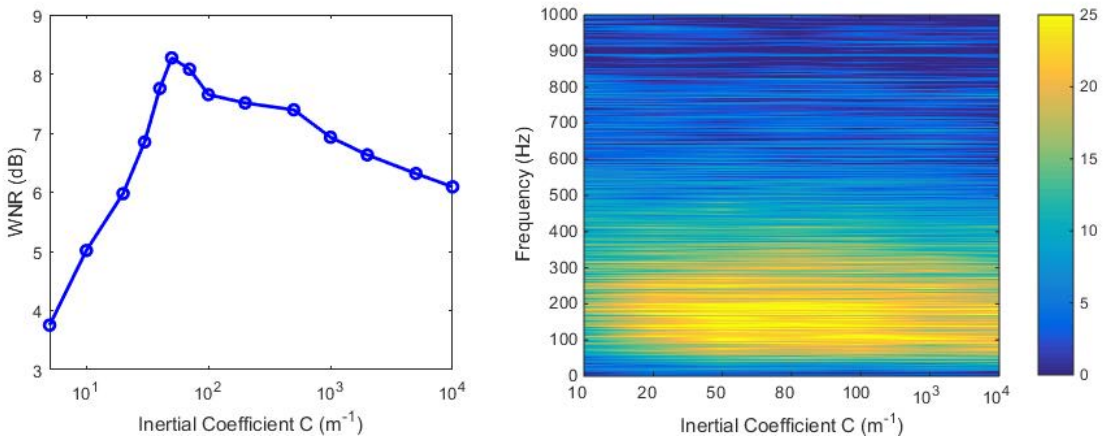

(a) (b)

Figure 4.7 (a) The overall Wind Noise Reduction (WNR) and (b) the WNR at different frequencies for 90 mm windscreens with different inertial coefficients at the wind speed U = 4 m/s.

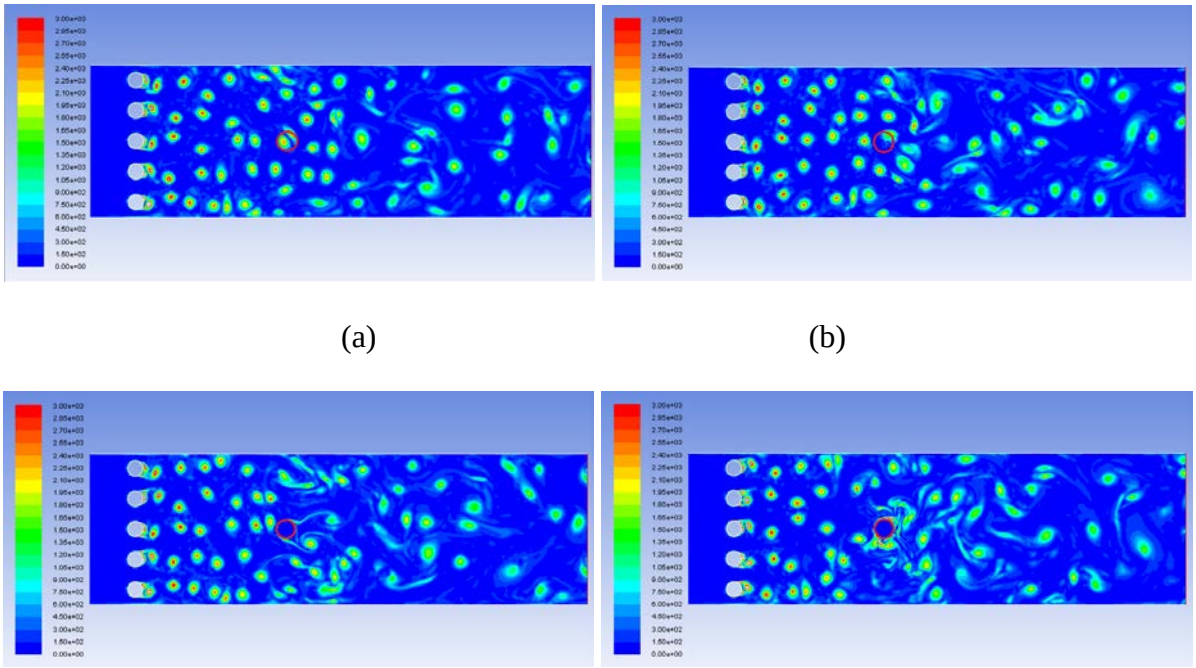

(a) (b)

(c) (d)

Figure 4.8 The vorticity contour for different inertial coefficients, (a) C = 0 (no windscreen), (b) C = 10 m^{-1}, (c) C = 50 m^{-1}, and (d) C = 100 $m^{-1}m^{-2}$. The red marker circle at the middle denotes the location of the microphone windscreen.

By comparing the wind velocity spectra and wind noise spectra in Figure 4.3 and Figure 4.6, it can be observed that the wind velocity level decreases continuously with the viscous or inertial coefficients in the broad band from 1 Hz to 1000 Hz, whereas the wind noise is only reduced in the frequency band below 500 Hz and has the lowest level at a certain value of viscous or inertial coefficients. The inconsistency between the wind velocity and wind noise inside the windscreens shows that the wind noise level is not proportional to the wind velocity inside the porous windscreens, as stated in the intuitive explanation [51].

C. The combination effect

The above simulation results show separately the individual effect of the viscous force or inertial force on the wind noise reduction performance by the porous windscreens. To understand the wind noise reduction performance of real windscreens with both viscous and inertial forces on the air flow, various combinations of the viscous and inertial coefficients are investigated. The simulation results are shown in Figure 4.9, where the horizontal and vertical axes are the viscous and inertial coefficients, respectively, and different colours are used to represent different levels of WNR.

It can be observed that the viscous forces are the main source of wind noise reduction mechanism for the porous windscreens when the inertial coefficient is below 50 m^{-1}, while for the inertial coefficient larger than 100 m^{-1}, the viscous forces have little effect. Figure 4.9 indicates that the wind noise reduction performance of the windscreen is not the supposition of the viscous and inertial effect; in contrast, it is dominated by the larger effect. The WNR is the largest when the viscous and inertial coefficients are approximately 10^8 m^{-2} and 50 m^{-1}, respectively, which is denoted by a red cross in Figure 4.9. The porous windscreens with larger or smaller viscous and inertial coefficients have inferior performance.

In summary, the above simulation results show that the choice of the porous material for microphone windscreens should take into account both the turbulence suppression inside and the wake generation behind the windscreen, and there exists optimal viscous and inertial coefficients to reach the maximum performance. It is noteworthy that the optimal viscous and inertial coefficients should depend on the diameter of the porous windscreens and the wind speed of the incoming flow, and the values presented in Figure 4.9 are only applicable for a 90 mm spherical porous windscreen at the wind speed U = 4 m/s.

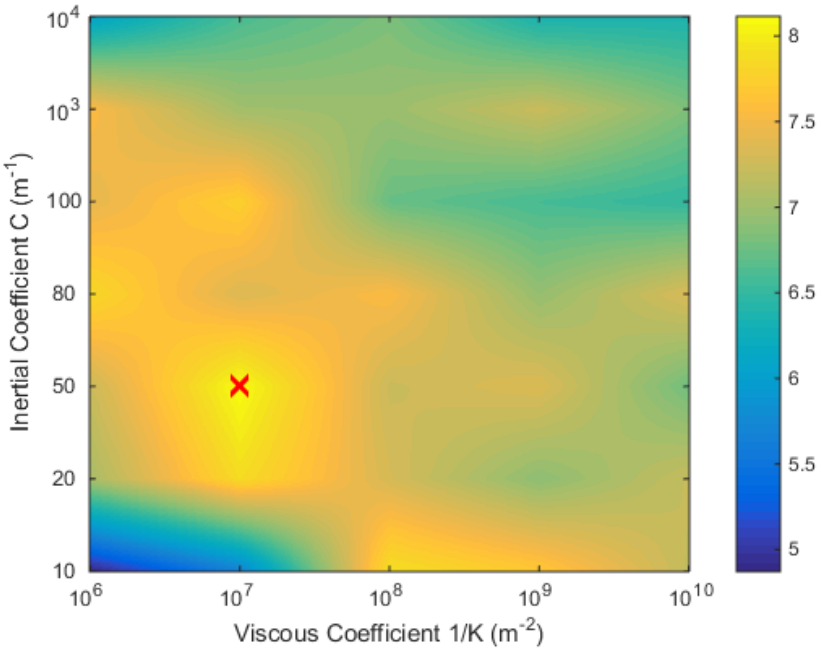

Figure 4.9 The overall Wind Noise Reduction (WNR) for various viscous and inertial coefficients for a 90 mm spherical porous windscreen at the wind speed U = 4 m/s.

4.2.3 Experimental results

To verify the reliability of the simulations, experiments were performed with a fan in the SIAL sound pod at RMIT University, as shown in Figure 4.10. The SIAL sound pod is a small room where the walls and floor are treated with sound absorptive material. The fan and

the microphone were approximately 0.8 m above the floor, with a separation distance of 0.5 m. The wind noise was measured with a B&K Type 4189 prepolarized free field 1/2" microphone and a G.R.A.S Type 40BF 1/4" free field microphone, respectively. The 1/2" microphone was connected to the B&K Type 2270 Analyzer via a B&K Type ZC 0032 Preamplifier. The system was calibrated with a B&K Type 4231 calibrator. The wind noise reduction by 5 spherical porous microphone windscreens with a diameter of 90 mm were measured in the experiments. The porosity of the porous microphone windscreens varied from 20 PPI (Pores Per Inch) to 60 PPI with a step of 10 PPI, as shown in Figure 4.10(c).

In the experiments, the fan ran at its highest speed and the mean wind speed around the microphone was about 4.2 m/s. The Reynolds number of the flow in the fan tests can be estimated as $Re = UD/\nu = 2.8\times10^4$ (where U = 4.2 m/s is the mean wind speed, D = 0.1 m is the fan blade length and $\nu = 1.511\times10^{-5}$ is the air kinematic viscosity at the temperature of 20 ^{o}C). The Reynolds number based on the Taylor microscale is proportional to the square root of the Reynolds number, i.e., $Re_\lambda \approx (20Re/3)^{1/2} = 432$ [24]. In contrast, the Reynolds number based on the Taylor microscale in outdoor atmospheric turbulence Re_λ varies from 4250 to 19500, which is much larger than that in the fan test [118]. The length scale of the atmospheric turbulence is much larger than that in the fan test, which might have a significant effect on the wind noise reduction performance of the porous microphone windscreens. This effect is not considered here and will be studied in the future work.

The wind noise was first measured by using the bare microphone inside the air flow and the background noise was measured by placing the microphone out of the flow but at the same distance from the fan. The wind noise and the background noise spectra of the environment with the fan running are compared in Figure 4.11(a), which shows that the wind noise level is much higher than the background noise; hence the measurement results with the microphone placed inside the air flow were primarily due to the wind turbulence from the

fan. The peak at 62.5 Hz and its harmonics in the background noise are the mechanical noise due to the fan blade.

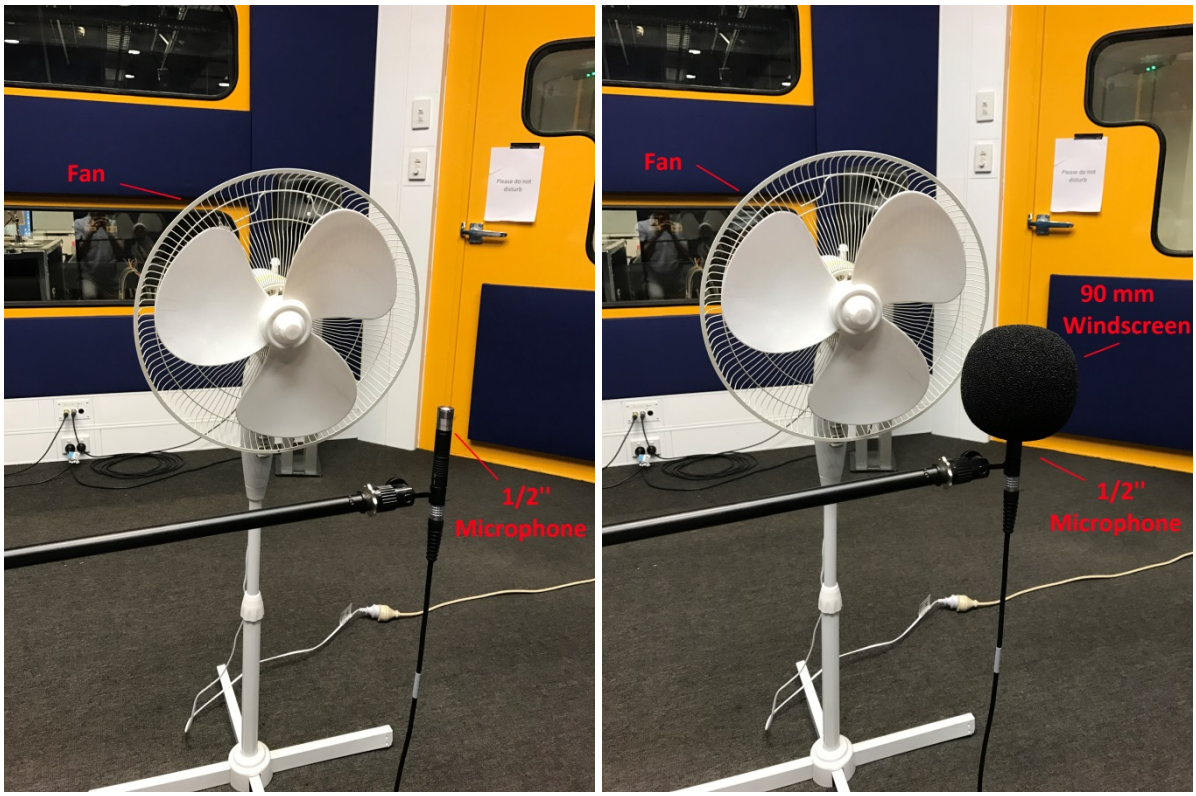

(a) (b)

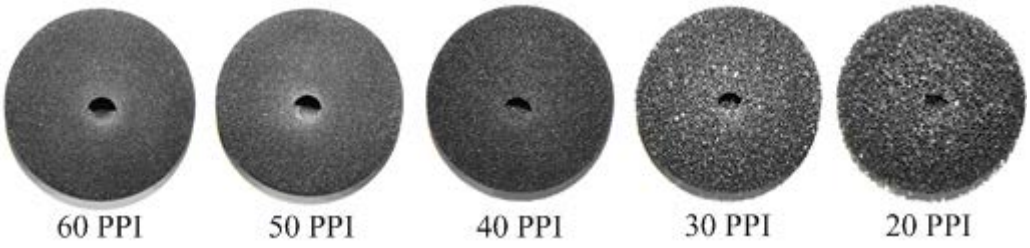

(c)

Figure 4.10 The experimental setup (a) without and (b) with a 90 mm diameter porous windscreen installed on a 1/2" microphone, and (c) the 90 mm spherical porous microphone windscreens of different porosities from 20 PPI to 60 PPI.

The wind noise inside the porous microphone windscreens was measured in the same way as that for the bare microphone and the measured wind noise spectra are also shown in Figure 4.11(a). The wind noise spectra measured inside 30 PPI and 50 PPI windscreens are not shown for the sake of brevity. It is clear in Figure 4.11(a) that the wind noise level inside the porous windscreens is still above the background noise, thus the measurement results are valid.

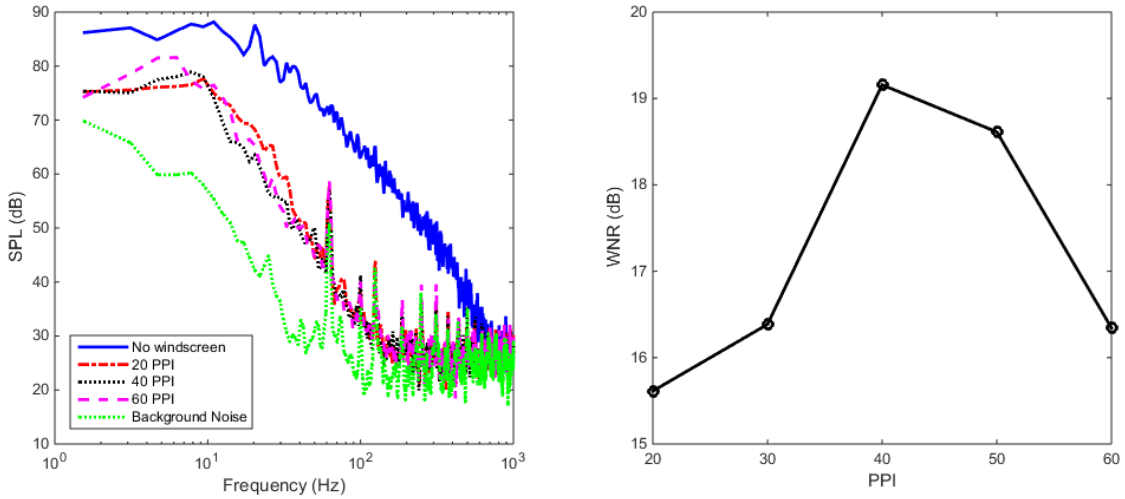

(a) (b)

Figure 4.11 The measurement results of (a) the wind noise spectra and (b) the overall Wind Noise Reduction (WNR) as a function of porosity.

The wind noise spectra measured inside windscreens of varying porosity are almost indistinguishable above 50 Hz due to the harmonic mechanical noise from the fan blade. However, it can be seen from the spectra below 50 Hz in Figure 4.11(a) that the wind noise inside the 40 PPI windscreen is lower than that inside both the 20 PPI and 60 PPI windscreens, which demonstrates that the existence of an optimal porosity for the porous windscreen to achieve the best performance. This can be more clearly observed from Figure 4.11(b), which shows the overall WNR in the broad frequency band from 1 Hz to 1000 Hz as

a function of the PPI values. The overall WNR first increases with the porosity but then decreases after reaching the maximum performance at 40 PPI.

As shown in Figure 4.10(c), with the increase of the PPI value from 20 to 60, the number of pores is increased while the pore size is reduced, so the contact surface area between the air flow and the porous frame is increased which leads to the increase of the viscous forces on the air flow [124]. Since the viscous coefficient $1/K$ is a lumped measure of the total viscous forces, it increases correspondingly with the increased PPI value [124]. Similarly, the inertial coefficient C also increases with the PPI value because the inertial forces from the porous frame on the air flow increases [124]. Both the viscous and inertial coefficients can be measured with hydraulic equipment [127]. However, the viscous and inertial coefficients of the porous windscreens used here were not measured because no such hydraulic equipment is available to us at present.

In summary, both the viscous and inertial coefficients of the porous windscreens increase with the PPI value although the specific values for the porous microphone windscreens used in our experiments are not known. Therefore the measurement results in Figure 4.11 verified the simulation results that there exists an optimal value of viscous and inertial coefficients for porous microphone windscreens to reach the best performance, and the design of porous microphone windscreens should take into account both turbulence suppression inside and the wake generation behind the microphone windscreens.

The simulations and experimental results in this paper indicate that the wind noise reduction performance can be further improved if the turbulence inside the windscreens can be suppressed and in the meantime no wake is generated behind the windscreen, which might be achieved with porous microphone windscreens with variable porosity. On the other hand, metamaterials can be explored to manipulate the fluid flow around three-dimensional bodies, e.g., Urzhumov and Smith [128,129] investigated fluid flow cloak which preserves the flow

that would have existed in the absence of the object so that the downstream wake is eliminated. However, their study is based on numerical simulations for the non-turbulent flows. Much more work is needed for developing prototype metamaterial microphone windscreen in the future.

4.2.4 Conclusions

This section investigates the wind noise reduction mechanism of porous microphone windscreens. The pressure fluctuations inside porous windscreens with various viscous and inertial coefficients are investigated with numerical simulations. The viscous and inertial coefficients represent the viscous forces resulting from the fluid-solid interaction along the surface of the pores and the inertial forces imposed on the fluid flow by the solid structure of the porous medium, respectively. Simulation results indicate that the wind noise reduction first increases and then decreases with both viscous and inertial coefficients after reaching a maximum. Experimental results conducted on 5 porous microphone windscreens with porosity from 20 PPI (Pores Per Inch) to 60 PPI show that the 40 PPI windscreen has the highest wind noise reduction performance, and this supports the simulation results. The existence of the optimal values for the viscous and inertial coefficients is explained qualitatively and it is shown that the design of porous microphone windscreens should take into account both turbulence suppression inside and wake generation behind the windscreen to achieve the optimal performance.

4.3 Spatial decorrelation of wind noise by porous microphone windscreens

Most of the studies in the literature focused on the wind noise inside windscreens measured with a single microphone, without considering the spatial structure of wind noise. This section investigates the wind noise reduction mechanism of porous microphone

windscreens by examining the effect of porous windscreens on the spatial structure of wind noise (signal). The spatial structure of wind noise is studied by using the magnitude squared coherence of the pressure measured with two microphones at various separation distances first, and then the wind noise reduction by porous microphone windscreens is investigated. Finally, the spatial coherence between the wind noise outside and inside the porous windscreens are calculated to investigate the wind noise reduction mechanism.

4.3.1 Simulation model

Figure 4.12 shows the diagram of the two dimensional model used in the simulations, where a uniform air flow with a mean speed U enters the computation domain from the left boundary. The computation domain is 34D in the downwind direction and 10D in the crosswind direction. Five solid cylinders are placed upstream to generate turbulence. The diameter and the interval between cylinders are both D and the solid cylinder array is 4D from the flow inlet boundary. Two 1/2" microphones are modeled as the rigid cylinders in Figure 4.12 and the pressure averaged over the rigid cylinder is monitored to mimic the pressure fluctuations detected by the microphone.

(a)

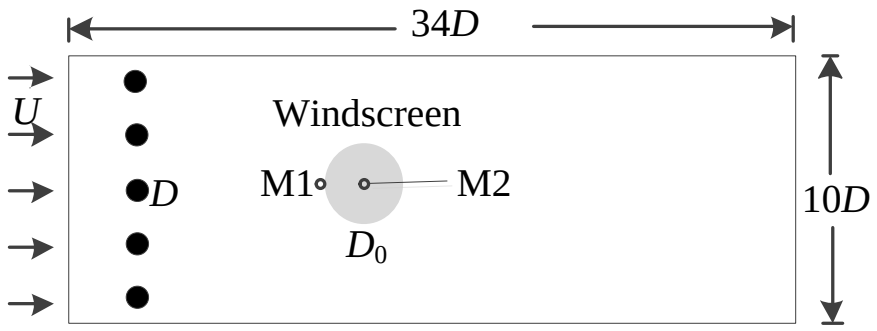

(b)

Figure 4.12 The diagram of the two dimensional simulation model (a) without and (b) with a microphone windscreen, where the 1/2" microphones are modeled as rigid cylinders.

Two sets of simulations were performed. In the first set of simulations in Figure 4.12(a), there was no microphone windscreen and the pressure fluctuations at two microphone locations M1 and M2 are monitored at various separation distances to study the spatial structure of wind noise. The fluid flow is described by the Navier-Stokes equations for viscous incompressible flow in Eqs. (4.1) and (4.2). In the second set of simulations in Figure 4.12(b), a microphone windscreen of diameter D_0 (gray circle in Figure 4.12) was placed $10D$ from the upstream solid cylinder array. The pressure fluctuations outside (at position M1) and inside (at position M2) the microphone windscreen were recorded and compared with that without the windscreen to investigate the effect of the microphone windscreen on the spatial structure of wind noise. The microphone windscreen was modeled as a porous medium,

inside which the fluid flow is governed by the continuity equation and the momentum conservation equation proposed in Eqs. (4.3) and (4.4). The pressure is calculated from the velocity field based on the Poisson equation in Eq. (2.1).

Equations (4.1) to (4.4) were solved in FLUENT 16.0 with the boundary conditions of velocity and stress continuity at the windscreen surface. The volume-averaged velocity inside the porous medium is used in the continuity of velocity in the boundary conditions. The models were built, and meshed in ANSYS Workbench 16.0, and simulated in ANSYS FLUENT 16.0. In the simulations, the boundary condition of the flow inlet was set to "velocity inlet", the output boundary condition was set to "pressure outlet", the upper and lower boundaries were set as "wall", and the microphone windscreen is modeled as "porous media zone". The computational domain was carefully meshed by dividing the domain into several subdomains, within which the structure mesh was deployed and checked. The mesh was changed from coarser to finer until the simulation results converge and are independent of mesh.

In the simulations, the diameter of the upstream cylinders was D = 50 mm. The permeability and inertial coefficients were set as $K = 10^{-7}$ m^2 and C = 50 m^{-1}, respectively. For each simulation, the time history of velocity and pressure fluctuations at the monitoring location was recorded for 5 s with a sampling rate of 10 kHz. It is noteworthy that the numerical simulations here are two dimensional only and the pressure spectrum can be different to that for the three dimensional turbulence. Therefore, the simulation results are used to gain insights into the mechanism and performance of the porous microphone windscreens, and they are not intended to be compared with the experimental results quantitatively.

To investigate the spatial structure of the wind noise, the magnitude squared coherence between the pressure fluctuations recorded at M1 and M2 was calculated [130],

$$MSC(f) = \frac{|\varphi_{12}(f)|^2}{\varphi_{11}(f)\varphi_{22}(f)} \tag{4.9}$$

where $\varphi_{12}(f)$ is the cross spectral density, $\varphi_{11}(f)$ and $\varphi_{22}(f)$ are the auto spectral density at frequency f.

4.3.2 Simulation results

A. Spatial structure of wind noise

In the first set of simulations in Figure 4.12(a) without microphone windscreen, the microphone location M1 is fixed and M2 is moved to change the separation distance along the wind direction d from 30 mm to 90 mm with a step of 15 mm. Both the velocity and pressure fluctuations at the microphone locations are monitored and the power spectral density of velocity and pressure are calculated based on the Welch method. The obtained velocity spectra at location M1 are shown in Figure 4.13(a) at various wind speeds from 2 m/s to 14 m/s, and the magnitude squared coherence between the velocity fluctuations at M1 and M2 are calculated and illustrated in Figure 4.13(b) as a function of the separation distance to the turbulence wavelength ratio (d/ξ), where the separation distance d is fixed at 30 mm. The turbulence wavelength is a parameter that is used to characterize the length scale of the turbulent eddies, and it can be calculated with $\xi = U/f$ where U is the mean wind speed and f is frequency. A larger turbulence wavelength corresponds to turbulent eddies of a larger size. It is also inversely proportional to frequency, and a large turbulence wavelength corresponds to low frequency.

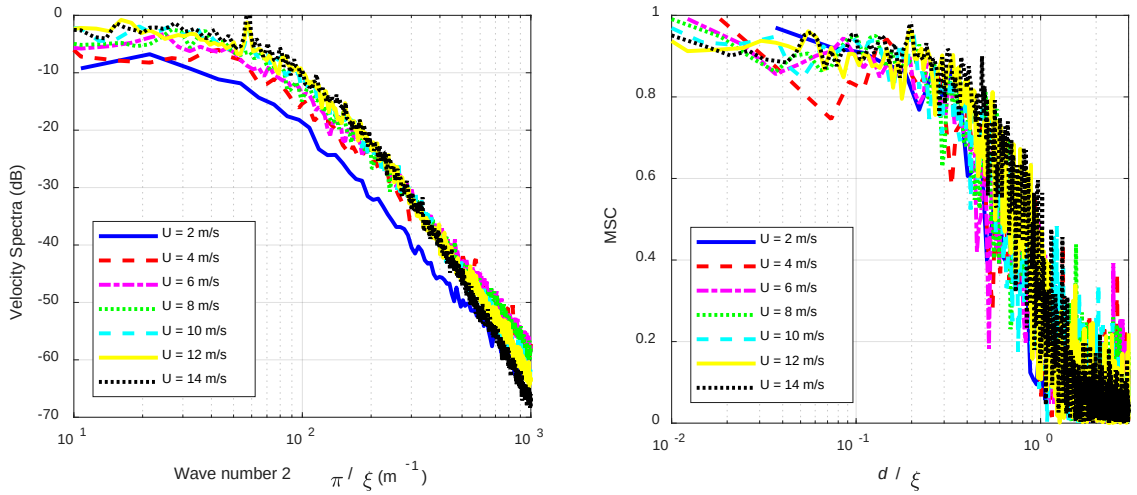

(a) (b)

Figure 4.13 (a) The velocity spectra as a function of turbulence wave number and (b) the magnitude squared coherence of the velocity fluctuations as a function of the ratio of the separation distance (fixed to 30 mm) to turbulence wavelength (the turbulence wavelength ξ is the variable for the horizontal axis) for wind noise at different wind speeds.

It can be observed from Figure 4.13 that the velocity spectra are nearly constant at the lower frequency range while decay rapidly in the higher frequency range, and the velocity fluctuations are coherent when the separation distance is smaller than the turbulence wavelength (i.e., $d/\xi < 1$). Similarly, Figure 4.14 presents the pressure spectra and the magnitude squared coherence of the pressure fluctuations. Figure 4.14(a) shows that the wind noise is almost flat in the low frequency range while decaying rapidly in the higher frequency range when the wave number is above 100 m^{-1}. In addition, the wind noise increases with the mean wind speed but the rate of noise level change decreases with growing velocity. These two observations are consistent with the wind noise spectra measured in a small anechoic wind tunnel by Alamshah et al. [49].

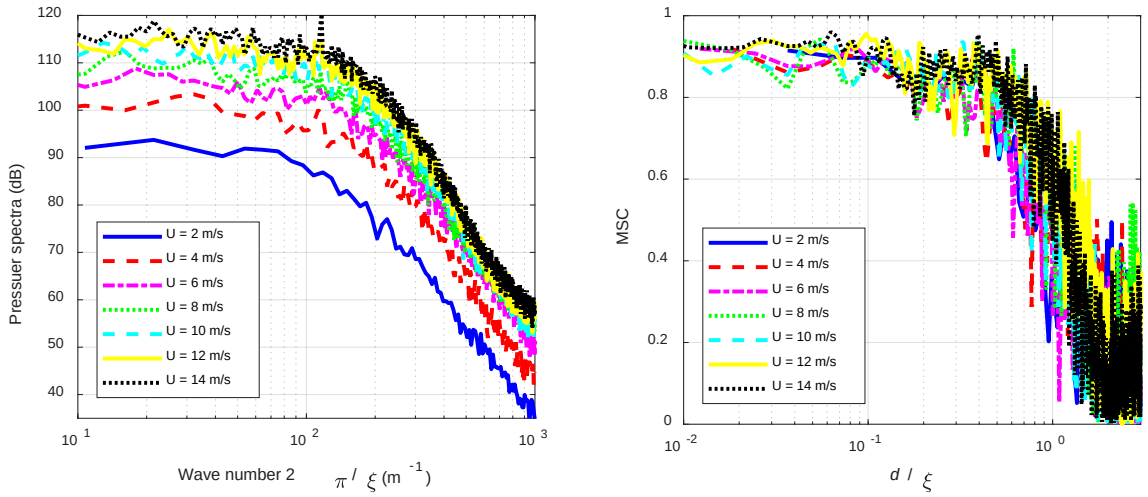

(a) (b)

Figure 4.14 (a) The pressure spectra as a function of turbulence wave number and (b) the magnitude squared coherence of the pressure fluctuations as a function of the ratio of the separation distance (fixed to 30 mm) to turbulence wavelength (the turbulence wavelength ξ is the variable for the horizontal axis) for the wind noise at different wind speeds

Figure 4.14 (b) shows that when the separation distance is smaller than the turbulence wavelength (i.e., $d/\xi < 1$), the wind noise at location M1 and M2 are coherent, whereas when the separation distance is larger than the turbulence wavelength (i.e. $d/\xi > 1$), the wind noise becomes incoherent. This is reasonable because when the turbulent eddy size is smaller than the separation distance, the instantaneous pressure recorded at location M1 and M2 originate from different eddies, hence the pressure signals are incoherent. In contrast, when the turbulent eddy size is larger than the separation distance, the instantaneous pressure at location M1 and M2 are caused by the same eddy, therefore the pressure signals are coherent. It can also be observed from Figure 4.14(b) that the magnitude squared coherence at different wind speeds are similar when the turbulence wavelength is larger than the separation distance (i.e., $d/\xi < 1$).

The magnitude squared coherence of the pressure fluctuations as a function of the separation distance to wavelength ratio for various separation distances are compared in Figure 4.15 for wind speeds U = 4 m/s and U = 10 m/s, where the variable along the horizontal axis is the turbulence wavelength ξ. Figure 4.15 shows that the pressures at M1 and M2 are incoherent when the separation distance is larger than the turbulence wavelength (i.e., $d/\lambda > 1$) regardless of the separation distance between microphones. When the turbulence wavelength is larger than the separation distance, the pressures at M1 and M2 are coherent; however, the coherence decreases with increasing separation distance, which indicates that large eddies decay with spatial distance as they are advected downstream by the mean flow. The decrease of spatial correlation with increasing separation distance is consistent with the outdoor measurements of wind noise correlation in microphone arrays in Ref. [86].

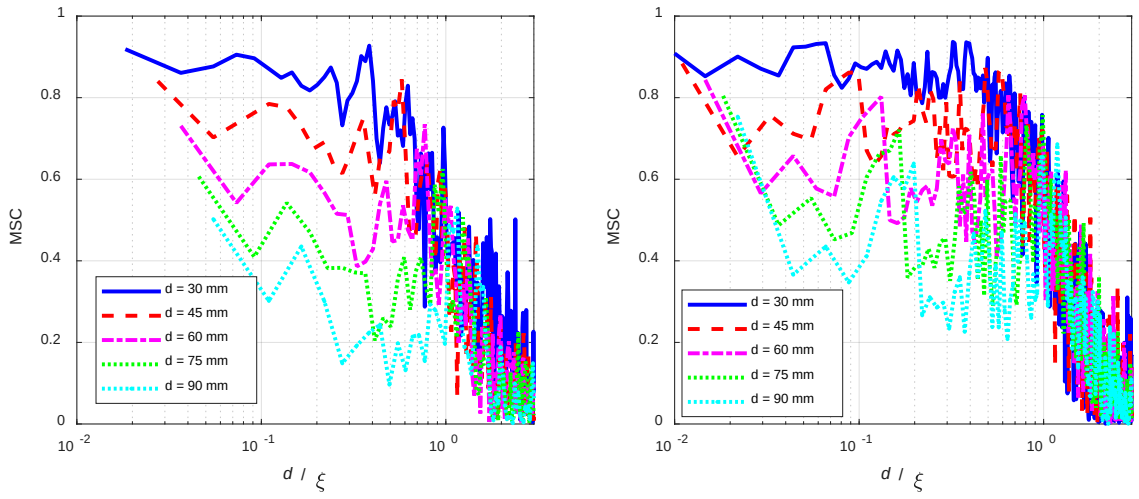

(a) (b)

Figure 4.15 The magnitude squared coherence of the pressure fluctuations as a function of the separation distance to turbulence wavelength (the turbulence wavelength ξ is the variable for the horizontal axis) ratio at various separation distances for the wind noise at wind speed (a) U = 4 m/s and (b) U = 10 m/s.

B. Wind noise reduction by porous microphone windscreens

To investigate the wind noise reduction performance of the porous microphone windscreens, the pressure inside the porous windscreens with varying diameters (M2 in Figure 4.12(b)) is simulated and compared with that when the windscreen is absent (M2 in Figure 4.12(a)). The wind noise reduction as a function of the windscreen diameter to turbulence wavelength ratio (D_0/ξ) is shown in Figure 4.16(a) for various wind speeds, where the wind noise reduction tends to form a single curve.

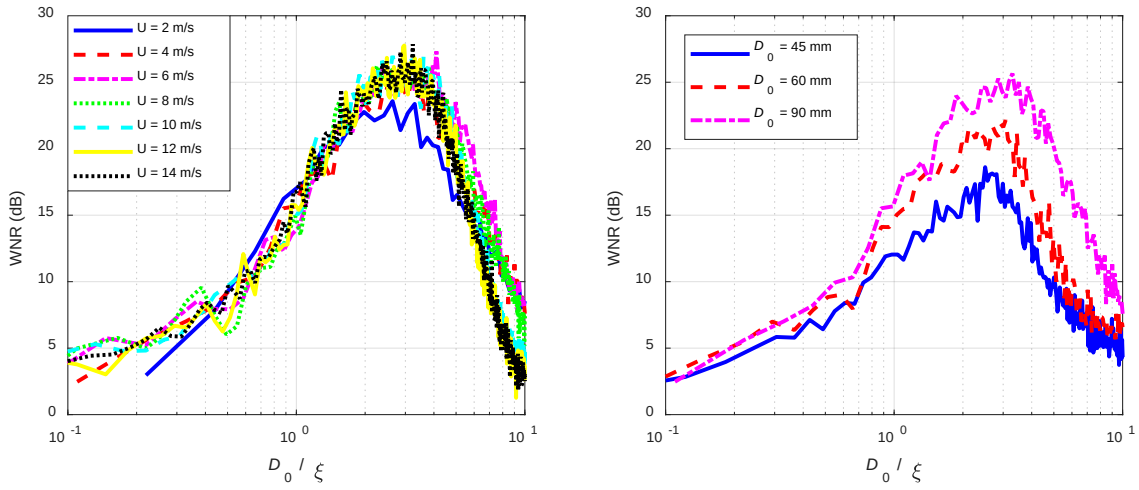

(a) (b)

Figure 4.16 The wind noise reduction as a function of the windscreen diameter to turbulence wavelength ratio (the turbulence wavelength ξ is the variable for the horizontal axis) for (a) a 90 mm diameter windscreen at various wind speeds and (b) windscreens of varying diameters at the wind speed U = 4 m/s.

It can be observed that the wind noise reduction performance of the porous windscreen becomes most effective in a certain frequency range, where the windscreen diameter is

approximately 2 to 4 times of the turbulence wavelengths ($2 < D_0/\xi < 4$), regardless of the wind speed. Figure 4.16(b) presents the wind noise reduction for different windscreen diameters at the wind speed U = 4 m/s, which also shows that the porous windscreen attenuates the wind noise more effectively when the windscreen diameter is approximately 2 to 4 times of the turbulence wavelengths ($2 < D_0/\xi < 4$), regardless of the windscreen diameters. Figure 4.16(b) also shows that the larger windscreen is more effective in reducing the wind noise, which is consistent with the measurement results in the reference [47], where the 20 cm diameter windscreen attenuates more wind noise than the 7 cm diameter windscreen.

The simulation results in Figure 4.16 indicate that when the turbulence wavelength is much larger than the windscreen diameter ($D_0/\xi < 0.1$), the porous windscreen has almost no effect on the wind noise reduction. With the turbulence wavelength increasing, the wind noise reduction first increases and then decreases after reaching the maximum. When the turbulence wavelength is much smaller than the windscreen diameter ($D_0/\xi > 10$), the wind noise reduction approaches zero again. The above results imply that a large windscreen is needed to reduce the low frequency wind noise that corresponds to a large turbulence wave length for a certain wind speed.

To understand the mechanism of the wind noise reduction by the porous microphone windscreen and the existence of this effective frequency range, the magnitude squared coherence of the pressure outside and inside the 90 mm diameter porous microphone windscreen (M1 and M2 in Figure 4.12(b)) is calculated and compared with that when the windscreen is absent (M1 and M2 in Figure 4.12(a)). The pressure spectra and magnitude squared coherence in Figure 4.17 show that the pressure spectra is reduced significantly in the frequency range from 200 Hz to 600 Hz. This can be more clearly observed in Figure 4.17(c) and (d), where the wind noise reduction and magnitude squared coherence difference

as a function of the windscreen diameter to turbulence wavelength ratio (D_0/ξ) are shown, respectively. Figure 4.17(d) shows that compared to the magnitude squared coherence without the porous windscreen, the magnitude squared coherence with the windscreen is reduced significantly when the windscreen diameter is approximately 2 to 4 times the turbulence wavelength ($2 < D_0/\xi < 4$), which corresponds to the most effective wind noise reduction frequency range in Figure 4.17(c). It is noteworthy that the frequency range of the MSC reduction in Figure 4.17(d) is narrower than the wind noise reduction in Figure 4.17(c). The exact reason is unclear yet and will be investigated in the future with a detailed modeling of the pore structure of the porous microphone windscreens.

This observation indicates that the mechanism of the wind noise reduction by porous microphone windscreens is related to the spatial decorrelation provided by the porous material and/or structure. When the turbulence wavelength is much larger than the windscreen, the wind noise is coherent regardless of whether the windscreen is present or not, there is barely any reduction in wind noise. When the diameter of the windscreen is between 2 to 4 times the turbulence wavelength ($2 < D_0/\xi < 4$), the spatial structure of wind noise is decorrelated by the windscreen, and the windscreen is most effective in wind noise reduction in this frequency range. When the turbulence wavelength is much smaller than the windscreen, the wind noise itself is incoherent and the windscreen is ineffective.

The simulation results show that the wind noise level increases with the wind speed, and the wind noise is spatially coherent at a low frequency range where the turbulence wavelength is larger than the separation distance, but the coherence decreases with the separation distance. The porous microphone windscreens are more effective in reducing wind noise in the frequency range where the windscreen diameter is approximately 2 to 4 times the turbulence wavelength.

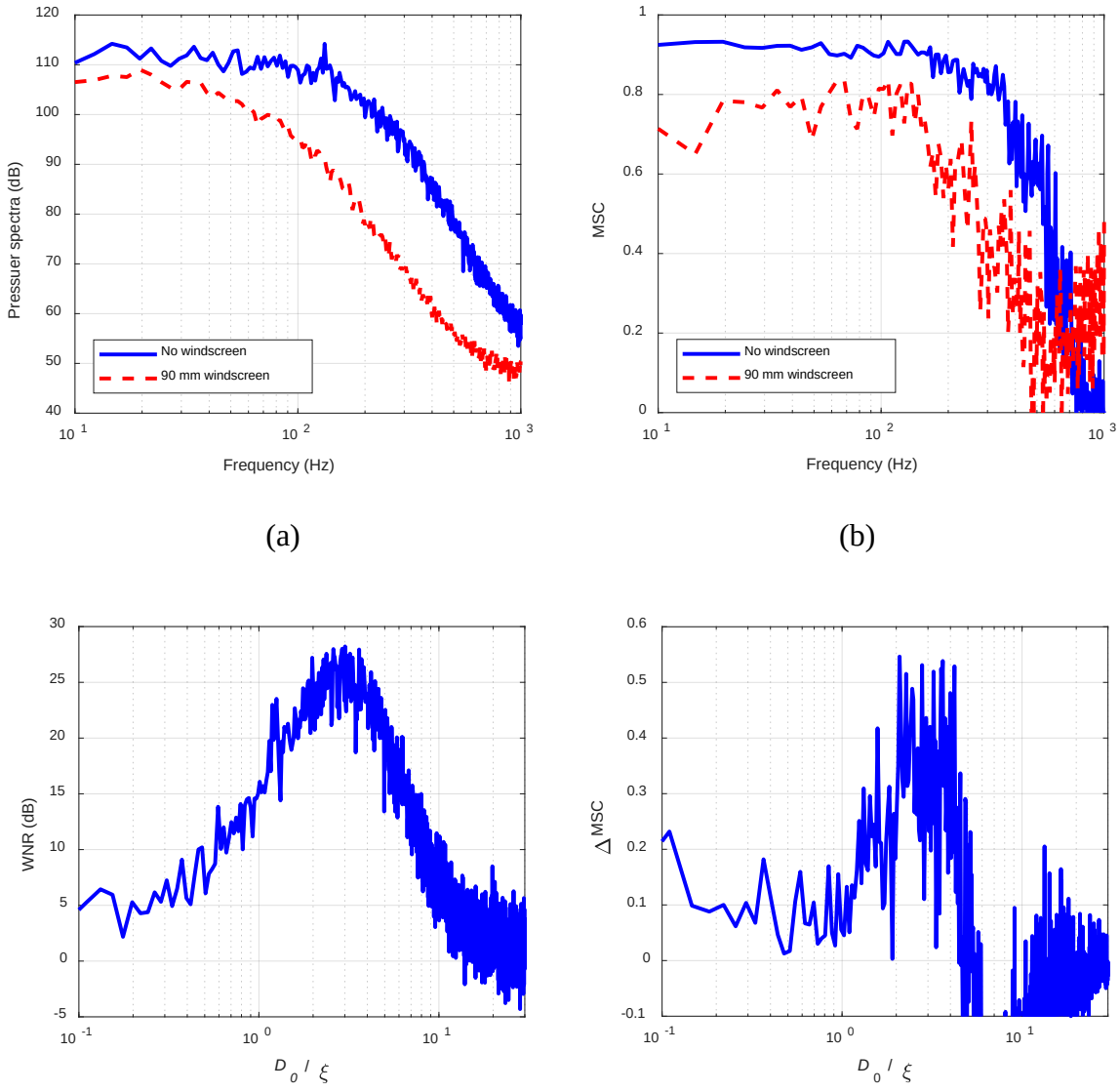

Figure 4.17 (a) The pressure spectra and (b) the magnitude squared coherence of the pressure fluctuations as a function of frequency, (c) the wind noise reduction, and (d) the magnitude squared coherence difference (ΔMSC) as a function of the ratio of the windscreen diameter (90 mm) to the turbulence wavelength (the turbulence wavelength ξ is the variable for the horizontal axis) for the wind noise at the wind speed U = 10 m/s.

It is noteworthy that the correlation length is used in some literature to characterize the spatial decorrelation of wind noise by the porous windscreen and the wind fence enclosure

[50,79], where an exponential function is fitted to the measured coherence function at different separation distances and the fitted correlation length is used to calculate the wind noise inside the windscreens. Different from these studies, in this work the coherence between the pressures outside and inside the porous windscreen was measured directly and compared with that when the windscreen is absent. This can help show intuitively that the decorrelation is related to the wind noise reduction and provides an insight to the mechanism of wind noise reduction by porous windscreens.

Although the above results show that the wind noise reduction by the porous microphone windscreen may be related to the decorrelation of the spatial structure of wind noise, there is no evidence demonstrating that the spatial decorrelation causes the wind noise reduction. The spatial decorrelation can be explained qualitatively based on the surface averaging assumption [52]. In the low frequency region where the eddy size is much larger than the windscreen, the windscreen has little effect on the eddy motion and the pressure around the windscreen surface is similar, so the surface averaging has little effect on the pressure fluctuations. In contrast, in the higher frequency region where the eddy size is smaller than the windscreen, the pressure fluctuations around the surface are uncorrelated due to the effect of the windscreen so the surface averaging reduces the spatial correlation with the pressure fluctuations outside the windscreen.

The above discussions are based on the phenomenological understanding that the wind noise reduction by the porous windscreen is due to the pressure averaging along the windscreen surface. It is still not clear how this surface averaging happens and how it is related to the viscous and inertial effects of the porous windscreen. It is suggested that both the spatial decorrelation and wind noise reduction are due to the viscous and inertial forces introduced by the porous microphone windscreen, which are shown as the third and fourth terms on the right side of Eq. (4.4). How the wind noise is reduced by the windscreens, how

the spatial decorrelation happens and what its relationship is to the viscous and inertial forces are still not clear, which need to be investigated in the future.

4.3.3 Experimental results

To verify the reliability of the simulations, experiments were performed with a commercial fan in a quiet small meeting room, as shown in Figure 4.18(a). The fan and the microphone were approximately 0.8 m above the floor, with a separation distance of 0.5 m. The wind noise was measured with two B&K Type 4189 prepolarized free field 1/2" microphones, both equipped with a B&K ZC0032 preamplifier, which were connected to a two channel B&K Type 2270 Hand-held Analyzer. The system was calibrated with a B&K Type 4231 calibrator. The wind noise reduction by spherical porous microphone windscreens of varying diameters was measured in the experiments. The arrangements of the microphones without and with a 90 mm diameter porous microphone windscreen are shown in Figure 4.18(b) and (c), respectively. It is noteworthy that the turbulence scale in the experiment may be different from that in the simulations, both of which are much smaller than the atmospheric turbulence scale. Therefore these experiment results are not compared with the simulation results quantitatively.

In the experiments, the fan ran at its highest speed and the mean wind speed around the microphone was about 3.8 m/s. The wind noise was first measured by a bare microphone at M1 inside the air flow and the background noise was measured by placing the microphone out of the flow but at the same distance from the fan. The wind noise and the background noise spectra of the environment with the fan running are given in Figure 4.19(a), which indicates that the wind noise level is much higher than the background noise, hence the measurement results with the microphone placed inside the air flow were primarily due to the wind from the fan. The peak at 62.5 Hz and its harmonics in the background noise are the mechanical noise due to the fan blades.

(a) (b) (c)

Figure 4.18 (a) The experimental setup and the microphone locations (b) without and (c) with a 90 mm windscreen of porosity 40 PPI.

The spatial structure of the wind noise was first measured without the microphone porous windscreen as shown in Figure 4.18(b). The pressure at the two microphones with different separation distances was measured and the magnitude squared coherence is compared in Figure 4.19(b). It can be seen that when the separation distance is larger than the turbulence wavelength (i.e., $d/\xi > 1$), the wind noise at the two microphones are incoherent, while when the separation distance is smaller than the turbulence wavelength, the wind noise is coherent but the coherence decreases with increasing separation distance due to the decay of the turbulent eddies.

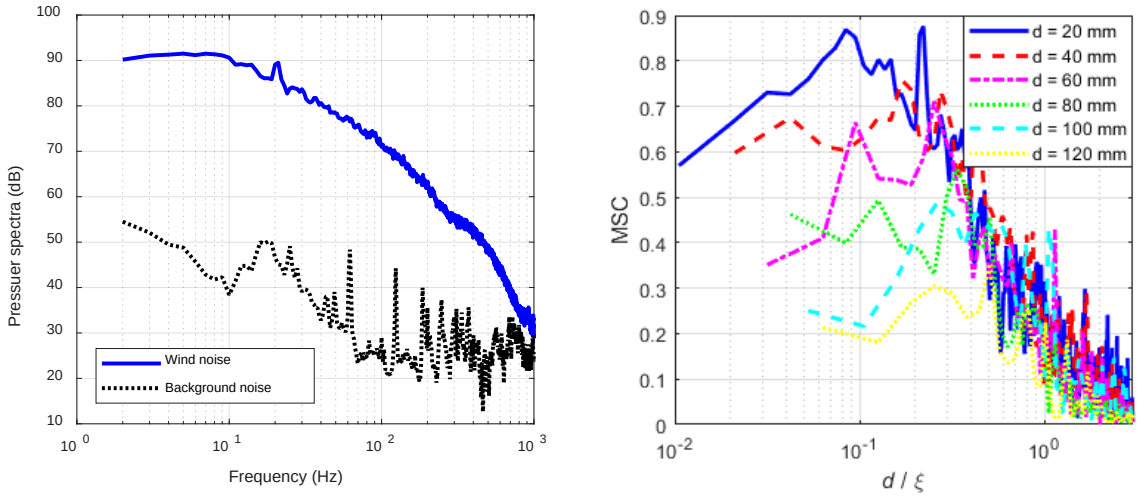

(a) (b)

Figure 4.19 (a) The pressure spectra as a function of frequency and (b) the magnitude squared coherence of the pressure fluctuations as a function of the separation distance to turbulence wavelength ratio (the turbulence wavelength ξ is the variable for the horizontal axis) measured for the wind noise at the wind speed U = 3.8 m/s.

It is noteworthy that the wind noise in the simulations is caused by the turbulent wake generated by the upstream solid cylinders, while the wind noise in the experiments is due to the turbulence produced by the fan blades. Therefore, the experimental results cannot be quantitatively compared with the simulation results. However, the trend consistency between the measurement results in Figure 4.19 and the simulation results in Figure 4.15 provides evidence of the reliability of the simulations.

The wind noise reduction by 4 porous microphone windscreens of varying diameters was measured and compared in Figure 4.20 as a function of the windscreen diameter to turbulence wavelength ratio (D_0/ξ), where the wind speed is U = 3.8. The 45 mm and 90 mm diameter B&K microphone windscreens are UA-1236 and UA-0237, respectively, of which the porosity is unknown. The 60 mm and the other 90 mm diameter windscreens were

customized with 40 PPI (Pores Per Inch) polyurethane foam. It is clear from Figure 4.20 that the porous windscreens are most effective in attenuating wind noise in a certain frequency range, where the windscreen diameter is approximately 2 to 4 times the turbulence wavelength ($2 < D_0/\xi < 4$). These experimental findings are consistent with the simulation results in Figure 4.16 and show that the larger windscreen attenuates more wind noise in the lower frequency region.

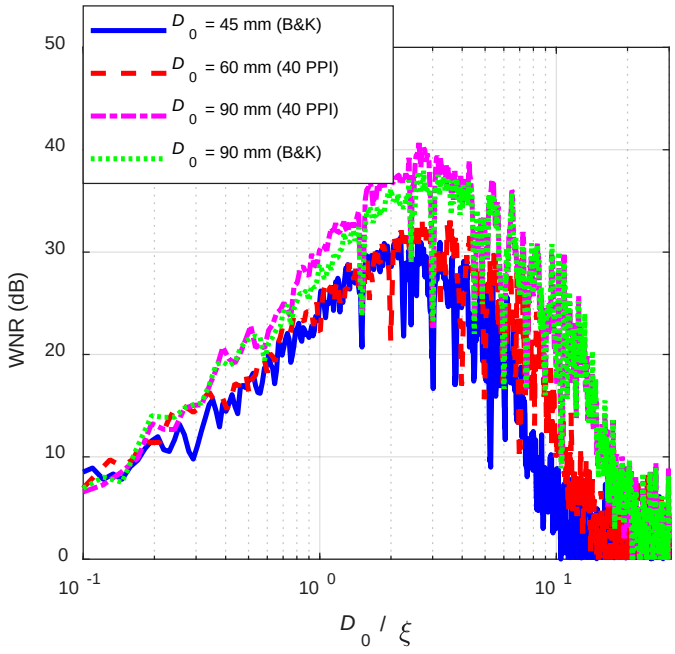

Figure 4.20 The wind noise reduction as a function of the windscreen diameter to turbulence wavelength ratio for windscreens of varying diameters measured for the wind noise at the wind speed U = 3.8 m/s.

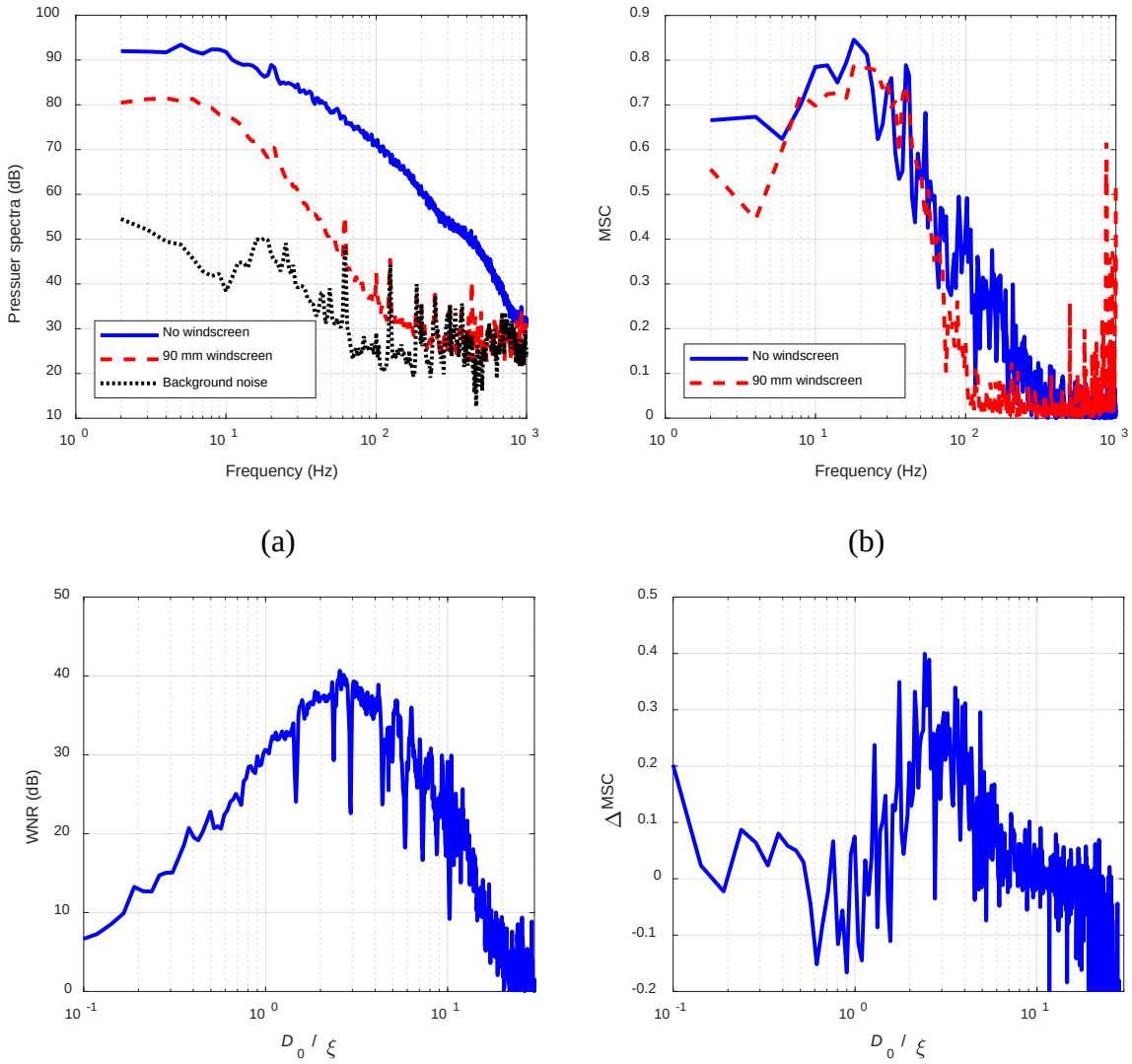

Figure 4.21 (a) The pressure spectra, (b) the magnitude squared coherence of the pressure flucutations as a function of frequency, (c) the wind noise reduction, and (d) the magnitude squared coherence difference (ΔMSC) measured without and with the 90 mm diameter 40 PPI porous microphone windscreens measured for the wind noise at the wind speed U = 3.8 m/s.

The pressure spectra inside the 90 mm diameter porous microphone windscreen (40 PPI) is compared with that without the windscreen and the background noise in Figure 4.21(a), where the wind noise levels are higher than the background noise, so the measured noise is

primarily due to the wind from the fan. The magnitude squared coherence between the pressures measured at the two microphones are shown in Figure 4.21(b), where the magnitude squared coherence reduces significantly above 100 Hz. The wind noise reduction and the magnitude squared coherence difference as a function of the windscreen diameter to turbulence wavelength ratio (D_0/ξ) are shown in Figure 4.21(c) and (d), respectively. It is clear that the magnitude squared coherence with the windscreen is reduced most significantly when the windscreen diameter is approximately 2 to 4 times the turbulence wavelengths ($2 < D_0/\xi < 4$), corresponding to the most effective wind noise reduction frequency range in Figure 4.21(c). This is also consistent with the simulations in Figure 4.17.

4.3.4 Conclusions

In summary, this section investigates the spatial structure of wind noise and the physical mechanism of the wind noise reduction with porous microphone windscreens. Simulation and experimental results show that the wind noise is spatially correlated within a certain distance of the turbulence wavelength. The coherence in the lower frequency range decreases with the separation distance due to the spatial decay of large eddies. The porous microphone windscreens are more effective in reducing the wind noise in a certain frequency range, where the windscreen diameter is approximately 2 to 4 times the turbulence wavelength, and the mechanism of the wind noise reduction is related to the decorrelation effect of the spatial structure of wind noise due to the porous structure of microphone windscreens. Future work will investigate the physical mechanism of the wind noise reduction by the porous microphone windscreens, and the quantitative relationship between the spatial decorrelation of the wind noise structure and the viscous and inertial forces introduced by porous microphone windscreens.

4.4 Wind noise reduction of semi-spherical shell windscreens

In this section, indoor experiments with an axial fan are performed to investigate the wind noise reduction of semi-spherical windscreens made of metal mesh. Five windscreens of different diameters are measured and compared to study the effect of windscreen size on the wind noise reduction performance at different mean wind speeds. Then, the performance of the multi-layer windscreens is investigated. The effect of fabric coverings on the wind noise reduction of the semi-spherical metal mesh windscreens is also studied. Finally, the insertion loss of all the above windscreens is measured.

4.4.1 Experimental setup

The experimental setup is illustrated in Figure 4.22, where a commercial axial fan was used to generate the wind noise on the microphone. The microphone was 1.4 m from the fan and flush mounted on a flat plywood board, with the semi-spherical windscreen placed on the board. The wind noise was measured with a B&K type 4189 prepolarised free field 1/2" microphone equipped with a B&K ZC0032 preamplifier connected to a B&K type 2270 Hand-held Analyser. The system was calibrated with a B&K type 4231 calibrator.

In the experiments, 5 semi-spherical metal mesh windscreens of different diameters were measured, as shown in Figure 4.23(a). The diameter of the windscreens varies from 7 cm to 35 cm and is summarized in Table 4.1. The wind noise reduction of each windscreen is measured first to study the effect of the windscreen size on the performance. The wind noise reduction (WNR) defined in Eq. (4.6) is used to quantitatively examine the noise reduction performance of the windscreens.

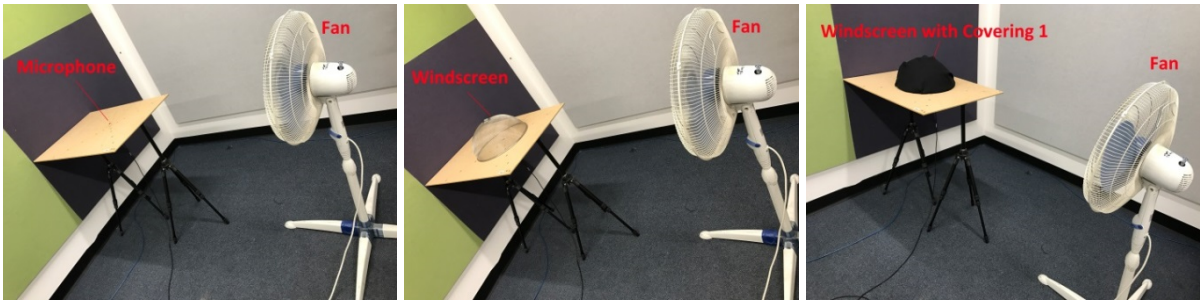

(a) (b) (c)

Figure 4.22 The experimental setup for (a) without windscreen, (b) with a semi-spherical metal mesh windscreen, (c) with a semi-spherical metal mesh windscreen covered with a cloth.

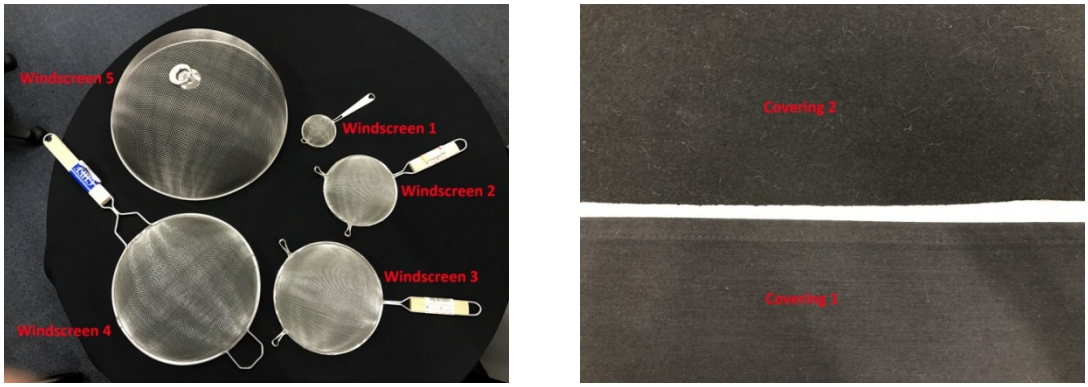

(a) (b)

Figure 4.23 (a) The five semi-spherical metal mesh windscreens and (b) the two covering cloths used in the experiments.

Table 4.1 The diameters of the semi-spherical metal mesh windscreens in Figure 4.23(a)

Windscreens	Windscreen 1	Windscreen 2	Windscreen 3	Windscreen 4	Windscreen 5
Diameter (cm)	7	14	20	27	35

Then two or more windscreens are combined to form the multi-layer windscreens to investigate the effect of the secondary windscreen on the wind noise reduction performance.

In addition, the effect of the fabric coverings on the wind noise reduction is also investigated. Two types of cloths are used as the covering in the experiments: a thin table cloth and thick curtain, as shown in Figure 4.23(b).

In addition to the above wind noise reduction measurements, the insertion loss of the sound signal due to the windscreens is also measured. The insertion loss is defined as the sound pressure level difference when the windscreen is absent and present, respectively, namely,

$$IL = L_{p,\mathrm{wo}} - L_{p,\mathrm{ws}}, \tag{4.10}$$

where $L_{p,\mathrm{ws}}$ and $L_{p,\mathrm{wo}}$ are the sound pressure levels measured with and without the windscreens, respectively. In the experiments, a B&K type 4295 omnidirectional sound source is used to generate the white noise signal. The measurement results for both the wind noise reduction and the insertion loss are illustrated and discussed in the next section.

4.4.2 Results and discussions

A. Size effect

To investigate the effect of the windscreen size on the wind noise reduction performance of the semi-spherical metal mesh windscreens, the wind noise is measured when the windscreen is absent and present, respectively. The measured wind noise levels are compared in Figure 4.24 for different mean wind speeds. It can be seen that the wind noise inside the semi-spherical metal mesh windscreen with a diameter of 20 cm (black dotted lines in Figure 4.24) is the lowest for all the three wind speeds. This can be more clearly observed from Table 4.2 for the overall wind noise reduction in the frequency range from 10 Hz to 1000 Hz. The maximum overall wind noise reduction is 13.4 dB, which is achieved by the 20 cm windscreen. The windscreens larger than 20 cm have smaller wind noise reduction. This is

consistent with the simulation results by Zhao et al. [131] that the larger windscreens may generate more wake turbulence that deteriorate the performance.

It is noteworthy that Table 4.2 shows that the overall wind noise reduction also varies with the mean wind speed for the same windscreens, and the wind noise reduction is the lowest at the moderate wind speed (U = 3.0 m/s). This is different from the measurement results by Lin et al. [47] that the wind noise reduction is found to increase with the mean wind speed above 2.0 m/s . The reason might be that the air flow in their experiments is non-turbulent while the air flow here is turbulent. For turbulent incoming flows, the pressure fluctuations depend on both the mean wind speed and the turbulence intensity, which is defined as the ratio of the root mean square velocity to the mean wind speed.

Table 4.2 The overall Wind Noise Reduction (dB) in the frequency range from 10 Hz to 1000 Hz for the single-layer windscreens

WNR (dB)	Windscreen 1 (D = 7 cm)	Windscreen 2 (D = 14 cm)	Windscreen 3 (D = 20 cm)	Windscreen 4 (D = 27 cm)	Windscreen 5 (D = 35 cm)
U = 2.1 m/s	9.8	12.7	13.4	13.2	10.9
U = 3.0 m/s	6.6	7.5	10.8	7.2	5.0
U = 4.2 m/s	4.4	8.8	13.4	10.2	8.7

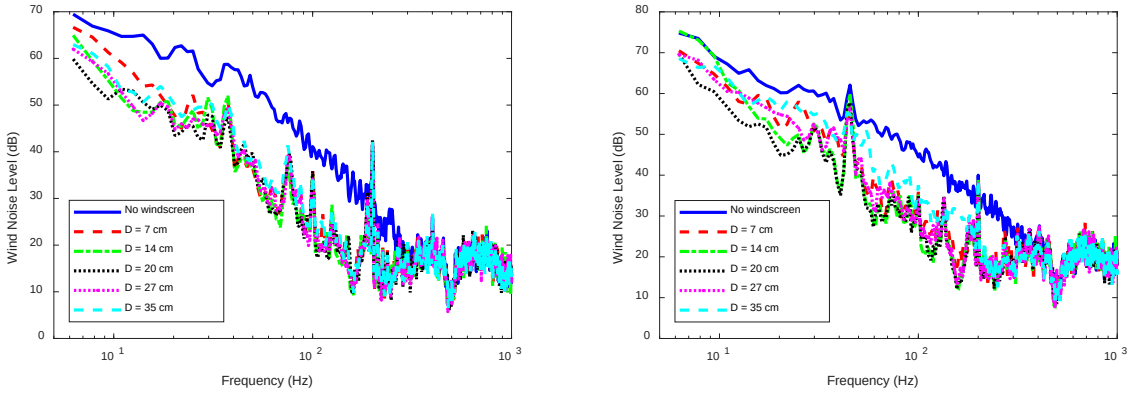

(a) (b)

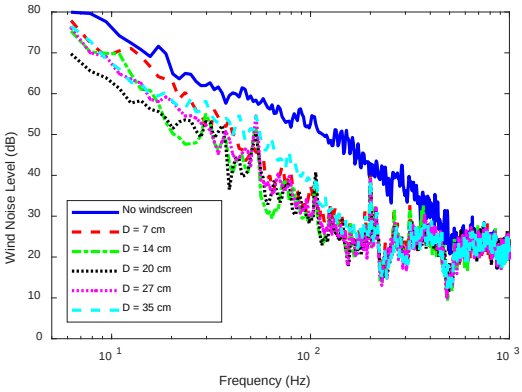

(c)

Figure 4.24 The wind noise level (dB) measured by the microphone with and without windscreens at the wind speed of (a) U = 2.1 m/s, (b) U = 3.0 m/s and (c) U = 4.2 m/s.

B. Multi-layer windscreens

To investigate the effect of secondary windscreens on the wind noise reduction performance, the semi-spherical metal mesh windscreens are combined to form multi-layer windscreens. The wind noise reduction of the multi-layer windscreens is measured and compared to that of the single-layer windscreen in Figure 4.25, where "Windscreen 1+2" denotes the two-layer windscreen with a combination of Windscreen 1 (D = 7 cm) and Windscreen 2 (D = 14) in Table 4.1, and the same for the others. It can be seen that the extra windscreen introduces dramatic additional wind noise reduction, especially in the frequency

range below 100 Hz. The wind noise reduction increases with the number of layers, as illustrated in Table 4.3 for the overall wind noise reduction in the frequency range from 10 Hz to 1000 Hz. The five-layer windscreen can attenuate the wind noise by 18.2 dB, which is 4.8 dB higher than the maximum wind noise reduction achieved by the single-layer windscreen (13.4 dB) in Table 4.2.

Table 4.3 The overall wind noise reduction (dB) in the frequency range from 10 Hz to 1000 Hz for the multi-layer windscreens

Windscreens	Single-layer	Two-layer	Three-layer	Four-layer	Five-layer
Wind Noise Reduction (dB)	6.7	14.2	15.0	17.0	18.2

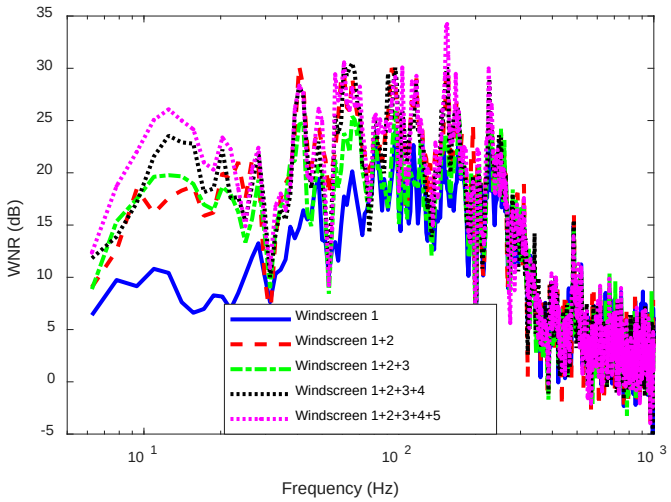

Figure 4.25 Comparison of the wind noise reduction (dB) of the multi-layer windscreens with the single-layer windscreen.

C. Covering effect

The wind noise reduction of the single-layer windscreens covered with the fabric cloth is compared with that of the original semi-spherical metal mesh windscreens in Figure 4.26 for the windscreens of diameter D = 7 cm (Windscreen 1) and D = 35 cm (Windscreen 2),

respectively. It can be seen that covering the windscreens with fabric cloth can increase the wind noise reduction and the thick cloth (covering 2) attenuates more wind noise than the thin cloth (covering 1). This can be clearly observed from Table 4.4, where the overall additional wind noise reduction due to the covering is summarised. The thin cloth (covering 1) and thick cloth (covering 2) can introduce additional 1.0 ~ 3.5 dB and 3.0 ~ 7.0 dB wind noise reduction, respectively, compared to the original semi-spherical metal mesh windscreens.

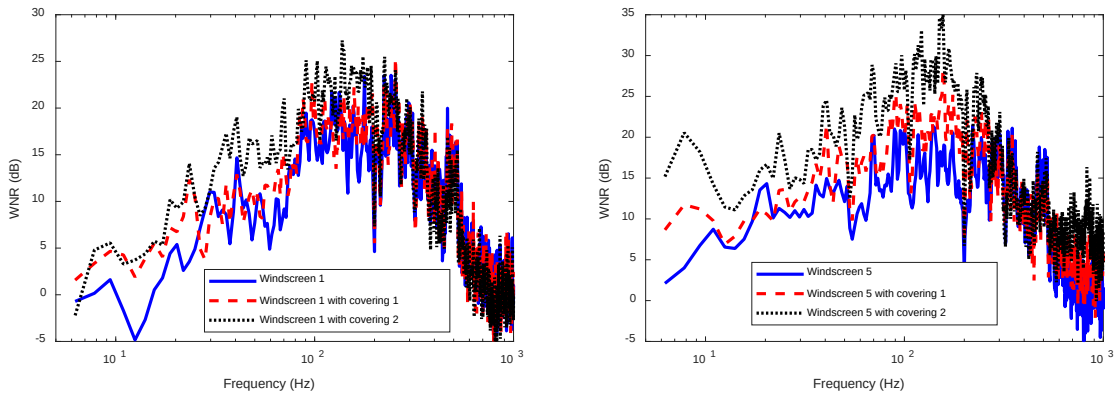

(a) (b)

Figure 4.26 Comparison of the wind noise reduction (dB) of the windscreens with covering and that of the original semi-spherical metal mesh windscreens of diameter (a) D = 7 cm and (b) D = 35 cm.

Table 4.4 The additional wind noise reduction (dB) in the frequency range from 10 Hz to 1000 Hz for the windscreens with coverings.

Additional WNR (dB)	Windscreen 1	Windscreen 2	Windscreen 3	Windscreen 4	Windscreen 5
Covering 1	2.1	3.2	1.5	1.0	3.5
Covering 2	3.0	6.8	3.1	5.1	7.0

D. Insertion loss

A perfect microphone windscreen should be transparent to the desired sound signal while attenuating the wind noise. Therefore, the insertion loss of the windscreens to the sound signal should be as small as possible. The insertion loss of the single-layer windscreens with and without coverings is compared in Figure 4.27, which shows that the insertion loss of the original semi-spherical metal mesh windscreen varies from 0.1 dB to 0.4 dB. However, covering the windscreens with the fabric cloths introduces more insertion loss while reducing more wind noise. The insertion loss of the windscreens covered with the thin cloth (covering 1) and thick cloth (covering 2) are 1.1 ~ 1.8 dB and 1.7 ~ 2.2 dB, respectively.

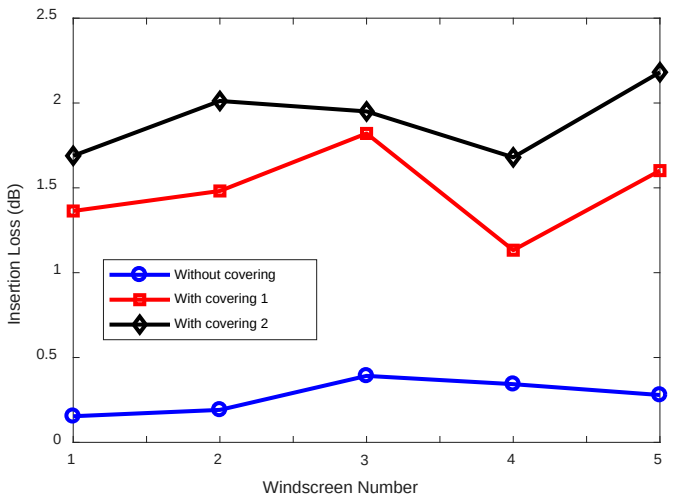

Figure 4.27 Comparison of the insertion loss (dB) of the windscreens with covering and that of the original semi-spherical metal mesh windscreens.

Table 4.5 The overall insertion loss (dB) in the frequency range from 10 Hz to 1000 Hz for the windscreens with and without coverings.

Insertion Loss (dB)	Windscreen 1	Windscreen 2	Windscreen 3	Windscreen 4	Windscreen 5	Five-layer windscreen
Without Covering	0.1	0.2	0.4	0.3	0.3	0.6
With Covering 1	1.4	1.5	1.8	1.1	1.6	--
With Covering 2	1.7	2.0	1.9	1.7	2.2	--

The insertion loss of the five-layer windscreens without coverings is 0.6 dB, as shown in the last column in Table 4.5. This shows that the five-layer windscreen is superior to the windscreens with coverings because it shows larger wind noise reduction but smaller insertion loss. In addition, by comparing Figure 4.25 and Figure 4.26, it can be seen that the multi-layer windscreens can attenuate more wind noise in the low frequency range below 30 Hz, which is desired for outdoor wind turbine noise measurements.

In summary, the wind noise reduction and the insertion loss of the semi-spherical metal mesh microphone windscreens were measured for the single-layer windscreens with and without coverings, and the multi-layer windscreens. For the single-layer windscreens without coverings, the insertion loss is below 0.4 dB and the maximum wind noise reduction is achieved by the middle size windscreens (D = 20 cm). Covering the single-layer windscreens with the fabric cloths can introduce additional 1.0 ~ 7.0 dB wind noise reduction, but also lead to higher insertion loss (1.1 ~ 2.2 dB). The five-layer windscreen is recommended because it shows high wind noise reduction (18.2 dB) and low insertion loss (0.6 dB).

4.4.3 Conclusions

This section investigates both the wind noise reduction and the insertion loss of the semi-spherical metal mesh windscreens by indoor experiments. Five single-layer windscreens were

measured to study the effect of the windscreen size on the noise reduction performance, and the mid-sized windscreen with a diameter of 20 cm was found to provide the maximum wind noise reduction. Covering the single-layer windscreens with a thin and thick cloth introduced an additional 1.0 ~ 3.5 dB and 3.0 ~ 7.0 dB wind noise reduction, but also increased the insertion loss to 1.1 ~ 2.2 dB. The multi-layer windscreens were found to improve the wind noise reduction while keeping the insertion loss small, which is superior to the fabric coverings. The best performance was achieved by the five-layer windscreen, with an 18.2 dB wind noise reduction and a 0.6 dB insertion loss. Future work includes conducting outdoor measurements and performing detailed measurements of the turbulence intensity of the incoming flow to analyse the effect of wind velocity on the wind noise reduction.

4.5 Summary

In summary, this chapter investigates the wind noise reduction mechanism of porous microphone windscreens and the wind noise reduction of the semi-spherical shell windscreens. The following conclusions are drawn from the simulations and experimental results.

Firstly, the effects of the viscous and inertial forces on the wind noise reduction performance of porous microphone windscreens were studied with a single microphone inside the windscreens in Section 4.2. The wind noise reduction was found to first increase and then slightly decrease with both the viscous and inertial coefficients after reaching a maximum. Experimental results show that the 40 PPI windscreen has the highest wind noise reduction performance among five porous windscreens with porosity from 20 to 60 PPI, which supports the simulation results. Therefore, the design of porous microphone windscreens should balance the turbulence suppression inside and the wake generation behind the porous windscreens to achieve the optimal performance.

Secondly, two microphones were used to study the spatial structure of wind noise and the effect on porous microphone windscreens on wind noise structure in Section 4.3. The magnitude squared coherence of the pressure measured with two microphones was found to decrease with the separation distance and the wind noise is spatially correlated only within a certain distance less than the turbulence wavelength. The porous windscreen was found to be the most effective in attenuating wind noise in a certain frequency range, where the windscreen diameter is approximately 2 to 4 times the turbulence wavelengths ($2 < D_0/\xi < 4$), regardless of the wind speed and windscreen diameter. The spatial coherence between the wind noise outside and inside a porous microphone windscreen was compared with that without the windscreen, and the coherence was found to decrease significantly when the windscreen diameter is approximately 2 to 4 times the turbulence wavelengths, corresponding to the most effective wind noise reduction frequency range of the windscreen. Experimental results with a fan are presented to support the simulations.

Finally, both wind noise reduction and insertion loss of the semi-spherical shell microphone windscreens were measured in Section 4.4. It was found that the semi-spherical metal mesh windscreen with a fabric covering improves the wind noise reduction performance, but also increases the insertion loss to more than 1 dB, leading to inaccurate sound level measurements. In contrast, the multi-layer windscreens can dramatically raise the wind noise reduction, especially in the low frequency range below 100 Hz, while keeping the insertion loss within 0.6 dB. Therefore, the multi-layer windscreen is superior to the windscreens with fabric coverings.

Future work includes

- conducting outdoor measurements of the wind noise reduction of porous microphone windscreens and semi-spherical shell windscreens;

- performing detailed measurements of the velocity fluctuations and turbulence intensity inside and outside porous microphone windscreens; and
- building porous microphone windscreens with variable porosity to further reduce wind noise.

5 Wind noise reduction with a spherical microphone array

The work presented in this chapter has been submitted to *The Journal of the Acoustical Society of America* and *Applied Acoustics*, both of which are now under review. Please see Appendix A for details.

5.1 Introduction

Spherical microphone arrays, in which the microphones are mounted around the surface of a sphere, have been widely studied in the past decade and become attractive tools for sound source localisation. Spherical microphone arrays offer several advantages over classical linear, planar and circular arrays, e.g., the spherical array beamforming can be designed to enhance or attenuate sources in any direction due to the rotational symmetry; efficient algorithms can be developed in the spherical harmonics domain; beamforming can be implemented by decoupling beam pattern design from beam pattern steering, which provides simplicity and flexibility in array realization [132].

Spherical microphone arrays have been used in room acoustics such as the geometry inference [133], acoustic absorption analysis [134], binaural reproduction [135], and arrival direction estimation [136,137] *etc*. They are also promising for outdoor wind turbine noise measurements due to its small size and portability, as well as noise source localization capability. However, the effect of wind noise caused by turbulent pressure fluctuations on the performance of spherical microphone arrays remains unknown. This chapter explores the potential applications of spherical microphone arrays on wind noise reduction and investigates the effect of wind noise on the spherical beamforming performance.

The signal processing of a spherical microphone array is usually realized in the spherical harmonics domain, based on spherical harmonic decomposition, i.e., a function $p(\theta, \phi)$ can be represented using a weighted sum of spherical harmonics, as [132]

$$p(\theta,\phi) = \sum_{n=0}^{\infty} \sum_{m=-n}^{n} p_{nm} Y_n^m(\theta,\phi) \tag{5.1}$$

where (θ, ϕ) is angular position on the sphere, p_{nm} is the spherical harmonics coefficients, and $Y_n^m(\theta, \phi)$ is the spherical harmonics function of order n (n = 0, 1, …, N) and degree m (m = $-n$, $-n$+1, …, 0, 1, …, n), which is defined as

$$Y_n^m(\theta,\phi) = \sqrt{\frac{2n+1}{4\pi}\frac{(n-m)!}{(n+m)!}} P_n^m(\cos\theta) e^{im\phi} \tag{5.2}$$

where $P_n^m(\cdot)$ is the associated Legendre functions, i is the imaginary unit, and $(\cdot)!$ is the factorial operator. The spherical harmonics coefficients can be obtained from the spherical Fourier transform, i.e.,

$$p_{nm} = \int_0^{2\pi} \int_0^{\pi} p(\theta,\phi) \left[Y_n^m(\theta,\phi) \right]^* \sin\theta d\theta d\phi \tag{5.3}$$

where the superscript * denotes the complex conjugate.

In practice, the number of microphones in the spherical array is limited, and the estimation of the sound pressure on the measurement sphere depends on the sampling scheme. In this case, the spherical Fourier transform in Eq. (5.3) needs to be discretised using a summation rather than integration, which can be written in matrix form as,

$$\mathbf{p}_{nm} = \mathbf{Y}^{\dagger}\mathbf{p} \tag{5.4}$$

where the superscript † denotes the pseudo inverse operation, $\mathbf{p} = [p(\theta_1, \phi_1), \ldots, p(\theta_q, \phi_q), \ldots, p(\theta_Q, \phi_Q)]^{\mathrm{T}}$, $p(\theta_q, \phi_q)$ is the pressure signal at the q-th microphone and Q is the total number of microphones in the spherical microphone array. $\mathbf{p}_{nm} = [p_{00}, p_{1(-1)}, p_{10}, p_{11}, \ldots, p_{NN}]^{\mathrm{T}}$ are the spherical harmonics coefficients, N is the highest order of the decomposition, and the matrix $\mathbf{Y}$ of dimensions $Q \times (N+1)^2$ is given by

$$\mathbf{Y} = \begin{bmatrix} Y_0^0(\theta_1,\phi_1) & \mathsf{L} & Y_n^m(\theta_1,\phi_1) & \mathsf{L} & Y_N^N(\theta_1,\phi_1) \\ \mathsf{M} & \mathsf{O} & \mathsf{M} & \mathsf{O} & \mathsf{M} \\ Y_0^0(\theta_q,\phi_q) & \mathsf{L} & Y_n^m(\theta_q,\phi_q) & \mathsf{L} & Y_N^N(\theta_q,\phi_q) \\ \mathsf{M} & \mathsf{O} & \mathsf{M} & \mathsf{O} & \mathsf{M} \\ Y_0^0(\theta_Q,\phi_Q) & \mathsf{L} & Y_n^m(\theta_Q,\phi_Q) & \mathsf{L} & Y_N^N(\theta_Q,\phi_Q) \end{bmatrix} \tag{5.5}$$

In this chapter, a spherical microphone array with 64 microphones mounted on a rigid sphere of diameter 20 cm is used to reduce wind noise without degrading the desired sound signal first, and then the effect of wind noise on the beamforming performance is investigated.

5.2 Wind noise characterisation and reduction with a spherical microphone array

This section utilizes a rigid spherical microphone array to characterize and reduce wind noise. The sound signal and wind noise are first measured with the spherical microphone array separately and analysed in the spherical harmonics domain. Then, a low pass filter method in the spherical harmonics domain is proposed to be used to reduce the wind noise but retain the desired sound signal. Experimental results demonstrate the feasibility of the proposed method in situations where the wind noise spectrum masks the sound signal.

5.2.1 Proposed method

A low pass filter method in the spherical harmonics domain (illustrated in Figure 5.1), is proposed to reduce wind noise captured by a spherical microphone array. The recorded signals are first transformed to the spherical harmonics domain via the discrete spherical Fourier transform in Eq. (5.4). Different modes of the spherical harmonics function represent different patterns. For example, the first mode $Y_0^0(\theta, \phi)$ represents a monopole pattern, the spherical harmonics of the order $n = 1$ are dipole patterns, and higher modes have more complex patterns [132]. For a low frequency sound signal with long wavelength, the spherical microphone array has little effect on the sound propagation and most of the sound

energy is dominated at the first few modes of the spherical harmonics. However, for the wind noise, the distribution of the noise energy along the sphere shows more complex patterns. This will be illustrated by the experimental results in the following sections.

In consideration of the abovementioned difference between the characterization of the sound signal and wind noise in the spherical harmonics domain, this thesis proposes to filter out the wind noise by applying a low pass filter to the spherical harmonics coefficients, i.e.,

$$\mathbf{p}'_{nm} = \mathbf{w}_{nm} \cdot \mathbf{p}_{nm} \tag{5.6}$$

where $\mathbf{p}'_{nm}$ are the filtered spherical harmonics coefficients, $\mathbf{w}_{nm} = [w_{00}, w_{1(-1)}, w_{10}, w_{11}, \ldots, w_{NN}]^T$ are the low pass filter coefficients in the spherical harmonics domain. For brevity without loss of generality, a simple rectangular low pass filter is used here, i.e.,

$$w_{nm} = \begin{cases} 1, & l \le M, \\ 0, & l > M. \end{cases} \tag{5.7}$$

where $l = n(n+1)+m+1$ is the mode number, and M is the threshold mode number above which the spherical harmonics are filtered out.

After low pass filtering in the spherical harmonics domain, the spatial domain signals can be derived from the low pass filtered harmonics coefficients with the discrete inverse spherical Fourier transform

$$\mathbf{p}' = \mathbf{Y}\mathbf{p}'_{nm} \tag{5.8}$$

where $\mathbf{p}'$ is the obtained sound signal after wind noise reduction.

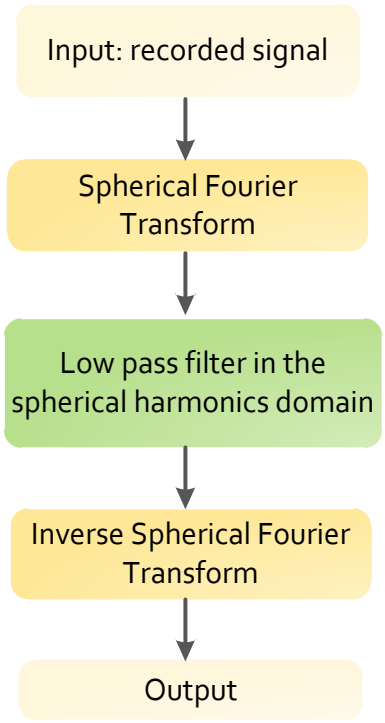

Figure 5.1 The diagram of the proposed spherical harmonic domain low pass filter method for wind noise reduction with a spherical microphone array.

The advantage of the proposed method is that the desired sound signal can be extracted from wind noise even when the sound signal is much lower in amplitude than the wind noise. In addition, contrasting with existing wind noise reduction structures, e.g., large spatial filters [78] and wind fence enclosures [8], the proposed method uses only a portable spherical microphone array, which is convenient for outdoor noise measurements. Finally, the proposed method is flexible and can be extended to spherical beamforming for future sound source localization. The feasibility of the proposed method will be verified by experiments and discussed in the next section.

5.2.2 Experimental results

A. Experiment setup

The experiments were performed in an anechoic chamber with the experimental setup illustrated in Figure 5.2. A commercial axial fan was used to generate the wind noise and a B&K Type 4295 omnidirectional loudspeaker was employed to produce the sound signal. A Visisonics spherical microphone array with 64 microphones on a 20 cm diameter rigid sphere was utilized to measure the pressure fluctuations due to the sound signal and wind noise [138]. The spherical microphone array was placed in the middle of the anechoic chamber, and the fan and the loudspeaker were both 1.4 m away from the spherical microphone array. The fan was located at a direction of (90°, 0°) relative to the spherical microphone array, where (θ, ϕ) denotes the elevation angle and azimuth angle. The loudspeaker was placed at a variety of positions, but only results for the same direction as the fan (90°, 0°) are presented here for brevity because the results for other directions are similar.

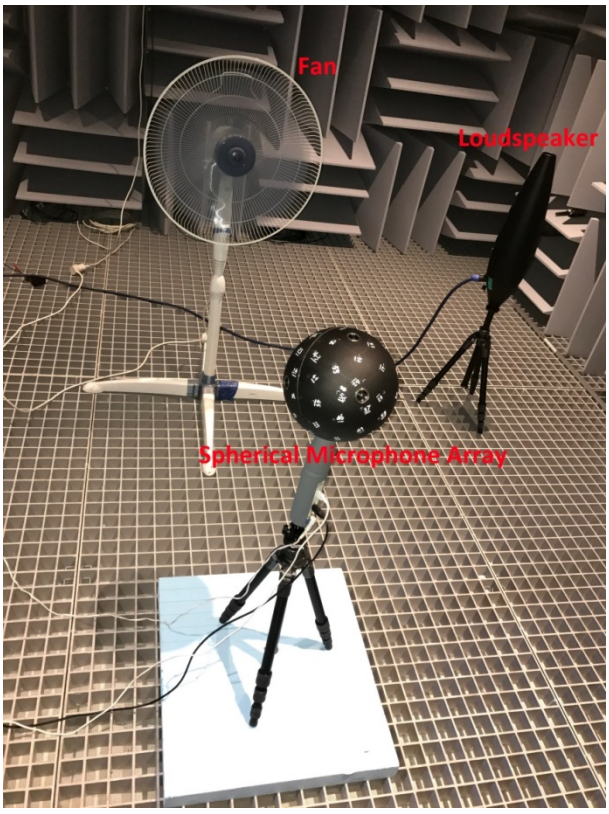

Figure 5.2 The experimental setup for wind noise measurement with a spherical microphone array in an anechoic chamber.

In the experiments, the sound signal was recorded first when the loudspeaker was active without the fan running, and then the wind noise was recorded when the fan was running alone. Finally, the sound signal, contaminated with wind noise, was recorded with both the loudspeaker and fan active. The time length for each recording is 30 s, which was divided into segments of 1 s for Fast Fourier Transform (FFT) calculation and spherical harmonic decomposition. The characteristics of the sound signal and wind noise were analysed in the spherical harmonics domain first, and then the difference between them utilized to filter out the wind noise in the spherical harmonics domain. The recording is

Figure 5.3 compares the recorded time domain signals at the front of the sphere near the stagnation point (100°, 0°) and at the rear of the sphere (100°, 180°). It can be observed from Figure 5.3(a) that the low frequency sound signal at 150 Hz is similar at both the front and rear of the sphere, indicating that the sound signal is uniform around the sphere. In contrast, Figure 5.3(b) shows that the wind noise at the front of the sphere is much higher than that at the rear of the sphere, implying a complex distribution pattern of wind noise around the sphere. Figure 5.3(c) and (d) present the wind noise contaminated sound signal when the sound signal is 10 dB higher and 3 dB lower in amplitude than the wind noise at the signal frequency, respectively, and clearly show that the sound signal is significantly distorted by wind noise in the time domain. While the spectral and spatial characteristics of the wind noise and sound signals are quite distinct, separation is difficult in the time domain. Hence, on the basis of the spherical microphone signals, the analysis was performed in the spherical harmonics domain in the next section.

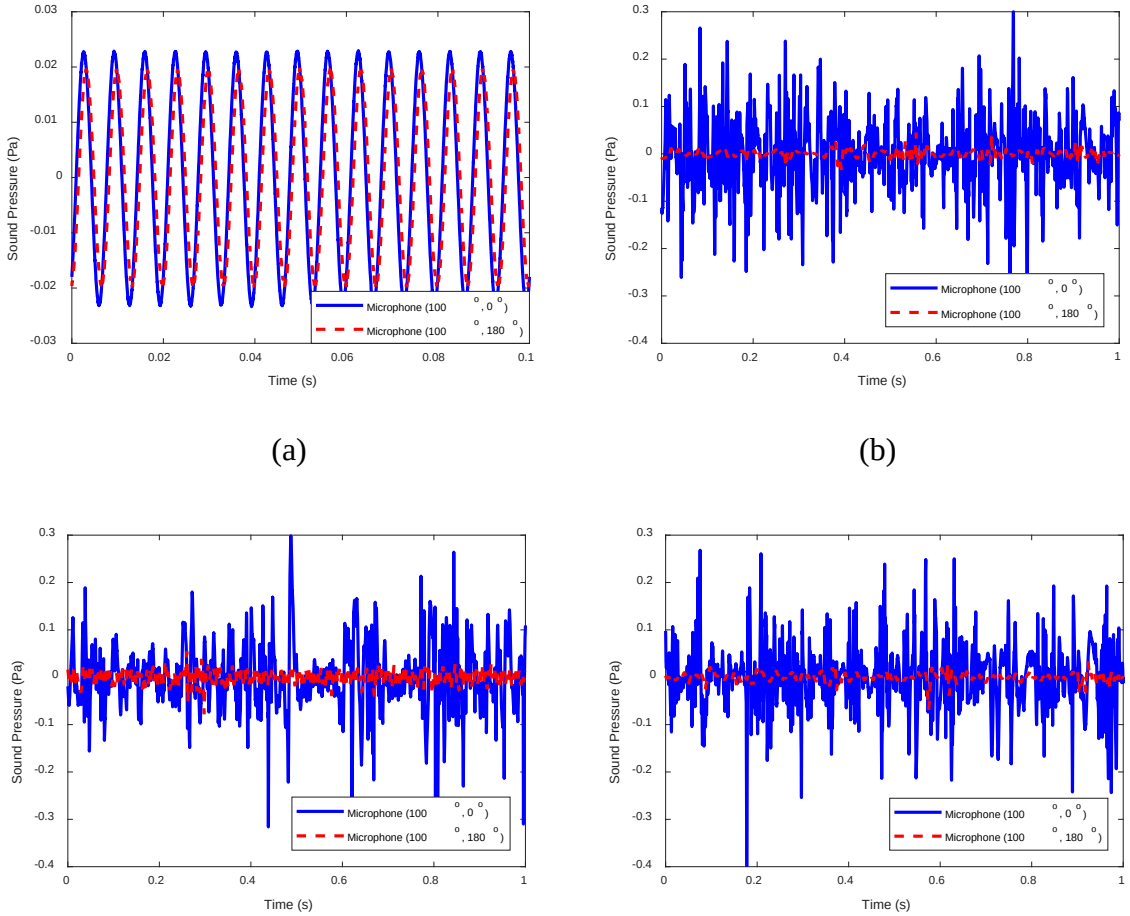

Figure 5.3 Comparison of the time domain signals measured at the front (100°, 0°) and the rear (100°, 180°) of the rigid spherical microphone array: (a) the 150 Hz tonal sound signal, (b) the wind noise, and the wind noise contaminated sound signal when the sound signal is (c) 10 dB higher and (d) 3 dB lower in amplitude than the wind noise. The mean wind speed at the spherical microphone array is U = 4.2 m/s.

B. The sound signal in the spherical harmonics domain

The measured sound pressure signals are substituted into Eq. (5.4) to calculate the spherical harmonics coefficients $\mathbf{p}_{nm}$, and the results for the sound signal without the fan running are shown in Figure 5.4 for frequencies 150 Hz and 500 Hz, respectively. In the calculation, the highest order N = 6, so there are $L = (N+1)^2$ = 49 modes in the spherical

harmonic decomposition. The abscissa mode number in Figure 5.4 is $l = n(n+1)+m+1$, where $l = 1$ represents the first mode $Y_0^0(\theta, \phi)$ and the $l = 49$ indicates the highest mode $Y_N^N(\theta, \phi)$.

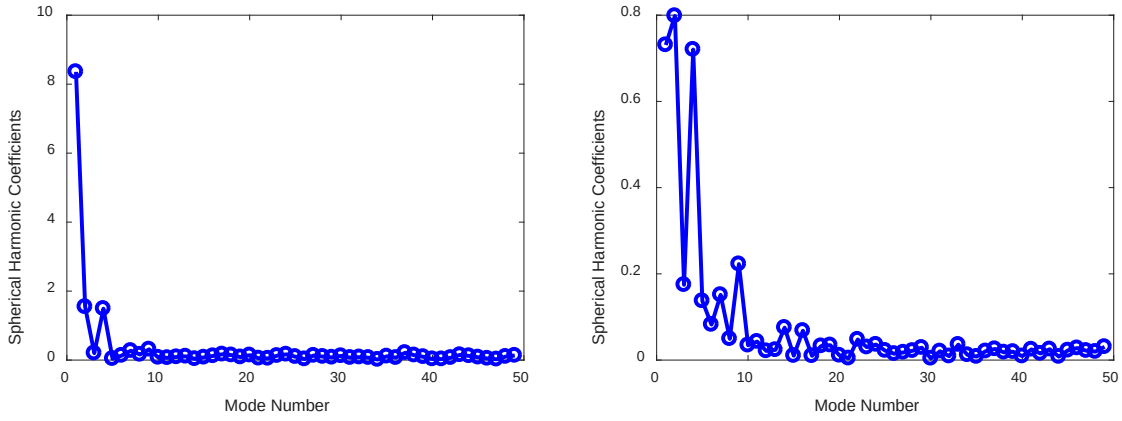

(a) (b)

Figure 5.4 The spherical harmonics coefficients for the tonal sound signal at the frequency of (a) 150 Hz and (b) 500 Hz.

Figure 5.4(a) shows that when the sound signal is at 150 Hz, the spherical harmonic coefficient for the first mode is much larger than that for higher modes, indicating that the sound energy is predominantly in the first mode. To quantify the percentage of sound energy contained in the first L_0 modes, the cumulative energy ratio is calculated as

$$R = \frac{\sum_{l=1}^{L_0} C_l^2}{\sum_{l=1}^{L} C_l^2} \times 100\% \tag{5.9}$$

where C_l denotes the l-th spherical harmonic coefficient, L is the total number of spherical harmonic modes. The accumulative energy ratio for the sound signal at 150 Hz and 500 Hz corresponding to Figure 5.4 is summarized in Table 5.1. For the sound signal at 150 Hz, it is clear that 93.0% of the sound energy is contained in the first mode.

Table 5.1. The cumulative energy ratio (%) for the sound signal

Modes (L_0)	1	2	3	4	5	10
150 Hz	0.930	0.961	0.962	0.992	0.992	0.995
500 Hz	0.288	0.632	0.649	0.928	0.959	0.993

In acoustic measurements, the error in the Sound Pressure Level (SPL) is within 0.5 dB if 90% of the sound energy is captured. This implies that the measurement accuracy can be restricted to 0.5 dB by neglecting the higher modes but only retaining the first mode. To further verify this result, the low pass filter in the spherical harmonics domain with $M = 1$ is used in Eq. (5.6) to calculate the filtered spherical harmonics coefficients, which are substituted in Eq. (5.8) to obtain the filtered signal. Comparison of the filtered signal with the original signal in Figure 5.5(a) shows that the original SPL at 150 Hz is clearly extracted from the first mode with an error of 0.4 dB.

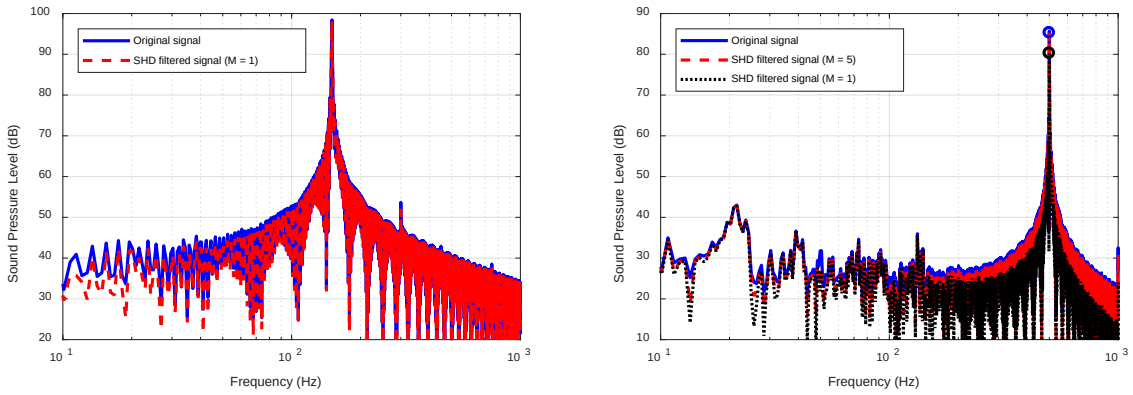

(a) (b)

Figure 5.5 Comparison of the original signal with the spherical harmonics domain filtered signal for the tonal sound at the frequency of (a) 150 Hz and (b) 500 Hz.

Similarly, Figure 5.4(b) shows that at 500 Hz, the spherical harmonic coefficients in the first few modes are much larger than those in higher modes, and Table 5.1 shows that 92.8%

of the sound energy is focused in the first 4 modes. A low pass filter in the spherical harmonics domain with $M = 5$ and $M = 1$ is applied and the filtered signal compared with the original signal in Figure 5.5(b). It can be seen that the desired SPL at 500 Hz can be extracted from the first 5 modes with an error of 0.3 dB. However, if only the first mode is utilized, the restored SPL is 5.5 dB lower than the original signal, which indicates that some of the sound energy is lost in the process.

The above results demonstrate that over 90% of the sound energy is contained in the first spherical harmonic mode at 150 Hz and in the first 4 modes at 500 Hz. Hence, a low pass filter in the spherical harmonics domain can restore the original SPL with an error less than 0.5 dB, and the threshold mode number M needs to be tuned for different frequency sound signals. For higher frequency sound signals, higher modes are needed to restore the SPL, as shown in Table 5.1. However, in the application scenario of wind noise reduction, the frequency range below 500 Hz is of greater interest because previous measurement results have shown that wind noise above 500 Hz is below 40 dB in both indoor and outdoor environments [119,139].

C. Wind noise in the spherical harmonics domain

The wind noise was measured first when the fan was running alone. In the experiment, the fan ran at three different speeds, and the mean wind speeds around the spherical microphone array were about 2.4 m/s, 3.3 m/s and 4.2 m/s, respectively. The spherical harmonics coefficients at frequencies 150 Hz and 500 Hz are shown in Figure 5.6 for 4.2 m/s. It can be observed that the spherical harmonics coefficients for the wind noise seem randomly distributed along the mode number in the spherical harmonics domain, which is different from that for the sound signals shown in Figure 5.4. To quantify the difference, Table 5.2 summarizes the cumulative energy ratio for the wind noise at different wind speeds.

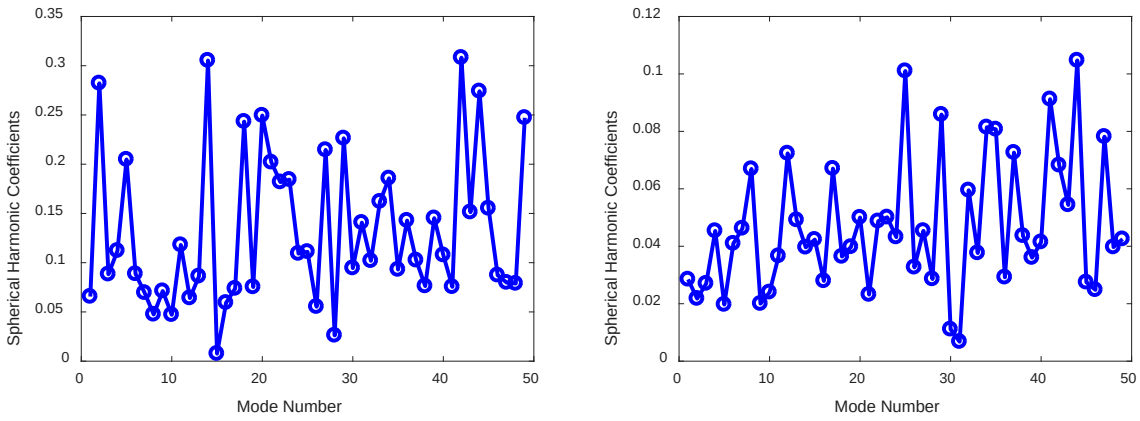

(a) (b)

Figure 5.6 The spherical harmonics coefficients for the wind noise at the frequency of (a) 150 Hz and (b) 500 Hz.

Table 5.2. The cumulative energy ratio (%) for the wind noise at different speeds

Modes (L_0)		1	2	3	4	5	10
U = 2.4 m/s	150 Hz	0.004	0.007	0.008	0.025	0.026	0.131
	500 Hz	0.012	0.021	0.023	0.033	0.063	0.162
U = 3.3 m/s	150 Hz	0.007	0.010	0.030	0.046	0.059	0.117
	500 Hz	0.001	0.016	0.036	0.051	0.092	0.138
U = 4.2 m/s	150 Hz	0.004	0.074	0.081	0.092	0.129	0.148
	500 Hz	0.006	0.010	0.015	0.031	0.034	0.104

It can be seen that less than 1% of the wind noise energy is contained in the first mode at 150 Hz, while less than 10% of the wind noise energy is contained in the first 4 modes at 500 Hz. This is dramatically different from the sound signals in Table 5.1, where over 90% of the sound energy is contained in the first mode at 150 Hz, and in first 4 modes at 500 Hz. In the acoustic measurements, if less than 1% and 10% wind noise energy are retained, the wind noise reductions are over 20 dB and 10 dB, respectively. Therefore, in comparison with Table

5.1 and Table 5.2, more than 20 dB and 10 dB wind noise reduction are expected at 150 Hz and 500 Hz, respectively, with a measurement accuracy of the desired SPL within 0.5 dB.

Figure 5.7(a) presents the magnitude of the spherical harmonics coefficients of the wind noise at different modes and frequencies below 1000 Hz. This shows that the wind noise is distributed randomly in the spherical harmonics domain at each frequency from 10 Hz to 1000 Hz. This implies that if the sound signal dominates in the lower order modes, then the wind noise can be reduced using the proposed low pass filter approach in the spherical harmonics domain by filtering out the higher modes. The filtered results with different threshold mode numbers are compared with the original signal in Figure 5.7(b), which shows that the wind noise is reduced in the whole frequency range from 10 Hz to 1000 Hz by the proposed low pass filtering in the spherical harmonics domain.

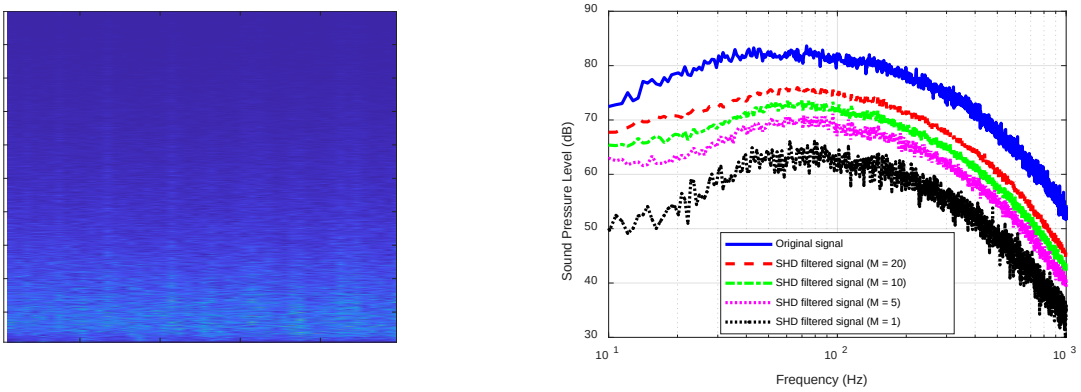

(a) (b)

Figure 5.7 (a) The magnitude of the spherical harmonics coefficients of the wind noise at different modes and frequencies, and (b) the comparison of the original signal and the spherical harmonics domain filtered signal with different threshold mode number.

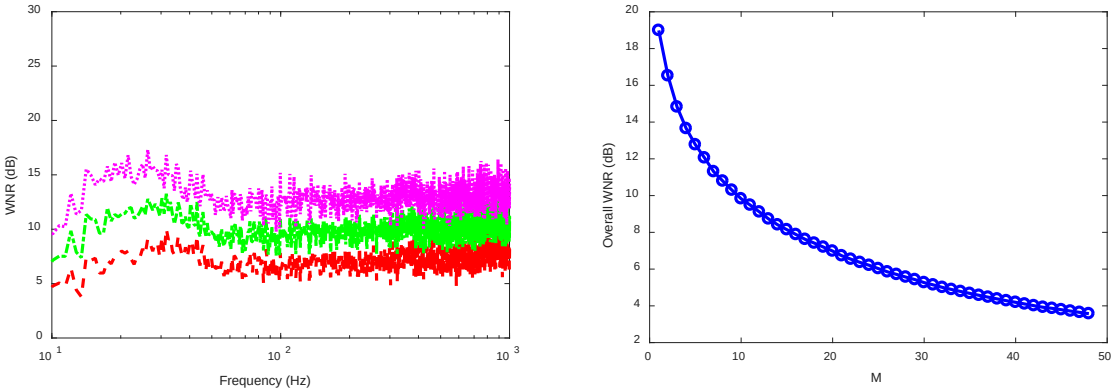

(a) (b)

Figure 5.8 (a) The wind noise reduction as a function of frequency for various threshold mode number *M*, and (b) the overall wind noise reduction as a function of the threshold mode number *M*.

This can be observed more clearly from Figure 5.8(a) for the wind noise reduction as a function of frequency. In addition, more wind noise is attenuated when fewer modes are used in the low pass filtering, as indicated in Figure 5.8(b), where the overall wind noise reduction (WNR) in the whole frequency range 10 Hz to 1000 Hz is shown as a function of the threshold mode number. The overall WNR decreases from 19.0 dB to 3.5 dB as the threshold mode number increases from 1 to 48.

The above results demonstrate that the spherical harmonics coefficients for the wind noise are randomly distributed at each frequency in the spherical harmonics domain, as opposed to the sound signal where the sound energy dominates at the first few spherical harmonics modes. This difference can be utilized to reduce wind noise while retaining the desired sound signal with the proposed low pass filter method in the spherical harmonics domain.

D. Wind noise reduction in the spherical harmonics domain

To investigate the performance of the proposed spherical harmonics domain low pass filter method when retrieving a sound signal from wind noise, a noisy sound signal was recorded with the spherical microphone array with both the loudspeaker and the fan operating. A single tonal sound signal at different frequencies was played through the loudspeaker to conduct two sets of experiments.

In the first set of experiments, the sound signal was higher in amplitude than the wind noise and the results are shown in Figure 5.9, where the spherical harmonics coefficients are presented for the noisy sound signal when the frequency of the sound signal is 150 Hz and 500 Hz, respectively. In Figure 5.9, the SPL of the desired sound signal is 10 dB and 8 dB higher than the wind noise at 150 Hz and 500 Hz, respectively. In this case, the difference between the sound and the wind noise in the spherical harmonics domain can be observed because the sound energy is higher than the wind noise at the same frequency, as illustrated by the red marker ellipses in Figure 5.9(a) and (b). On the other hand, the wind noise energy is randomly distributed across the frequency range in the spherical harmonics domain, which is consistent with Figure 5.7(a).

These observations indicate that the wind noise can be reduced by the proposed low pass filter method in the spherical harmonics domain as discussed in the previous section. The low pass filtered results are compared with the original signal in Figure 5.9(c) and (d) for the single tonal sound of frequency 150 Hz and 500 Hz, respectively. It can be observed from Figure 5.9(c) that when only the first mode is kept in the spherical harmonics domain, the wind noise is reduced by 19.2 dB across the whole frequency range from 10 Hz to 1000 Hz and the desired SPL at 150 Hz is retained with an error of 0.5 dB. For the 500 Hz tonal sound in Figure 5.9(d), when only the first mode is retained in the spherical harmonics domain (M = 1), the wind noise is significantly reduced by 19.2 dB but the desired sound signal is also degraded by 5.5 dB. When the first 5 modes are retained in the spherical harmonics domain

(M = 5), the wind noise is reduced by 13.0 dB across the whole frequency range from 10 Hz to 1000 Hz, and the desired SPL is degraded by 1.0 dB.

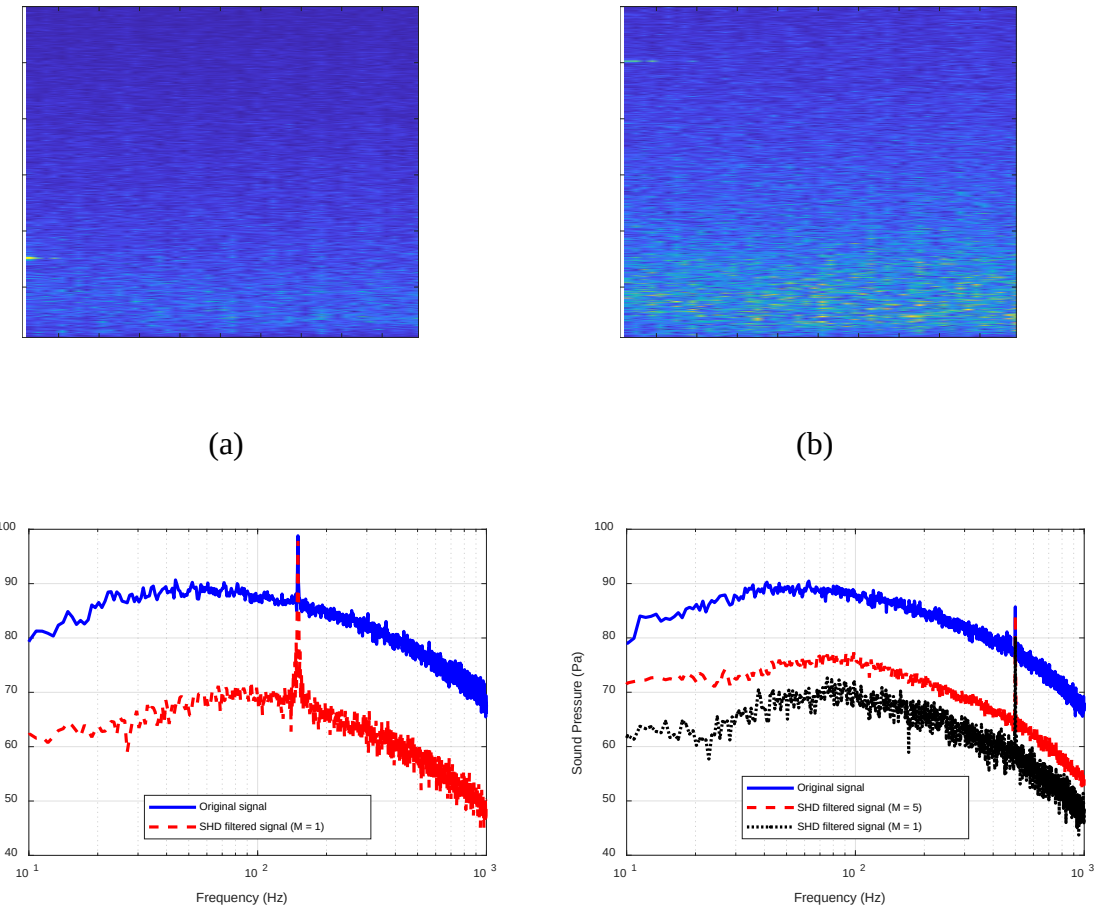

Figure 5.9 The magnitude of the spherical harmonics coefficients for the wind noise contaminated sound signal at different modes and frequencies for a sound signal at (a) 150 Hz and (b) 500 Hz, and comparison of the spherical harmonics domain low pass filtered signal with the original signal for the sound signal at (c) 150 Hz and (d) 500 Hz. The sound signal at 150 Hz and 500 Hz are 10 dB and 8 dB higher than the wind noise, respectively.

The above results demonstrate that when the sound signal is higher in amplitude than the wind noise, the proposed low pass filter method in the spherical harmonics domain can reduce the measured wind noise by 13.0 dB with the sound signal degradation less than 1.0 dB. In practical applications, the sound signal might be lower in amplitude than the wind noise. In this situation, the difference between the sound signal and wind noise cannot be seen in the spherical harmonics domain, as illustrated by Figure 5.10(a) and (b). However, the spherical harmonics domain low pass filtered results in Figure 5.10((c) and (d) demonstrate that the proposed method can still extract the desired sound signal from the wind noise.

For the 150 Hz tonal sound with a sound pressure level of 84 dB (3 dB lower than the wind noise), the low pass filtered results with $M = 1$ and $M = 5$ obtain the same sound level of 84 dB at 150 Hz in Figure 5.9(c). For the 500 Hz tonal sound with a sound pressure level of 71 dB (8 dB lower than the wind noise), the low pass filtered results with $M = 5$ and $M = 10$ derive almost the same sound level of 70 dB at 500 Hz, which are both about 5 dB higher than that with $M = 1$ as shown in Figure 5.9(d).

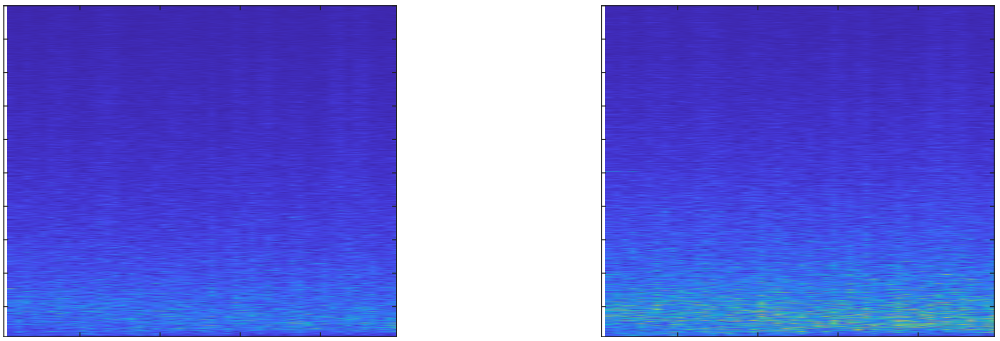

(a) (b)

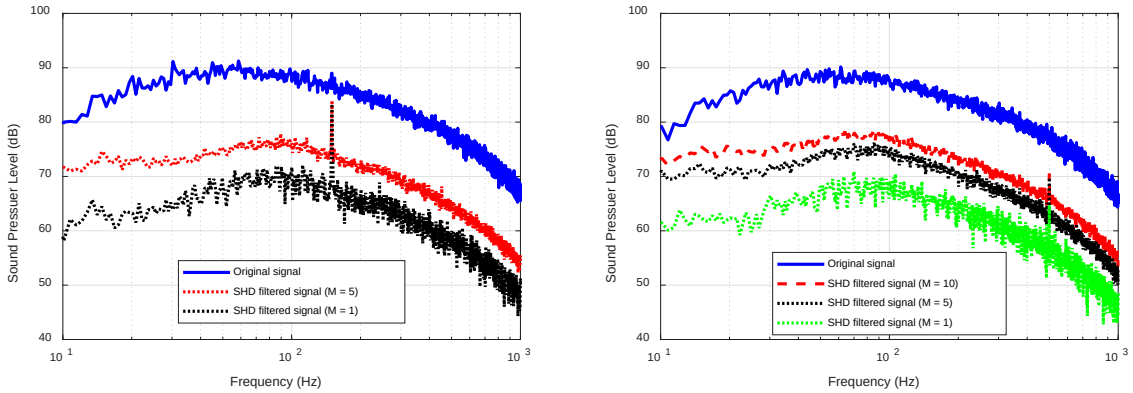

(c) (d)

Figure 5.10 The magnitude of the spherical harmonics coefficients of the wind noise contaminated sound signal at different mode and different frequency for sound signal at (a) 150 Hz and (b) 500 Hz, and comparison of the spherical harmonics domain low pass filtered signal with the original signal for the sound signal at (c) 150 Hz and (d) 500 Hz. The sound signal at 150 Hz and 500 Hz are 3 dB and 8 dB lower than the wind noise, respectively.

To further evaluate the performance of the proposed method, a multi-tonal signal consisting of 125 Hz, 250 Hz, and 500 Hz sounds was recorded in the presence of wind noise. The 125 Hz sound was 94 dB and 7 dB higher than the wind noise, the 250 Hz sound was 82 dB which is the same level as the wind noise, and the 500 Hz sound was 72 dB and 2.5 dB lower than the wind noise. The spherical harmonics domain low pass filtered signals with

different threshold mode numbers are compared with the original signal in Figure 5.11. It can be seen that when only the first mode is retained (M = 1), the error for 250 Hz and 500 Hz sounds is 1.5 dB and 3.0 dB, respectively, although the error for the 125 Hz sound is within 0.5 dB. When the first 5 modes are retained (M = 5), the error is within 1.0 dB for all the three tonal signals, and the wind noise is reduced by 10 dB. With more than 5 modes retained (e.g., M = 10), there is almost no further improvement in the measurement accuracy of the desired sound signals, but the wind noise reduction is decreased by 3 dB. Therefore, the threshold mode number M = 5 is considered appropriate for this case, with a 10 dB wind noise reduction and measurement error within 1.0 dB.

In summary, the above results demonstrate that the proposed low pass filter method in the spherical harmonics domain can extract the desired sound signal from the noisy signal even when the sound signal is lower in amplitude than the wind noise. In theory, more than 20 dB and 10 dB measured wind noise reduction are expected at 150 Hz and 500 Hz, respectively, with a measurement accuracy of the desired SPL within 0.5 dB, as shown in Table 5.1 and Table 5.2. In the experiments, 19.2 dB and 13.2 dB wind noise reductions were observed at 150 Hz and 500 Hz, respectively, with the measurement accuracy of the desired SPL within 1.0 dB. Experimental results with the multi-tonal sound signals show a wind noise reduction of 10 dB with the measurement error within 1.0 dB for all three tonal sounds.

It is noteworthy that the above results are based on the indoor fan test. For the potential full-field outdoor wind turbine testing, the sound signals should be similar to those in the current stage, e.g., most of the sound energy is focused in the first few modes in the spherical harmonics domain. The wind noise may be different in the following two aspects, first the wind direction keeps changing in outdoor environments, and second the turbulence scale in atmospheric turbulence is much larger than that in the wind produced by fans. The changing wind direction will not be a problem, because for real time processing, the wind direction can

be assumed to be constant in a short time period such as 1 second. On the other hand, the large scale turbulence might change the wind noise energy distribution in the spherical harmonics domain, which might affect the wind noise reduction performance. This will be investigated in the future with outdoor measurement of wind noise with the spherical microphone array.

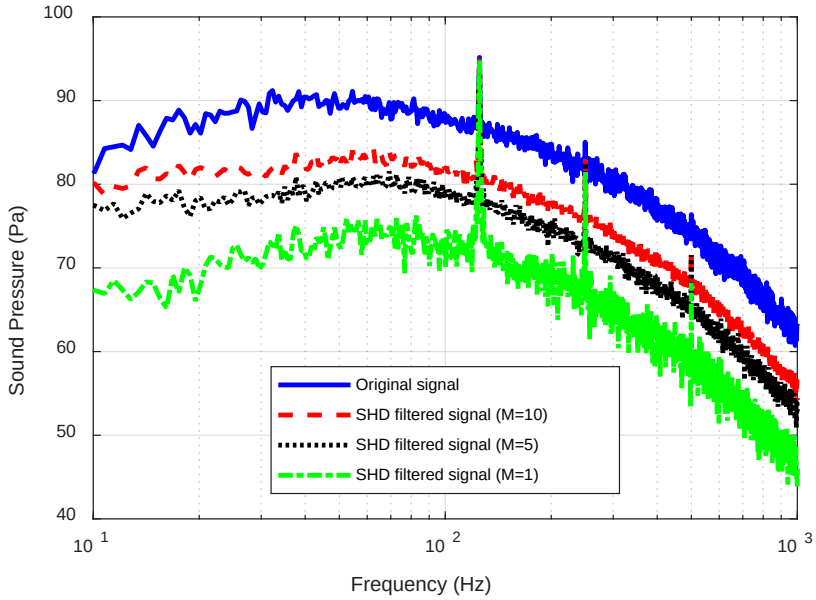

Figure 5.11 Comparison of the spherical harmonics domain low pass filtered signal with the original signal for the multi-tonal sound signal consisting of 125 Hz, 250 Hz and 500 Hz tonal sound.

5.2.3 Conclusions

This section utilized a portable rigid spherical microphone array to characterize and reduce wind noise without degrading the sound pressure level of the desired sound signal to be measured. The wind noise was found to be randomly distributed in the spherical harmonics domain at each frequency, contrasting with the sound signal that dominates in the first few spherical harmonics modes. A low pass filter method in the spherical harmonics

domain was proposed to reduce the wind noise while preserving the sound pressure level of the desired sound signal. Experimental results show that 19.2 dB and 13.2 dB wind noise reduction are observed at 150 Hz and 500 Hz, respectively, with the measurement accuracy of the desired sound pressure level within 1.0 dB, even when the sound signal is 8 dB lower than the wind noise. The proposed method was also validated with the measurements of the multi-tonal sound signals in the presence of wind noise, which showed a 10 dB wind noise reduction with the measurement error within 1.0 dB. Future work will extend the proposed method to sound source localization using beamforming algorithms in the spherical harmonics domain.

5.3 Wind noise effect on the beamforming performance of a spherical microphone array

In this section, the wind noise effect on the common spherical beamforming performance is investigated in the laboratory environment. In the experiments, a commercial axial fan is used to generate wind noise, which is measured with a rigid spherical microphone array and analyzed in the spherical harmonics domain. The effect of wind noise on the spherical harmonic beamforming performance of the Plane Wave Decomposition (PWD) beamformer, Delay and Sum (DAS) beamformer and Maximum Variance Distortionless Response (MVDR) beamformer are presented and compared in terms of the directivity factor first. Then, experimental results of the MVDR beamforming map with and without wind noise are illustrated and discussed for different Signal-to-Noise Ratio (SNR) at different frequencies.

5.3.1 Theoretical models

The recorded signals are first transformed to the spherical harmonics domain via the discrete spherical Fourier transform, i.e., [132]

$$\mathbf{x}_{nm} = \mathbf{Y}^{\dagger}\mathbf{x} \tag{5.10}$$

where the superscript † denotes the pseudo inverse operation, $\mathbf{x} = [x(\theta_1, \phi_1), \ldots, x(\theta_q, \phi_q), \ldots, x(\theta_Q, \phi_Q)]^{\mathrm{T}}$, $x(\theta_q, \phi_q)$ is the pressure signal at the q-th microphone and $Q = 64$ is the number of microphones in the spherical microphone array, $\mathbf{x}_{nm} = [x_{00}, x_{1(-1)}, x_{10}, x_{11}, \ldots, x_{NN}]^{\mathrm{T}}$ is the spherical harmonics coefficients, N is the highest order of the decomposition, and the elements of the matrix $\mathbf{Y}$ of dimensions $Q \times (N+1)^2$ defined in Eq. (5.8)

Three typical spherical beamforming algorithms are investigated, i.e., the PWD beamformer, the DAS beamformer, and the MVDR beamformer. The filter coefficients of all the three beamformers can be written in the following form with different matrix $\mathbf{B}$ [132]

$$\mathbf{w}_{nm}^{\mathrm{H}} = \frac{\mathbf{v}_{nm}^{\mathrm{H}}\mathbf{B}^{-1}}{\mathbf{v}_{nm}^{\mathrm{H}}\mathbf{B}^{-1}\mathbf{v}_{nm}} \tag{5.11}$$

where $\mathbf{v}_{nm} = [v_{00}, v_{1(-1)}, v_{10}, v_{11}, \ldots, v_{NN}]$, $v_{nm} = b_n(kr)[Y_n^m(\theta_l, \phi_l)]^*$, $b_n = 4\pi i^n[j_n(kr) - j_n'(ka)/h_n'(ka)h_n(kr)]$, j_n is the spherical Bessel function, h_n is the spherical Hankel function of the section kind, j_n' and h_n' are their derivatives, k and a are the wavenumber and array radius, respectively.

The PWD beamformer is based on the idea that the signals recorded by the spherical microphone array can be decomposed to plane waves with directional amplitude density, and the matrix $\mathbf{B}$ is given as [140]

$$\mathbf{B} = \frac{1}{4\pi} \cdot \mathrm{diag}\left(|b_0|^2, |b_1|^2, |b_1|^2, |b_1|^2, \mathrm{L}\ |b_N|^2\right) \tag{5.12}$$

The DAS beamformer has the attractive property of a constant white noise gain with a maximum robustness, and the matrix $\mathbf{B}$ is given as [132]

$$\mathbf{B} = \mathbf{Y}^{-1}\mathbf{Y}^{-\mathrm{H}} \tag{5.13}$$

The MVDR beamformer aims to minimize the output power subject to a distortionless constraint on the response in the look direction, and the matrix $\mathbf{B}$ is given as [141]

$$\mathbf{B} = \mathrm{E}\left[\mathbf{x}_{nm}\mathbf{x}_{nm}^{\mathrm{H}}\right] \tag{5.14}$$

where E[·] denotes the expectation operator. To improve the robustness of the MVDR beamformer, the frequency smoothing technique is applied [142]. In practical implementations, Eq. (5.14) is estimated by

$$\mathbf{B} = \frac{1}{I}\sum_{i=1}^{I} \mathbf{x}_{nm}(i)\mathbf{x}_{nm}{}^{\mathrm{H}}(i) \tag{5.15}$$

where I denotes the number of time domain snapshots [141].

When the array weights are determined with Eq. (5.11), the output of the spherical microphone array beamformer is written as

$$y(\theta,\phi) = \mathbf{w}_{nm}{}^{\mathrm{H}}\mathbf{x}_{nm} \tag{5.16}$$

In the presence of wind noise, the recorded signal can be written as the superposition of the sound signal $\mathbf{s}_{nm}$ and the wind noise $\mathbf{n}_{nm}$, i.e., $\mathbf{x}_{nm} = \mathbf{s}_{nm} + \mathbf{n}_{nm}$.

$$y(\theta,\phi) = \mathbf{w}_{nm}{}^{\mathrm{H}}(\mathbf{s}_{nm} + \mathbf{n}_{nm}) \tag{5.17}$$

Therefore the presence of wind noise introduces an extra term on the array output, i.e., the spherical harmonic coefficients of wind noise. In the following section, wind noise is measured with a spherical microphone array and analyzed in the spherical harmonics domain first, and then the effect of wind noise on the beamforming performance is studied with simulation and experiments. To quantitatively evaluate the beamforming performance, the Root Mean Square Error (RMSE) is defined to assess the accuracy of the sound source direction localization, i.e., [137]

$$RMSE = \sqrt{(\theta_0 - \theta_s)^2 + (\phi_0 - \phi_s)^2} \tag{5.18}$$

where (θ_s, ϕ_s) and (θ_0, ϕ_0) are the actual and estimated sound source direction, respectively. In addition, the Directivity Factor (DF) is calculated as [20]

$$DF = \frac{\left|y(\theta_0,\phi_0)\right|^2}{\frac{1}{4\pi}\int_0^{2\pi}\int_0^{\pi}\left|y(\theta,\phi)\right|^2 \sin\theta d\theta d\phi} \tag{5.19}$$

where $y(\theta, \phi)$ is the array output at the direction (θ, ϕ), and (θ_0, ϕ_0) is the front direction with a maximum array output power. The DF is a scalar that quantifies the array directivity and measures the ratio between the peak and the average array output power over all directions. It can be considered as the improvement of the signal-to-noise ratio provided by the array due to its directional response [132].

5.3.2 Simulations and experiments

A. Wind noise measurements

The experiments were performed in an anechoic chamber with the experimental setup illustrated in Figure 5.12. A commercial axial fan was used to generate the wind noise and a B&K Type 4295 omnidirectional loudspeaker was employed to produce the sound signal. A Visisonics spherical microphone array with 64 microphones on a 20 cm diameter rigid sphere was utilized to measure the pressure fluctuations due to the sound signal and wind noise [138]. The spherical microphone array was placed in the middle of the anechoic chamber, and the fan and the loudspeaker were both 1.4 m away from the spherical microphone array. The fan was located at a direction of (90°, 90°) relative to the spherical microphone array, where (θ, ϕ) denotes the elevation angle and azimuth angle.

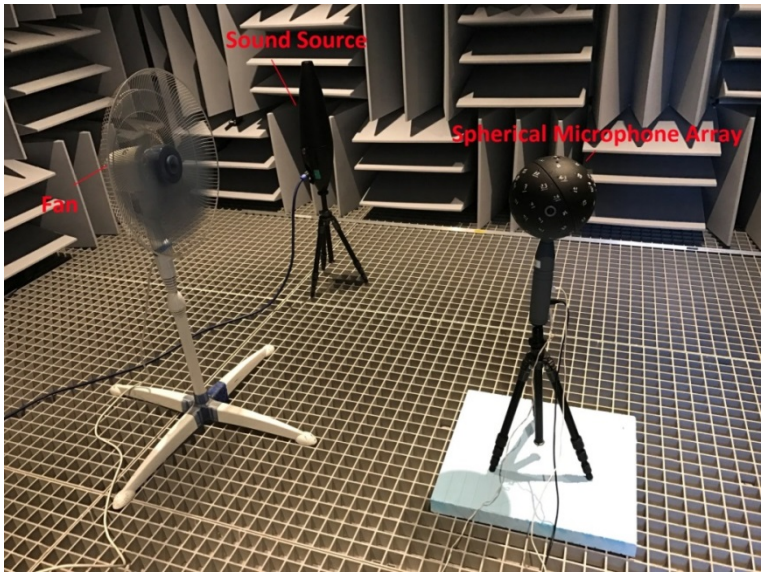

Figure 5.12. Experimental setup in the anechoic chamber.

The wind noise was first measured when the fan was running at its highest speed and the mean wind speed around the spherical microphone array is about 4.2 m/s. It was found that the distribution of the wind noise around the sphere is non-uniform and has complex patterns, e.g., the wind noise on the microphone at the front of the sphere is much higher than that at the rear of the sphere, as shown in Figure 5.13(a). This means that the wind noise is highly directional, thus the spherical harmonic coefficients of higher modes will be large, because different modes of the spherical harmonics function represent different patterns, e.g., the first mode $Y_0^0(\theta, \phi)$ represents a monopole pattern, the spherical harmonics of the order $n = 1$ are dipole patterns, and higher modes have more complex patterns [16].

To illustrate this, the spherical harmonics coefficients of the wind noise at 20 Hz, 60 Hz and 100 Hz are shown in Figure 5.13(b) to (d), where the mode number is $l = n(n+1)+m+1$, where $l = 1$ represents the first mode $Y_0^0(\theta, \phi)$ and the $l = 49$ indicates the highest mode $Y_N^N(\theta, \phi)$. It is clear that the spherical harmonics coefficients of higher modes have similar value to those of lower modes and no regularity of the coefficients distribution is observed at the three frequencies. In contrast, the sound signal below 100 Hz is dominated by the first

few spherical harmonics, as shown in Figure 5.14 for a single tonal sound at 100 Hz recorded by the spherical microphone array. At 100 Hz, the sound wavelength is much larger than the size of the spherical microphone array; hence the sound signals at the front and rear of the sphere are almost the same both in amplitude and phase, as shown in Figure 5.14(a). In this case, the directivity pattern is almost a monopole, so the coefficient of the first spherical harmonic mode is much larger than those of the higher modes, as shown in Figure 5.14(b).

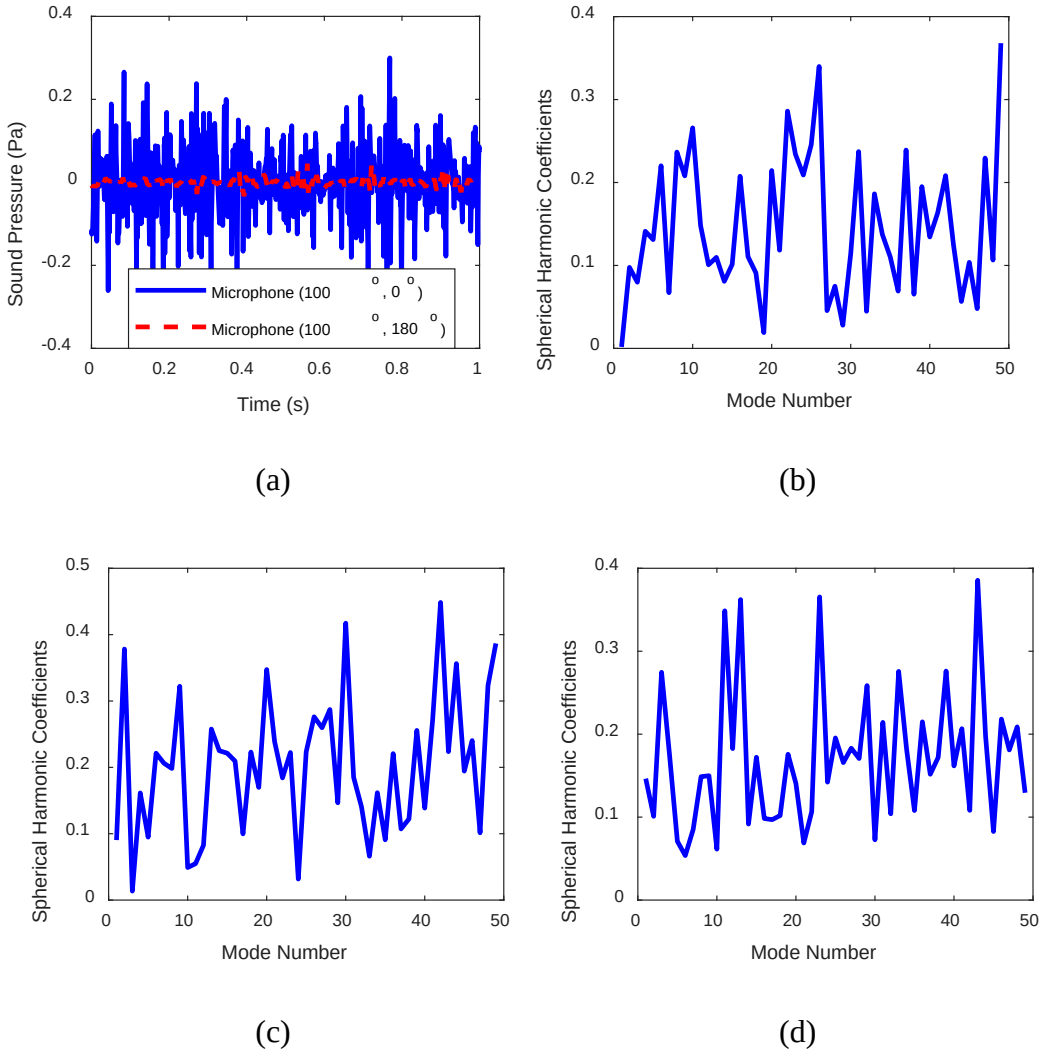

Figure 5.13 (a) Comparison of the time domain wind noise waveform measured at the front (100°, 0°) and the rear (100°, 180°) of the rigid spherical microphone array, and the spherical harmonics coefficients at (b) 20 Hz, (c) 60 Hz and (d) 100 Hz.

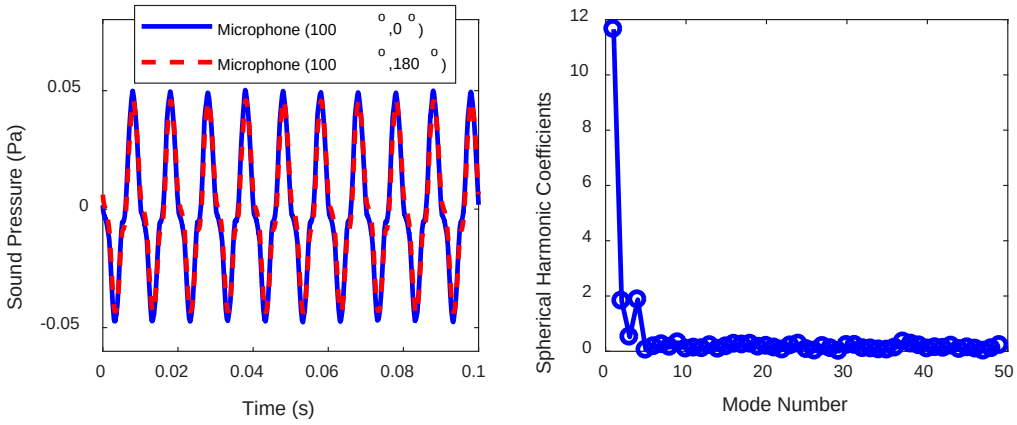

(a) (b)

Figure 5.14 Comparison of the time domain sound signal waveform measured at the front (100°, 0°) and the rear (100°, 180°) of the rigid spherical microphone array, and (b) the spherical harmonics coefficients at 100 Hz.

The distinct characteristics of wind noise and sound signal in the spherical harmonics domain can be explained qualitatively. Wind noise is caused by pressure fluctuations in turbulence rather than the impressible sound wave. The turbulence wavelength $\zeta = U_0/f$ is much smaller than the sound wavelength $\lambda = c_0/f$ at frequency f, because the wind speed U_0 (4.2 m/s in our test) is usually two orders of magnitude smaller than the speed of sound c_0 (340 m/s) [9]. At low frequency, e.g., 100 Hz, the sound wavelength is 3.4 m, much larger than the sphere diameter (here 0.2 m), while the turbulence wavelength is only 0.042 m, much smaller than the sphere diameter. This might be the reason that the sound energy is dominated by the first few modes and the wind noise energy is irregularly distributed in the spherical harmonics domain.

By substituting the spherical harmonic coefficients of the wind nose and sound signal to Eq. (5.16), the array output can be obtained. Comparing Figure 5.13(b) and Figure 5.14(c), the presence of wind noise introduces an extra vector on the spherical harmonic coefficients

of the desired sound signal. The quantitative effect of wind noise on the beamforming performance will be investigated in the next section.

B. Simulation results

To investigate effect of wind noise on the beamforming performance of the PWD, DAS, and MVDR beamformers systematically, synthetic tonal signals of different frequencies are superposed to the measured wind noise to compose the noisy signals of various SNR. The SNR is defined as the ratio of the overall sound energy to the overall wind noise energy in all the microphones in the spherical array, which is calculated as

$$SNR(f) = 10\log_{10}\frac{\sum_{q=1}^{Q} P_{s,q}(f)^2}{\sum_{q=1}^{Q} P_{n,q}(f)^2} \tag{5.20}$$

where $P_{s,q}(f)$ and $P_{n,q}(f)$ is the sound signal and wind noise at the q-th microphone, respectively. The performance of the beamforming is evaluated by the RMSE and the DF for the sound source localization accuracy and the spatial resolution, respectively. Because the wind noise dominates in the low frequency range below 200 Hz, the effect of wind noise on the beamforming performance of the PWD, DAS and MVDR beamformers are illustrated in Figure 5.15, which shows the DF as a function of frequency from 10 Hz to 200 Hz for different SNR. In the simulation, each calculation is based on 1 s recording of the wind noise with a sampling rate of 44.1 kHz, and a total of 20 s recordings are calculated for average, where the vertical bars indicate the standard deviation.

When there is no wind noise, all three types of beamformers can accurately localize the sound source location as the RMSE are all zero. The MVDR shows the best spatial resolution because it has the highest DF of about 28 dB, while the DAS beamformer has the worst spatial resolution with a DF of −3.8 dB. Figure 5.15 shows that when the wind noise is present, the PWD beamformer fails to localize the sound source direction because the RMSE

is over 60°, except at very high SNR such as 40 dB, where the RMSE is about 25°. Therefore, the PWD beamformer is not robust to wind noise. In contrast, the DF of the DAS beamformer is not affected by the wind noise while the RMSE grows with decreasing SNR while. When the SNR is 0 dB, the RMSE of the DAS beamformer is about 6° whereas when the SNR is −10 dB, the RMSE varies between 10° and 20° in the frequency range between 20 Hz and 200 Hz, as illustrated in Figure 5.15(c). It is clear that the DAS beamformer is much more robust to the wind noise than the PWD beamformer. This is because the PWD beamformer is designed to maximize the directivity without considering the robustness, hence it has higher DF for clean signals but is not robust to noise [16]. In contrast, the DAS beamformer is designed to maximize the robustness without accounting for the directivity, thus it is robust to noise but shows a poor spatial resolution, especially in the low frequency range [16].

Different from the PWD and DAS beamformers, which are designed for clean signals and the array weights are independent of the input signals, the MVDR beamformer is tailored to the actual measured noisy signals. Figure 5.15(e) and (f) show that the RMSE of the MVDR beamformer is slightly increased due to the presence of wind noise, while the DF is heavily degraded and decreases with the SNR. When the SNR is −10 dB, the RMSE decreases from 25° at 10 Hz to 4° at 200 Hz, and the DF increases from 0.6 dB at 10 Hz to 8.4 dB at 200 Hz. The MVDR beamformer shows better performance in the presence of wind noise with a smaller RMSE but a higher DF compared to the DAS beamformer. It can be observed from Figure 5.15(c) and (e) that the beamforming performance decreases in the lower frequency range for both DAS and MVDR beamformers. This might because at low frequencies such as 10 Hz, the turbulence wavelength is 0.42 m, which is comparable to the size of the spherical microphone array and the wind noise signals around the sphere becomes more correlated that those at higher frequencies.

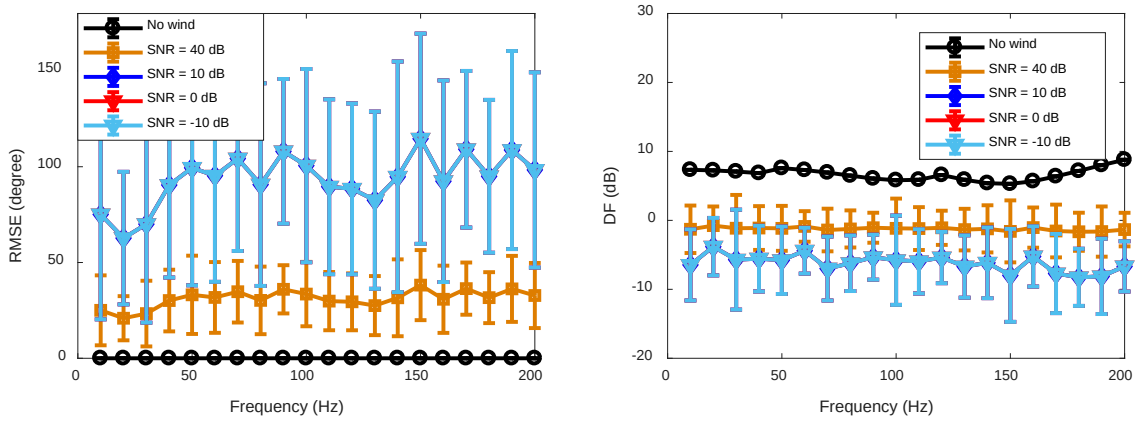

(a) (b)

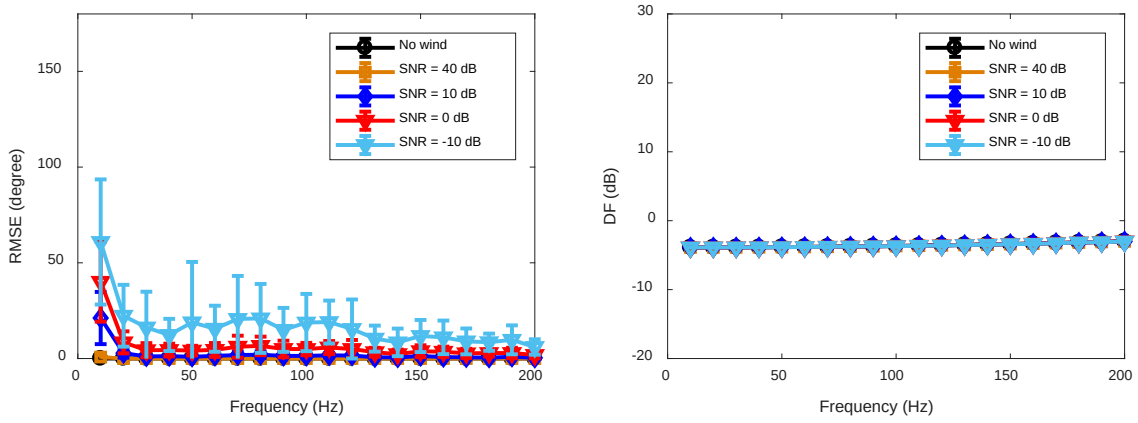

(c) (d)

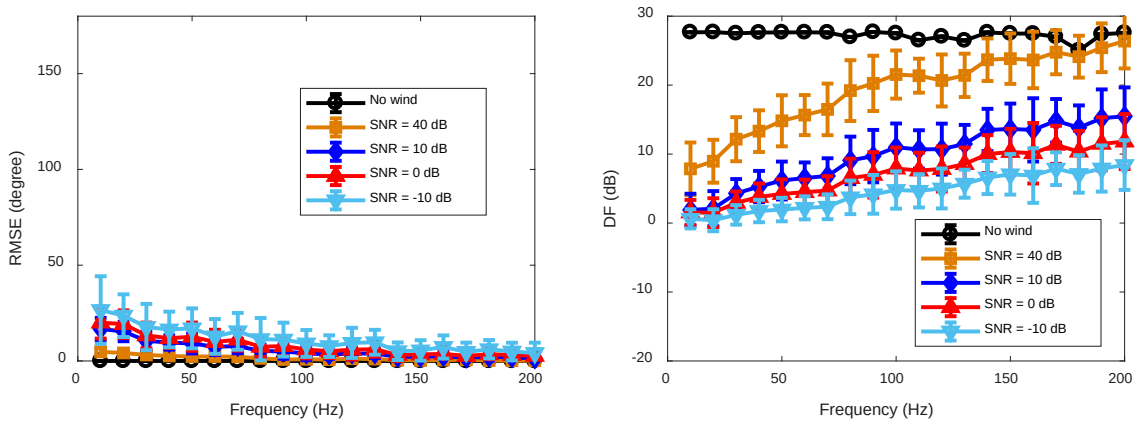

(e) (f)

Figure 5.15 (a) The RMSE and (b) the DF for the PWD beamformer, (c) the RMSE and (d) the DF for the DAS beamformer, and (e) the RMSE and (f) the DF for the MVDR beamformer as a function of frequency.

In summary, the presence of wind noise degrades the beamforming performance of the PWD, DAS, and MVDR beamformers in terms of the sound source direction localization accuracy and spatial resolution. The PWD fails as a beamformer under windy conditions because the RMSE is too large to find the sound source direction. The localization accuracy of the DAS beamformer is reduced although the spatial resolution is not affected by the wind noise. In contrast, the MVDR beamformer shows the best performance among the three beamformers with the smallest RMSE but the highest DF, and the performance increases with frequency from 10 Hz to 200 Hz.

C. Experiment results

To investigate the MVDR beamforming performance in the presence of wind noise and compare with that without wind, experiments were carried out to in an anechoic chamber to record both the pure sound signal and the wind noise contaminated sound signals, as shown in Figure 5.12. The fan was located at a direction of (90°, 90°) relative to the spherical microphone array, respectively. The pure sound signal was recorded first when the loudspeaker was active while the fan was not working. Then, the noisy signals were recorded when both the fan and sound source were active, and the sound pressure level of the single tonal sound signal was tuned to be 5 dB higher (SNR = +5dB), the same level (SNR = 0 dB), and 5 dB lower (SNR = –5 dB) than the wind noise.

The experimental results of the beamforming map at 100 Hz are shown in Figure 5.16 to Figure 5.18 for the PWD, DAS and MVDR beamformers, respectively. Figure 5.16 shows that when there is no wind noise, the PWD beamformer is able to estimate the sound source direction with a 6.7° bias from the exact sound source direction. However, the PWD beamformer fails to localize the sound source direction when the wind noise is present, in

consistent with the simulation results in Figure 5.15(a), where a more than 90° RMSE is observed.

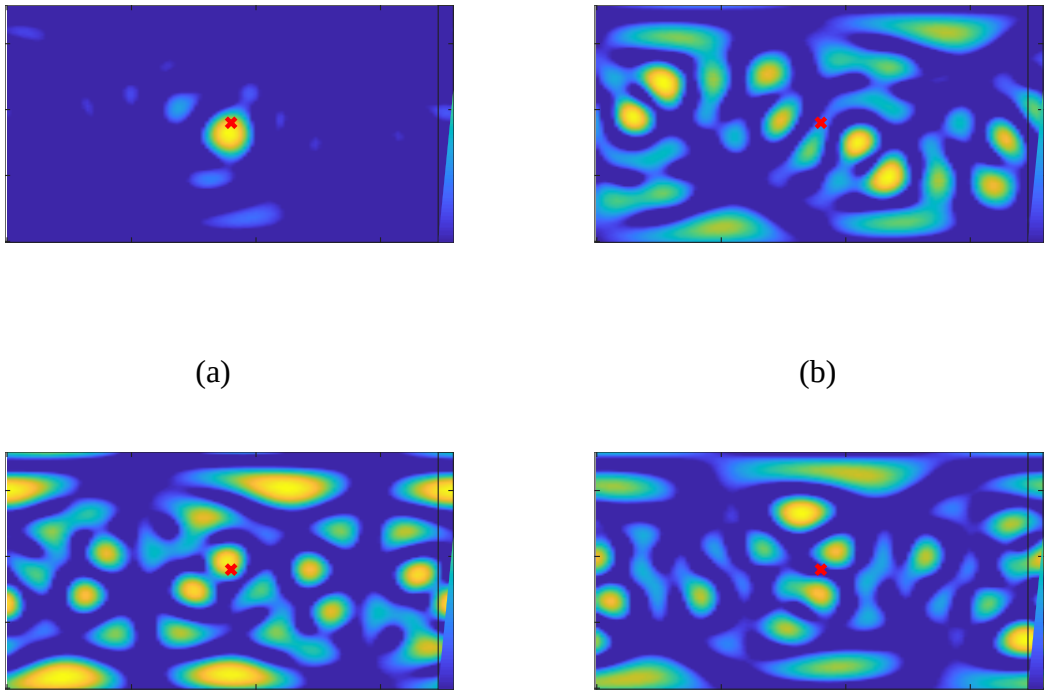

(a) (b)

(c) (d)

Figure 5.16. The effect of wind noise on the PWD beamforming map at 100 Hz (a) without wind noise, and with wind noise at a SNR of (b) +5 dB, (c) 0 dB, and (d) –5 dB. The red cross markers indicate the actual sound source direction.

In contrast, the DAS beamformer is more robust to wind noise, as illustrated in Figure 5.17, which shows that when there is no wind, the sound source direction is correctly estimated, whereas when the wind noise is present, a small bias from the actual sound source direction is observed, i.e., a RMSE of 9.5°, 10.6° and 11.8° corresponding to the SNR of +5 dB, 0 dB and –5 dB, respectively. It is worth noting that the dynamic range shown by the color bar in Figure 5.17 is zoomed to 1 dB for the array output pattern to be observed clearly,

therefore the spatial resolution of the DAS beamformer is very poor, with a DF of –3.6 dB. This is consistent with the simulation results in Figure 5.15(c) where a DF of –3.8 dB is obtained for the DAS beamformer regardless of the SNR value.

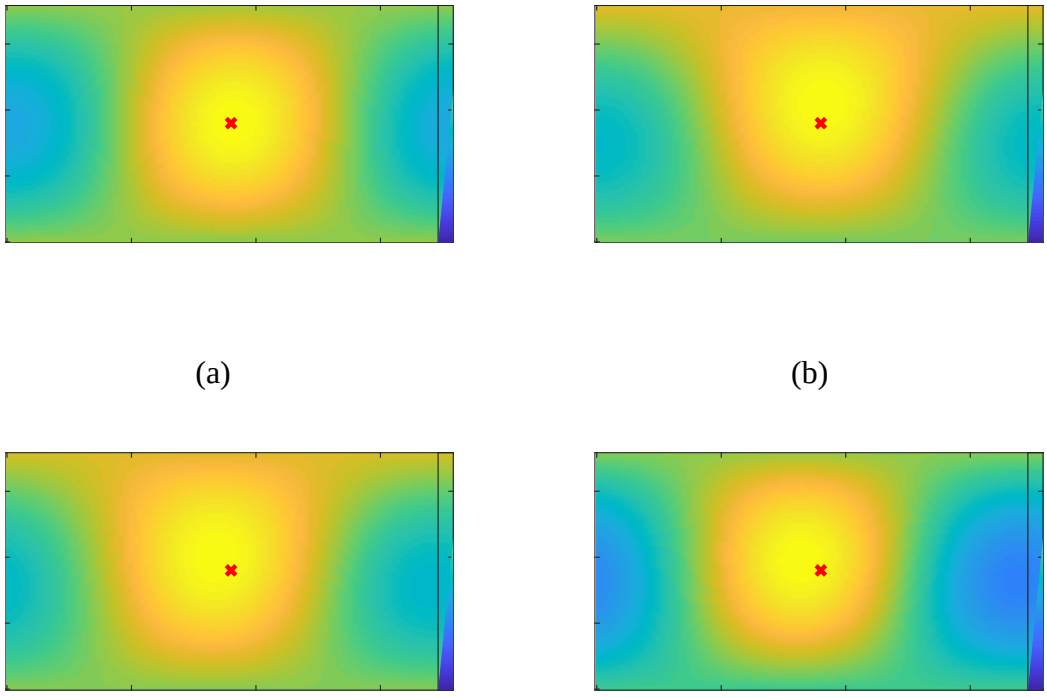

(a) (b)

(c) (d)

Figure 5.17. The effect of wind noise on the DAS beamforming map at 100 Hz (a) without wind noise, and with wind noise at a SNR of (b) +5 dB, (c) 0 dB, and (d) –5 dB. The red cross markers indicate the actual sound source direction.

The MVDR beamformer shows the best performance among the three beamformers, as shown in Figure 5.18. It can be observed that the sound source direction is correctly localized by the MVDR beamformer when there is no wind noise, with a high resolution, i.e., the DF is 8.2 dB. In the presence of wind noise, the estimated sound source direction is slightly biased from the actual sound source direction denoted by the red cross marker in Figure 5.18, with a

RMSE of 6.7°, 7.1° and 8.7° corresponding to the SNR of +5 dB, 0 dB and –5 dB, respectively. In addition, the spatial resolution of the MVDR beamformer is higher than that of the DAS beamformer although it is reduced by the wind noise.

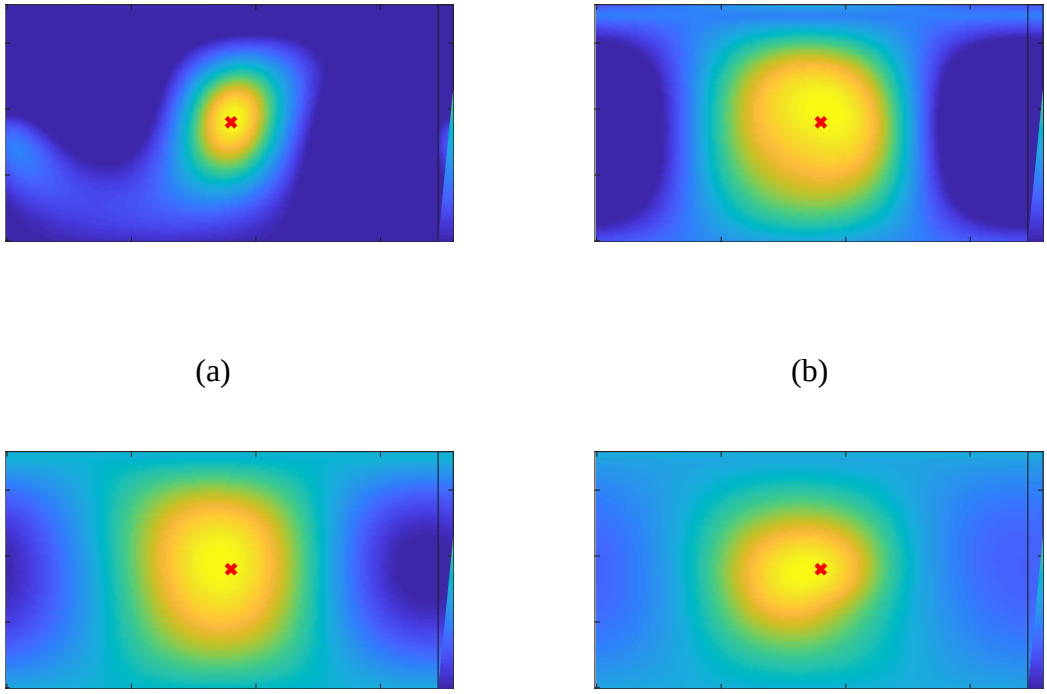

(a) (b)

(c) (d)

Figure 5.18. The effect of wind noise on the MVDR beamforming map at 100 Hz (a) without wind noise, and with wind noise at a SNR of (b) +5 dB, (c) 0 dB, and (d) –5 dB. The red cross markers indicate the actual sound source direction.

To quantitatively compare the beamforming performance of all three beamformers, the RMSE and the DF are calculated and summarized in Table 5.3, where the simulation results are also given for comparison. It is clear that the experimental results are consistent with the simulation results, and the best performance is achieved by the MVDR beamformer, with the smallest RMSE and the largest DF. For the MVDR beamformer, the wind noise increases the

RMSE from 1.1° without wind noise to 7.1° when the wind noise is present with a SNR of 0 dB, and correspondingly the DF is reduced from 8.2 dB to 0.4 dB. It can also be observed from Table 5.3 that both the RMSE and DF of the MVDR beamformer are slightly dependent on the SNR when wind noise exists, with the RMSE increased from 6.7° to 8.7° and the DF decreased from 1.1 dB to 0.6 dB when the SNR varies from +5 dB to –5 dB.

Table 5.3 The Root Mean Square Error (RMSE) and the Directivity Factor (DF) for the PWD,DAS and MVDR beamformers with and without wind noise at 100 Hz.

		Experiments				Simulations			
Beamformer	SNR (dB)	No wind	+5	0	–5	No wind	+5	0	–5
PWD	RMSE (°)	6.7	93.7	113.7	120.7	0	95.5	95.5	95.5
	DF (dB)	8.0	–6.1	–6.4	–7.1	7.0	–8.5	–8.5	–8.5
DAS	RMSE (°)	0	9.5	10.6	11.8	0	1.4	5.0	18.8
	DF (dB)	–3.6	–3.6	–3.6	–3.6	–3.8	–3.8	–3.8	–3.8
MVDR	RMSE (°)	1.1	6.7	7.1	8.7	0	4.3	5.9	7.7
	DF (dB)	8.2	1.1	0.4	0.6	27.6	9.1	7.6	6.2

In summary, the above results demonstrate that the MVDR beamformer can be used to localize the sound source direction with a certain accuracy under windy conditions. This indicate the possibility of applying the spherical microphone array for outdoor low frequency wind turbine noise measurements and noise source localization in windy environments, which will be pursued in the future work. In addition, it is noteworthy that the above results are based on tonal signals. For broadband sound signals, the beamforming can be performed in two ways. First, the broadband signals can be transformed to the frequency domain and the beamforming is performed for each frequency bin or in octave bands to localise the sound source direction. Second, the time domain broadband beamforming methods can be formulated to localise the sound source direction from the broadband signals directly. This

will be investigated together with the full-field outdoor wind turbine noise measurements in the future.

5.3.3 Conclusions

This section investigated the effect of wind noise on the beamforming performance of the PWD, DAS and MVDR beamformers with a rigid spherical microphone array. The wind noise was first measured and analysed in the spherical harmonics domain, and the wind noise energy was found to be irregularly distributed in the spherical harmonics domain. Then, the beamforming performance of the spherical PWD, DAS and MVDR beamformers was studied in the presence of wind noise for different SNR and frequencies, and the MVDR beamformer was found to achieve the best performance. The experimental results demonstrated that the MVDR beamformer is able to localize the sound source direction in the presence of wind noise at low frequency (100 Hz) with a low SNR of −5 dB, indicating the possibility of applying the spherical microphone array for outdoor wind turbine noise measurements. Future work will measure and localize the wind turbine noise with the spherical microphone array in outdoor windy conditions.

5.4 Summary

This chapter reports the research of utilizing a rigid spherical microphone array to characterise and reduce wind noise, and investigating the effect of wind noise on the spherical beamforming performance.

First, the sound signals and wind noise were measured separately with the spherical microphone array and analysed in the spherical harmonics domain. The wind noise was found to be randomly distributed in the spherical harmonics domain, distinct from the sound signal which is concentrated in the first few spherical harmonic modes. This difference was utilized to reduce the wind noise without degrading the desired sound pressure level by using a low

pass filter method in the spherical harmonics domain. Experimental results with both single-tonal and multi-tonal sound signals demonstrated that the proposed method can reduce wind noise by more than 10 dB in the frequency range below 500 Hz, and the sound pressure level of the desired sound signal can be extracted from wind noise with an error within 1.0 dB, even when the sound level is 8 dB lower than the wind noise.

Then, the effects of wind noise on the beamforming performance of a spherical microphone array were investigated. It was shown that the presence of wind noise introduces an extra term on the array output. The wind noise was measured with the spherical microphone array, and the wind noise energy was found to be irregularly distributed in the spherical harmonics domain. The performance of the Plane Wave Decomposition (PWD), the Delay and Sum (DAS) and the Maximum Variance Distortionless Response (MVDR) beamformers was presented and compared in the presence of wind noise. The MVDR beamformer was found to be the best under various signal-to-noise ratios at different frequencies in terms of the directivity factor. Experiment results demonstrated that the MVDR beamformer is able to localise the sound source direction under windy conditions at low frequencies.

Future work will investigate:

(a) effect of the size of the spherical microphone array on wind noise reduction;

(b) combination of the array and windscreen to further reduce wind noise;

(c) application of other array such as differential microphone array for wind noise reduction; and

(d) carry out outdoor onsite wind turbine noise measurements to test the proposed method for wind noise reduction.

6 Conclusions and future work

6.1 Conclusions

The objective of this PhD research was to investigate the mechanism of wind noise generation, to study the wind noise reduction mechanism of porous microphone windscreen, and to develop a new compact acoustic measurement system that is insensitive to wind noise. To achieve this research objective, an extensive literature review was presented first, based on which the theoretical approaches, numerical simulations, and experimental measurements were utilised in the investigation. To summarise, the following major outcomes and contributions are identified and documented in this thesis.

- A pressure structure function model that incorporates both the inertial range and the dissipation range of turbulence is proposed, based on which the pressure spectrum extending to the dissipation range is obtained. This pressure spectrum can be used to describe wind noise spectra measured outdoors.
- A pressure structure function model that combines the energy-containing range and the dissipation range is proposed, from which the pressure spectrum for small Reynolds number turbulent flows is obtained. This pressure spectrum can be utilized to predict the wind noise spectra in indoor environments such as wind tunnels and fans.
- The effect of both the viscous and inertial forces on the wind noise reduction of porous microphone windscreens was investigated, and it was found that the design of porous microphone windscreens should take into account both turbulence suppression inside and wake generation behind the windscreens to achieve optimal performance.
- Simulations and measurements with two microphones demonstrate that porous microphone windscreens are the most effective in attenuating wind noise in a certain

frequency range, where the windscreen diameter is approximately 2 to 4 times the turbulence wavelengths, and that the wind noise reduction is related to the spatial decorrelation of wind noise signals provided by porous microphone windscreens.

- Spherical microphone arrays were used to suppress the wind noise in the measured signals, where a low pass filter method in the spherical harmonics domain was used to extract the desired sound signal from wind noise even when the sound signal is lower than the wind noise.

6.2 Future works

The goal of the research is to develop a reliable compact measurement system for wind turbine noise investigation. It is hoped that the size of measurement configuration will be reduced from current few meters to less than 10 centimetres based on the specially designed windproof shell and microphone array geometry together with the adaptive noise cancellation algorithm. Various potential research directions were spotted during the course of this PhD work, which can provide deeper understanding of wind noise generation and reduction, and will have productive outcomes when undertaken as potential future work. These include:

- Conducting measurements of the velocity fluctuations and turbulence intensity both inside and outside porous microphone windscreens. This will help understand the relations between the velocity and pressure fluctuations in turbulent flows and thus the generation mechanism of wind noise.
- Investigating the effect of the finite Reynolds number on wind noise spectra. The two theoretical models proposed this thesis assume that the Reynolds number to be either large or small. However, the quantitative relationship between the Reynolds number and wind noise spectra remains unclear.

- Studying the effect of the finite size of microphone diaphragm on the measured wind noise spectra. In the existing models, the interaction between the incoming flow and the microphone is not taken into account.
- Building porous microphone windscreens with variable porosity to achieve better performance. It is shown in this thesis that the design of porous microphone should take into account both turbulence suppression inside and wake generation behind the windscreens. A variable porosity windscreen with inner low porosity material and outer high porosity material may offer superior performance.
- Exploring other array such as the differential microphone array for wind noise reduction. The differential microphone arrays are small in size and are effective for the entire audio and sub-audio frequency bands, with a potential to be used for wind noise reduction as a compact system.
- Combining the passive porous microphone windscreens with the spherical microphone array. Installing a porous layer around the spherical microphone array may reduce the wind noise effect and the combination system may have better wind noise reduction performance.
- Carrying out outdoor experiments to measure the wind noise reduction of various windscreens. Most the experiments in this thesis were conducted in indoor environments. Outdoor experiments are desired to further verify the simulation and indoor measurement results.

Appendix A: List of publications

The publications during the PhD candidature are as follows:

- **Journal articles**

1. **Sipei Zhao**, Eva Cheng, Xiaojun Qiu, Ian Burnett and Jacob Chia-chun Liu. Spatial decorrelation of wind noise by porous microphone windscreens. ***Journal of Acoustical Society of America***. 2018, **143**(1): 330-339.
2. **Sipei Zhao**, Eva Cheng, Xiaojun Qiu, Ian Burnett and Jacob Chia-chun Liu. Wind noise spectra in small Reynolds number turbulent flows. ***Journal of Acoustical Society of America***. 2017, **142**(5): 3227-3233.
3. **Sipei Zhao**, Matthew Dabin, Eva Cheng, Xiaojun Qiu, Ian Burnett and Jacob Chia-chun Liu. On the physical mechanism of wind noise reduction by porous microphone windscreens. ***Journal of Acoustical Society of America***. 2017, **142**(4): 2454-2463.
4. **Sipei Zhao**, Eva Cheng, Xiaojun Qiu, Ian Burnett and Jacob Chia-chun Liu. Pressure spectra in turbulent flows in the inertial and the dissipation ranges. ***Journal of Acoustical Society of America***. 2016, **140**(6): 4178-4182.
5. **Sipei Zhao**, Matthew Dabin, Eva Cheng, Xiaojun Qiu, Ian Burnett and Jacob Chia-chun Liu. Effects of wind noise on the spherical microphone array beamforming performance. ***Applied Acoustics***. 2018 (**submitted**).
6. **Sipei Zhao**, Matthew Dabin, Eva Cheng, Xiaojun Qiu, Ian Burnett and Jacob Chia-chun Liu. Characterisation and reduction of wind noise with a spherical microphone array. ***Journal of Acoustical Society of America***. 2018 (**submitted**).

- **Conference papers**

1. **Sipei Zhao**, Eva Cheng, Xiaojun Qiu, Ian Burnett and Jacob Chia-chun Liu. Experimental investigation on the wind noise reduction of semi-spherical metal mesh

windscreens. In *Proc. of the 25th International Congress on Sound and Vibration (ICSV 25)*, Hiroshima, Japan, 8-12 July, 2018. (**accepted**)

2. **Sipei Zhao**, Eva Cheng, Xiaojun Qiu, Ian Burnett and Jacob Chia-chun Liu. Simulations on the wind noise reduction by spherical shell windscreens. In *Proc. of the 46th International Congress and Exposition on Noise Control Engineering (INTER-NOISE 2017)*, Hong Kong, 27-30 August, 2017. (**Young Professional Grant**)
3. **Sipei Zhao**, Eva Cheng, Xiaojun Qiu, Jordan Lacey and Simon Maisch. A method of configuring fixed coefficient active noise controllers for traffic noise reduction. In *Proc. of the 46th International Congress and Exposition on Noise Control Engineering (INTER-NOISE 2017)*, Hong Kong, 27-30 August, 2017.
4. **Sipei Zhao**, Eva Cheng, Xiaojun Qiu, Ian Burnett and Jacob Chia-chun Liu. Estimation of the frequency boundaries of the inertial range for wind noise spectra in anechoic wind tunnels. In *Proc. of the Second Australasian Acoustical Societies Conference (ACOUSTICS 2016)*, Brisbane, Australia, 9-11 Novermber, 2016.
5. **Sipei Zhao**, Eva Cheng, Xiaojun Qiu, Pantea Alambeigi, Jane Burry and Mark Burry. A preliminary investigation on the sound field properties in the Sagrada Familia Basilica. In *Proc. of the Second Australasian Acoustical Societies Conference (ACOUSTICS 2016)*, Brisbane, Australia, 9-11 Novermber, 2016.
6. Pantea Alambeigi, **Sipei Zhao**, Jane Burry and Xiaojun Qiu. Complex human auditory perception and simulated sound performance prediction. In *Proc. of the 21st International Conference of the Association for Computer-Aided Architectural Design Research in Asia (CAARDRIA 2016)*, Melbourne, Australia, 30 March-02 April, 2016. (**Best Paper Award**)

References

[1] Hansen CH, Doolan CJ, Hanse KL. Wind farm noise: measurement, assessment, and control. New York, USA: John Wiley & Sons Inc; 2017.

[2] Pedersen CS, Waye KP. Perception and annoyance due to wind turbine noise - a dose-response relationship. J Acoust Soc Am 2004;116:3460–70. doi:10.1121/1.3543957.

[3] Bakker RH, Pedersen E, van den Berg GP, Stewart RE, Lok W, Bouma J. Impact of wind turbine sound on annoyance, self-reported sleep disturbance and psychological distress. Sci Total Environ 2012;425:42–51. doi:10.1016/j.scitotenv.2012.03.005.

[4] Micic G, Zajamsek B, Lack · Leon, Hansen K, Doolan C, Hansen C, et al. A review of the potential impacts of wind farm noise on sleep. Acoust Aust 2018:1–11. doi:10.1007/s40857-017-0120-9.

[5] Raspet R, Webster J, Dillion K. Framework for wind noise studies. J Acoust Soc Am 2006;119:834–43. doi:10.1121/1.2146113.

[6] Raspet R, Yu J, Webster J. Low frequency wind noise contributions in measurement microphones. J Acoust Soc Am 2008;123:1260–9. doi:10.1121/1.2832329.

[7] IEC64100-11. Wind turbines - Part 11: Acoustic noise measurement techniques. 2012.

[8] Abbott J, Raspet R, Webster J. Wind fence enclosures for infrasonic wind noise reduction. J Acoust Soc Am 2015;137:1265–73. doi:10.1121/1.4908568.

[9] Hedlin MAH, Raspet R. Infrasonic wind-noise reduction by barriers and spatial filters. J Acoust Soc Am 2003;114:1379–86. doi:10.1121/1.1598198.

[10] Oerlemans S, Sijtsma P, Méndez López B. Location and quantification of noise sources on a wind turbine. J Sound Vib 2007;299:869–83. doi:10.1016/j.jsv.2006.07.032.

[11] Ramachandran RC, Raman G, Dougherty RP. Wind turbine noise measurement using a compact microphone array with advanced deconvolution algorithms. J Sound Vib 2014;333:3058–80. doi:10.1016/j.jsv.2014.02.034.

[12] Wilson D, Greenfield R, White M. Spatial structure of low-frequency wind noise. J Acoust Soc Am 2007;122:EL223-EL228. doi:10.1121/1.2786608.

[13] Novak C, Sjöström A, Ule H, Bard D, Sandberg G. An investigation of different

secondary noise wind screen designs for wind turbine noise applications. Proc. INTER-NOISE 2014, Melbourne, Australia: 2014, p. 1–8.

[14] Noble JM, Alberts WCK, Raspet R, Collier SL, Coleman MA. Infrasound wind noise reduction via porous fabric domes. J Acoust Soc Am 2014;135:2409–2409. doi:10.1121/1.4877982.

[15] Morgan S, Raspet R. Investigation of the mechanisms of low-frequency wind noise generation outdoors. J Acoust Soc Am 1992;92:1180–3. doi:10.1121/1.404049.

[16] Hessler G. A real-time blast noise detection and wind noise rejection system. Noise Control Eng J 1996;44:306–14.

[17] Jackson IR, Kendrick P, Cox TJ, Fazenda BM, Li FF. Perception and automatic detection of wind-induced microphone noise. J Acoust Soc Am 2014;136:1176–86. doi:10.1121/1.4892772.

[18] Kendrick P, Jackson IR, Fazenda BM, Cox TJ, Li FF. Microphone handling noise: Measurements of perceptual threshold and effects on audio quality. PLoS One 2015;10:1–17. doi:10.1371/journal.pone.0140256.

[19] Zakis JA. Wind noise at microphones within and across hearing aids at wind speeds below and above microphone saturation. J Acoust Soc Am 2011;129:3897–907. doi:10.1121/1.3578453.

[20] Chung K. Comparisons of spectral characteristics of wind noise between omnidirectional and directional microphones. J Acoust Soc Am 2012;131:4508–17. doi:10.1121/1.3699216.

[21] Kokkinakis K, Cox C. Reducing the impact of wind noise on cochlear implant processors with two microphones. J Acoust Soc Am 2014;135:EL219-25. doi:10.1121/1.4871583.

[22] Richardson LF. Weather prediction by numerical process. Cambridge, UK: Cambridge University Press; 1922.

[23] Kolmogorov AN. The local structure of turbulence in incompressible viscous fluid for very large Reynolds n umbers. Proc R Soc A Math Phys Eng Sci 1991;434:9–13. doi:10.1098/rspa.1991.0075.

[24] Pope SB. Turbulent flows. New York: Cambridge University Press; 2000.

[25] Klimenko AY. Complex competitive systems and competitive thermodynamics. Philos Trans A Math Phys Eng Sci 2013;371:20120244. doi:10.1098/rsta.2012.0244.

[26] Batchelor GK. Pressure fluctuations in isotropic turbulence. Math Proc Cambridge Philos Soc 1951;47:359–74. doi:10.1017/S0305004100026712.

[27] Xu Y, Zheng Z, Wilson D. A computational study of the effect of windscreen shape and flow resistivity on turbulent wind noise reduction. J Acoust Soc Am 2011;129:1740–7. doi:10.1121/1.3552886.

[28] Hill DJ, Wilczak JM. Pressure structure functions and spectra for locally isotropic turbulence. J Fluid Mech 1995;296:241–69. doi:10.1017/S0022112095002126.

[29] Townsend AA. Measurements in the turbulent wake of a cylinder. Proc R Soc A Math Phys Eng Sci 1947;190:551–61. doi:10.1098/rspa.1947.0096.

[30] Obukhoff AM, Yaglom AM. The microstructure of turbulent flow. National Advisory Committee for Aeronautics: 1953.

[31] George WK, Beuther PD, Arndt RE a. Pressure spectra in turbulent free shear flows. J Fluid Mech 1984;148:155–91. doi:10.1017/S0022112084002299.

[32] Yu J, Raspet R, Webster J, Abbott J. Wind noise measured at the ground surface. J Acoust Soc Am 2011;129:622–32. doi:10.1121/1.3531809.

[33] Kraichnan RH. Pressure field within homogeneous anisotropic turbulence. J Acoust Soc Am 1956;28:64–72.

[34] Kraichnan RH. Pressure fluctuations in turbulent flow over a flat plate. J Acoust Soc Am 1956;28:378–90. doi:10.1121/1.1908336.

[35] Yu J, Raspet R, Webster J, Abbott J. Improved prediction of the turbulence-shear contribution to wind noise pressure spectra. J Acoust Soc Am 2011;130:3590–4. doi:10.1121/1.3652868.

[36] Raspet R, Webster J. Wind noise under a pine tree canopy. J Acoust Soc Am 2015;137:651–9. doi:10.1121/1.4906587.

[37] Webster J, Raspet R. Infrasonic wind noise under a deciduous tree canopy. J Acoust Soc Am 2015;137:2670–7. doi:10.1121/1.4919340.

[38] Kamiakito N, Shimura M, Nomura T, Hiroshi H, Osafune T, Iwabuki H. Wind noise estimation functions for low frequency sound measurement in natural wind at different

topography types. Proc. 6th Int. Meet. Wind Turbine Noise, Glasgow, UK: 2015.

[39] Shepherd IC, La Fontaine RF. Microphone screens for acoustic measurement in turbulent flows. J Sound Vib 1986;111:153–65. doi:10.1016/S0022-460X(86)81430-4.

[40] Wang JS, Crocker MJ. Tubular windscreen design for microphones for in-duct fan sound power measurements. J Acoust Soc Am 1974;55:568–75. doi:10.1121/1.1914565.

[41] Shams QA, Zuckerwar AJ, Sealey BS. Compact nonporous windscreen for infrasonic measurements. J Acoust Soc Am 2005;118:1335–40. doi:10.1121/1.1992707.

[42] Larsson M, Johansson S, Håkansson L, Claesson I. Microphone windscreens for turbulent noise suppression when applying active noise control to ducts. Proc. 12th Int. Congr. Sound Vib., Lisbon, Portugal: 2005, p. 1–8.

[43] Strasberg M. Dimensional analysis of windscreen noise. J Acoust Soc Am 1988;83:544–8. doi:10.1121/1.396148.

[44] Strasberg M. Nonacoustic noise interference in measurements of infrasonic ambient noise. J Acoust Soc Am 1979;66:1487. doi:10.1121/1.383543.

[45] van den Berg GP. The sounds of high winds: the effects of atmospheric stability on wind turbine sound and microphone noise. University of Groningen, 2006.

[46] van den Berg GP. Wind-induced noise in a screened microphone. J Acoust Soc Am 2006;119:824–33. doi:10.1121/1.2146085.

[47] Lin I-C, Hsieh Y-R, Shieh P-F, Chuang H-C, Chou L-C. The effect of wind on low frequency noise. Proc. INTER-NOISE 2014, Melbourne, Australia: 2014, p. 1–12.

[48] Wang L, Zander AC, Lenchine V V. Measurement of the self-noise of microphone wind shields. Proc. 18th Aust. Fluid Mech. Conf., Launceston, Australia: 2012, p. 1–10.

[49] Alamshah V, Zander A, Lenchine V. Effects of turbulent flow characteristics on wind induced noise generation in shielded microphones. Proc. Acoust. 2015, Hunter Valley, Australia: 2015, p. 1–11.

[50] Raspet R, Webster J, Naderyan V. Mechanisms for wind noise reduction by a spherical windscreen 2014. doi:10.1121/1.4877865.

[51] Phelps WD. Microphone wind screening. RCA Rev 1938;111:203–12.

[52] Zheng Z, Tan B. Reynolds number effects on flow/acoustic mechanisms in spherical windscreens. J Acoust Soc Am 2003;113:161–6. doi:10.1121/1.1527927.

[53] Xu Y. Flow/acoustic interactions in porous media under a turbulent wind environment. Kansas State University, 2010.

[54] Xu Y, Zheng ZC, Wilson DK. Simulation of turbulent wind noise reduction by porous windscreens using high-order schemes. J Comput Acoust 2010;18:321–34. doi:10.1142/S0218396X10004231.

[55] Zuckerwar AJ. Theory of compact nonporous windscreens for infrasonic measurements. J Acoust Soc Am 2010;127:3327–34. doi:10.1121/1.3409402.

[56] Dauchez N, Hayot M, Denis S. Effectiveness of nonporous windscreens for infrasonic measurements. J Acoust Soc Am 2016;139:3177–81. doi:10.1121/1.4954260.

[57] Dauchez N, Hayot M, Denis S, Dauchez N, Hayot M, Denis S. Infrasound transmission of non porous windscreens. Proc. Acoust. 2012, Nantes, France: 2012, p. 1–5.

[58] Adcock J, Delaire C, Griffin D, Jiggins M. Study of secondary wind shield performance in the field. Proc. 6th Int. Meet. Wind Turbine Noise, Glasgow, UK: 2015, p. 20.

[59] Bleazey JC. Experimental determination of the effecitveness of microphone wind screens. J Audio Soc 1961;9:48–54.

[60] Imaizumi H, Takahashi Y. Improvement of wind noise reduction performance of microphone-enclosed type windscreen. Proc. INTER-NOISE 2010, Libson, Portugal: 2010, p. 9.

[61] Hansen KL, Zajamsek B, Hansen C, Pacific E, Street F, Vic M, et al. Identification of low frequency wind turbine noise using secondary windscreens of various geometries. Noise Control Eng J 2014;62:125. doi:10.3397/1/376207.

[62] Noble JM, Kirkpatrick Alberts WC, Collier SL, Raspet R, Coleman MA. Wind noise suppression for infrasound sensors. Army Research Laboratory: 2014.

[63] Collier SL, Raspet R, Noble JM, Alberts WCK, Webster J. Analysis of wind noise reduction by semi-porous fabric domes. J Acoust Soc Am 2014;136:2139–2139. doi:10.1121/1.4899716.

[64] Abbott JR, Raspet R, Noble J, Alberts WCK, Collier S. Calculated wind noise for semi-porous fabric domes. J Acoust Soc Am 2016;139:2120–2120. doi:10.1121/1.4950310.

[65] Walker KT, Hedlin MAH. A review of wind-noise reduction methodologies. In: Pichon A Le, Blanc E, Hauchecorne A, editors. Infrasound Monit. Atmos. Stud., Springer; 2010, p. 141–82.

[66] Hedlin MAH, Walker K, Drob DP, de Groot-Hedlin CD. Infrasound: connecting the solid earth, oceans, and atmosphere. Annu Rev Earth Planet Sci 2012;40:327–54. doi:10.1146/annurev-earth-042711-105508.

[67] Daniels FB. Acoustical energy generated by the ocean waves. J Acoust Soc Am 1952;24:83–83. doi:10.1121/1.1906855.

[68] Daniels FB. Noise-reducing line microphone for frequencies below 1 cps. J Acoust Soc Am 1959;31:1180–717. doi:10.1121/1.1804966.

[69] Alcoverro B, Le Pichon A. Design and optimization of a noise reduction system for infrasonic measurements using elements with low acoustic impedance. J Acoust Soc Am 2005;117:1717–27. doi:doi:http://dx.doi.org/10.1121/1.1804966.

[70] Gabrielson TB. In situ calibration of atmospheric-infrasound sensors including the effects of wind-noise-reduction pipe systems. J Acoust Soc Am 2011;130:1154–63. doi:10.1121/1.3613925.

[71] Hedlin MAH, Berger J. Experiments with infrasonic noise-reducing spatial filters. Proc. 24th Seism. Res. Rev., Tokyo, Japan: 2002, p. 783–92.

[72] Howard W, Dillion K, Shields FD. Acoustical properties of porous hose wind noise filters. J Acoust Soc Am 2007;122:2985. doi:10.1121/1.2942646.

[73] Zumberge MA, Berger J, Hedlin MAH, Husmann E, Nooner S, Hilt R, et al. An optical fiber infrasound sensor: A new lower limit on atmospheric pressure noise between 1 and 10 Hz. J Acoust Soc Am 2003;113:2474–9. doi:10.1121/1.1566978.

[74] Bass HE, Talmadge C, Hedlin M, Walker K, Zumberge M, Garces M. Developments in infrasound sensors and wind noise reduction. J Acoust Soc Am 2007;122:2958. doi:10.1121/1.2942541.

[75] Walker K, Dzieciuch M, DeWolf S, Zumberge M, Hedlin M, Berger J. Optical fiber

infrasound sensor arrays: Signal detection and characterization capabilities in the presence of wind noise. J Acoust Soc Am 2007;122:2960. doi:10.1121/1.2942547.

[76] Walker KT, Zumberge MA, Dzieciuch MA. OFIS experiments at Camp Elliott: paving the way to infrasonic radar and a portable infrasonic sensor calibrator. Proc. 29th Monit. Res. Rev., Tokyo, Japan: 2007, p. 884–93.

[77] Walker KT, Zumberge M, Hedlin M, Berger J, Shearer P. Resolving infrasound signals with arrays of optical fiber infrasound sensors (OFIS): Low wind noise, superb back azimuth (and elevation angle) resolution, and a compact design. Infrasound Technol. Work., Tokyo, Japan: 2007, p. 37.

[78] DeWolf S, Walker KT, Zumberge MA, Denis S. Efficacy of spatial averaging of infrasonic pressure in varying wind speeds. J Acoust Soc Am 2013;133:3739–50. doi:10.1121/1.4803891.

[79] Abbott J, Raspet R. Calculated wind noise for an infrasonic wind noise enclosure. J Acoust Soc Am 2015;138:332–43. doi:10.1121/1.4922782.

[80] Abbott J, Raspet R, Raspet R, Abbott J, Raspet R. Effect of scaling laws for noise reduction optimization of wind fences of scaling laws for noise reduction optimization of wind fences. Cit Proc Mtgs Acoust 2013;19. doi:10.1121/1.4796034.

[81] Chung JY. Rejection of flow noise using a coherence function method. J Acoust Soc Am 1977;62:388–95. doi:10.1121/1.4867360.

[82] Wilson DK, White MJ. Discrimination of wind noise and sound waves by their contrasting spatial and temporal properties. Acta Acust United with Acust 2010;96:991–1002. doi:10.3813/AAA.918362.

[83] Buck S, Oerlemans S, Palo S. Experimental characterization of turbulent in fl ow noise on a full-scale wind turbine. J Sound Vib 2016;385:219–38. doi:10.1016/j.jsv.2016.09.010.

[84] Ramachandran RC, Patel H, Raman G, Dougherty RP. Localization of wind turbine noise sources using a zompact microphone array with advanced beamforming algorithms. Proc. 4th Berlin Beamforming Conf., Berlin Heidelberg: 2012, p. 1–14.

[85] Patel H, Ramachandran RC, Raman G, Jiang Y, Shi X, Krishnamurthy M. Noise source localization on a small wind turbine using a compact microphone array with advanced beamforming algorithms: Part II — a study of mechanical noise from nacelle

using a wind turbine drive train simulator. Wind Eng 2014;38:89–100. doi:10.1260/0309-524X.38.1.89.

[86] Shields FD. Low-frequency wind noise correlation in microphone arrays. J Acoust Soc Am 2005;117:3489–96. doi:10.1121/1.1879252.

[87] Bass HE, Raspet R, Messer JO. Experimental determination of wind speed and direction using a three microphone array. J Acoust Soc Am 1995;97:695–6.

[88] Costley RD, Frazier WG, Dillion K, Picucci JR, Williams JE, McKenna MH. Frequency-wavenumber processing for infrasound distributed arrays. J Acoust Soc Am 2013;134:EL307-EL313. doi:10.1121/1.1603763.

[89] McGuinn RS, Lauchle GC, Swanson DC. Low flow-noise microphone for active noise control applications. AIAA J 1997;35:29–34. doi:10.2514/2.83.

[90] Morgan MS. An investigation of the sources and attenuation of wind noise in measurement microphones. The University of Mississippi, 1993.

[91] Shust MR, Rogers JC. Active removal of wind noise from outdoor microphones using local velocity measurements. J Acoust Soc Am 1998;104:1781–1781. doi:10.1121/1.424141.

[92] Shust M. Active removal of wind noise from outdoor microphone using local velocity measurements. Michigan Technological University, 1998.

[93] Nelke CM, Nawroth N, Jeub M, Beaugeant C, Vary P. Single microphone wind noise reduction using techniques of artificial bandwidth extension. Proc. 20th Eur. Signal Process. Conf., Bucharest, Romania: 2012, p. 2328–32.

[94] Nelke CM, Vary P. Wind noise short term power spectrum estimation using pitch adaptive inverse binary masks. Proc. IEEE Int. Conf. Acoust. Speech Signal, Brisbane, Australia: 2015, p. 5068–72. doi:10.1109/ICASSP.2015.7178936.

[95] Nelke CM. Wind noise reduction: signal processing concepts. RWTH University, 2016.

[96] Nelke CM, Vary P. Measurement, analysis and simulation of wind noise signals for mobile communication devices. Proceddings 14th Int. Work. Acoust. Signal Enhanc., Sophia-Antipolis, France: 2014, p. 327–31.

[97] Nelke CM, Chatlani N, Beaugeant C, Vary P. Single microphone wind noise PSD

estimation using signal centroids. Proc. IEEE Int. Conf. Acoust. Speech Signal Process., Florence, Italy: 2014, p. 7113–7.

[98] Kuroiwa S, Mori Y, Tsuge S, Takashina M, Ren F. Wind noise reduction method for speech recording using multiple noise templates and observed spectrum fine structure. Proc. Int. Conf. Commun. Technol. Proc., Guilin, China: 2006, p. 1–5. doi:10.1109/ICCT.2006.341933.

[99] Nemer E, Leblanc W. Single-microphone wind noise reduction by adaptive postfiltering. IEEE Work. Appl. Signal Process. to Audio Acoust., 2009, p. 177–80. doi:10.1109/ASPAA.2009.5346518.

[100] Hofmann C, Wolff T, Buck M, Haulick T, Kellermann W. A morphological approach to single-channel wind-noise suppresion. Int. Work. Acoust. Signal Enhanc., Aachen, Germany: 2012, p. 1–4.

[101] Thüne P, Enzner G. Maximum-likelihood approach to adaptive multichannel-wiener postfiltering for wind-noise reduction. Proc. 12th ITG Symp. Speech Commun., Paderborn, Germany: 2016, p. 302–6.

[102] Lee J, Kim K, Shabestary T, Kang H. Deep bi-directional long short-term memomy based speech enhancement for wind noise reduction. Proc. 5th Jt. Work. Hands-free Speech Commun. Microphone Arrays, San Francisco, California, USA: 2017, p. 41–5.

[103] Franz S, Bitzer J. Multi-channel algorithms for wind noise reduction and signal compensation in binaural hearing aids. Int. Work. Acoust. Signal Enhanc., Tel Aviv, Israel: 2010, p. 1–4.

[104] Nelke CM, Vary P. Dual microphone wind noise reduction by exploiting the complex coherence. Proc. ITG Symp. Speech Commun., vol. 2, Erlangen, Germany: 2014, p. 1–4.

[105] Sakai S, Murakami T, Sakata N, Nakajima H, Nakadai K. Wind speed estimation and wind-induced noise reduction using a 2-channel small microphone array. Proc. INTER-NOISE 2016, Hamburg, Germany: 2016, p. 288–95.

[106] Park J, Park J, Lee S, Kim J, Hahn M. Coherence-based dual microphone wind noise reduction by wiener filtering. Proc. 8th Int. Conf. Signal Process. Syst., Auckland, New Zealand: 2016, p. 170–2. doi:10.1145/3015166.3015206.

[107] Schulz-DuBois EO, Rehberg I. Structure function in lieu of correlation function. Appl

Phys 1981;24:323–9.

[108] Lohse D, Muller-Groeling A. Bottleneck effects in turbulence: Scaling phenomena in r versus p space. Phys Rev Lett 1995;74:1747–50. doi:10.1103/PhysRevLett.74.1747.

[109] Gotoh T, Fukayama D. Pressure spectrum in homogeneous turbulence. Phys Rev Lett 2001;86:3775–8. doi:10.1103/PhysRevLett.86.3775.

[110] Tsuji Y, Ishihara T. Similarity scaling of pressure fluctuation in turbulence. Phys Rev E 2003;68:1–5. doi:10.1103/PhysRevE.68.026309.

[111] Ould-Rouis M, Antonia R, Zhu Y, Anselmet F. Turbulent Pressure Structure Function. Phys Rev Lett 1996;77:2222–4.

[112] Sirovich L, Smith L, Yakhot V. Energy spectrum of homogeneous and isotropic turbulence in far dissipation range. Phys Rev Lett 1994;72:344–7. doi:10.1103/PhysRevLett.72.344.

[113] Lohse D, Müller-Groeling A. Anisotropy and scaling corrections in turbulence. Phys Rev E 1996;54:395–405.

[114] Abramowitz M, Stegun I. Handbook of mathematical functions. New York: Dover Publications; 1970.

[115] Xu H, Ouellette NT, Vincenzi D, Bodenschatz E. Experimental measurement of cceleration correlations and pressure structure functions in high-reynolds number turbulence. Phys Rev Lett 2007;99:1–4. doi:10.1103/PhysRevLett.99.204501.

[116] Meldi M, Sagaut P. Pressure statistics in self-similar freely decaying isotropic turbulence. J Fluid Mech 2013;717:1–12. doi:10.1017/jfm.2012.629.

[117] Wyngaard JC. Turbulence in the atmosphere. Cambridge, UK: Cambridge University Press; 2010. doi:10.1038/177013a0.

[118] Pearson BR, Antonia RA. Reynolds-number dependence of turbulent velocity and pressure increments. J Fluid Mech 2001;444:343–82. doi:10.1017/S0022112001005511.

[119] Zhao S, Cheng E, Qiu X, Burnett I, Liu JC. Pressure spectra in turbulent flows in the inertial and the dissipation ranges. J Acoust Soc Am 2016;140:4178–82. doi:10.1121/1.4968881.

[120] Kim J, Antonia RA. Isotropy of the small scales of turbulence at low Reynolds

number. J Fluid Mech 1993;251:219–38. doi:10.1017/S0022112093003398.

[121] Pumir A. A numerical study of pressure fluctuations in three-dimensional incompressible, homogeneous, isotropic turbulence. Phys Fluids 1994;6:2071–83. doi:10.1063/1.865579.

[122] Corcos GM. Resolution of Pressure in Turbulence. J Acoust Soc Am 1963;35:192–8. doi:10.1121/1.1918431.

[123] Nithiarasu P, Seetharamu KN, Sundararajan T. Natural convective heat transfer in a fluid saturated variable porosity medium. Int J Heat Mass Transf 1997;40:395–3967.

[124] Narasimhan A. Essentials of heat and fluid flow in porous media. CRC Press; 2013.

[125] Dawson MA, Germaine JT, Gibson LJ. Permeability of open-cell foams under compressive strain. Int J Solids Struct 2007;44:5133–45. doi:10.1016/j.ijsolstr.2006.12.025.

[126] Miller SL, Childers DG. Probability and Random Process: With Applications to Signal Processing and Communications. 1st ed. London: Elsevier Academic Press; 2004.

[127] Lage JL, Krueger PS, Narasimhan A. Protocol for measuring permeability and form coefficient of porous media. Phys Fluids 2005;17:1–4. doi:10.1063/1.1979307.

[128] Urzhumov YA, Smith DR. Fluid flow control with transformation media. Phys Rev Lett 2011;107:74501. doi:10.1103/PhysRevLett.107.074501.

[129] Urzhumov YA, Smith DR. Flow stabilization with active hydrodynamic cloaks. Phys Rev E 2012;86. doi:10.1103/PhysRevE.86.056313.

[130] Carter GC, Knapp CH, Nuttall AH. Estimation of the magnitude-squared coherence function Via overlapped fast Fourier transform processing. IEEE Trans Audio Electroacoust 1973;21:337–44. doi:10.1109/TAU.1973.1162496.

[131] Zhao S, Cheng E, Qiu X, Burnett I, Liu C. Simulations on the wind noise reduction by spherical shell windscreens. Proc. INTER-NOISE 2017, 2017, p. 1–8.

[132] Rafaely B. Fundamentals of Spherical Array Processing. vol. 1. Berlin Heidelberg: Springer Berlin Heidelberg; 2015.

[133] Mabande E, Kowalczyk K, Sun H, Kellermann W. Room geometry inference based on spherical microphone array eigenbeam processing. J Acoust Soc Am 2013;134:2773–89. doi:10.1121/1.4820895.

[134] Rathsam J, Rafaely B. Analysis of in situ acoustic absorption using a spherical microphone array. Appl Acoust 2015;89:273–80. doi:10.1016/j.apacoust.2014.10.008.

[135] Ben-Hur Z, Sheaffer J, Rafaely B. Joint sampling theory and subjective investigation of plane-wave and spherical harmonics formulations for binaural reproduction. Appl Acoust 2018;134:138–44. doi:10.1016/j.apacoust.2018.01.016.

[136] Hu Y, Lu J, Qiu X. A maximum likelihood direction of arrival estimation method for open-sphere microphone arrays in the spherical harmonic domain. J Acoust Soc Am 2015;138:791–4. doi:10.1121/1.4926907.

[137] Hu Y, Lu J, Qiu X. Direction of arrival estimation of multiple acoustic sources using a maximum likelihood method in the spherical harmonic domain. Appl Acoust 2018;135:85–90. doi:10.1016/j.apacoust.2018.02.005.

[138] VisiSonics. VisiSonics 5/64 Audio Visual Camera 2015. http://visisonics.com/download/audiovisual-camera-pamphlet/ (accessed February 21, 2018).

[139] Zhao S, Cheng E, Qiu X, Burnett I, Liu JC. Wind noise spectra in small Reynolds number turbulent flows. J Acoust Soc Am 2017;142:3227–33. doi:10.1121/1.5012740.

[140] Rafaely B. Plane-wave decomposition of the sound field on a sphere by spherical convolution. J Acoust Soc Am 2004;116:2149–57. doi:10.1121/1.2063108.

[141] Sun H, Mabande E, Kowalczyk K, Kellermann W. Localization of distinct reflections in rooms using spherical microphone array eigenbeam processing. J Acoust Soc Am 2012;131:2828–40. doi:10.1121/1.3688476.

[142] Khaykin D, Rafaely B. Acoustic analysis by spherical microphone array processing of room impulse responses. J Acoust Soc Am 2012;132:261–70. doi:10.1121/1.4726012.

[143] Hu Y, Zhou H, Lu J, Qiu X. Effects of a near-field rigid sphere scatterer on the performance of linear microphone array beamformers. J Acoust Soc Am 2016;140:924–35. doi:10.1121/1.4960546.

[144] Chu Z, Yang Y, He Y. Deconvolution for three-dimensional acoustic source identification based on spherical harmonics beamforming. J Sound Vib 2015;344:484–502. doi:10.1016/j.jsv.2015.01.047.

[145] Gover BN, Ryan JG, Stinson MR. Directional measurements in sound fields using a

spherical microphone array. J Acoust Soc Am 2004;116:2138–48. doi:10.1121/1.4784883.